CHALMERS

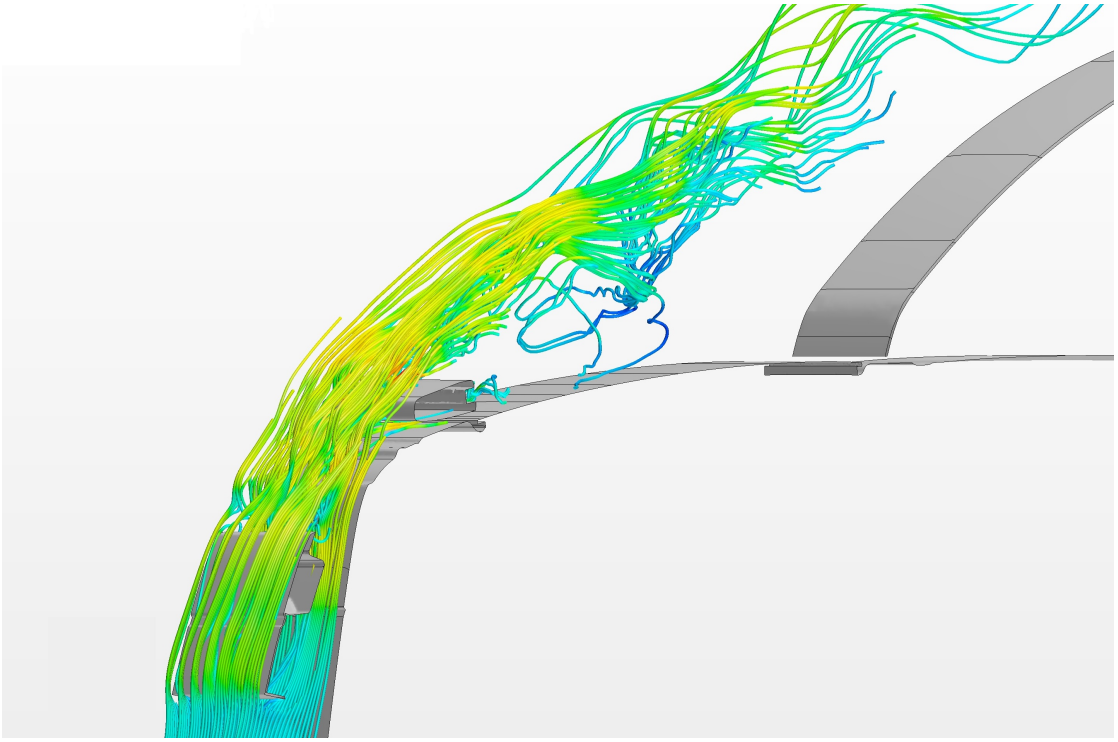

Aeroacoustic study on the roofbar of a truck using CFD

Master's thesis in Applied Mechanics

Erik Johansson

Division of Fluid Dynamics
Department of Applied Mechanics
Chalmers University of Technology
Gothenburg, Sweden
Master's thesis 2013:66

MASTER'S THESIS 2013:66

Aeroacoustic study on the roofbar of a truck using CFD

ERIK JOHANSSON

Department of Applied Mechanics
Division of Fluid Dynamics
CHALMERS UNIVERSITY OF TECHNOLOGY
Gothenburg, Sweden 2013

Aeroacoustic study on the roofbar of a truck using CFD
ERIK JOHANSSON

Master's Thesis 2013:66
ISSN 1652-8557

Department of Applied Mechanics
Division of Fluid Dynamics
Chalmers University of Technology
SE-41296 Gothenburg
Sweden

Tel. +46-(0)31 772 1000

Cover: Velocity-streamlines from an incompressible simulation using SST-DES illustrating the flow around the roofbar of the Volvo H1-truck.

Chalmers Reproservice
Gothenburg, Sweden 2013

Aeroacoustic study on the roofbar of truck using CFD

Erik Johansson

Department of Applied Mechanics
Division of Fluid Dynamics
Chalmers University of Technology

Abstract

Aeroacoustic CFD-simulations around a roofbar on a Volvo FH-series truck were performed with the purpose to find a method of how to perform an aeroacoustic simulation. The simulations included incompressible approaches using Detached Eddy Simulation (DES) with the SST k-ω turbulence-model and Spalart-Allmaras turbulence-model as RANS-models, and Large Eddy Simulation (LES) but also a compressible approach using SST-DES. Turbulence models and compressibility effects were the main scopes of the project.

The domain that was used proved to be unsuitable for both the compressible and the incompressible approach. The compressible case suffered from severe unphysical phenomena and the incompressible approach which removed the phenomena seemed to be too affected by stiff boundary conditions. Widening the domain could have mitigated the effects.

The incompressible DES-cases proved to predict the flow separation point on the roofbar completely different compared to the incompressible LES. Also, turbulent scales could not be entirely developed downstream of the roofbar for the incompressible DES-cases which had a large impact on the acoustic surface sources for these cases. Presumably, the LES separation point could be explained by high turbulent viscosity. The behavior of the separation point cannot be unambiguously explained since measurements have not been done. It is therefore not clear which one of DES or LES that gave the best results, however, future recommendations are based on LES as the reference case.

Among the realistic results only broadbanded noise sources were found.

There were no major differences between SA-DES and SST-DES, however SST-DES showed somewhat closer results to LES and is therefore recommended to be used although it took relatively longer time to perform.

Keywords: Aeroacoustics, CAA, LES, DES, incompressibility, compressibility, truck, roofbar, cavity, hatch

Preface

This project was carried out at the cabin analysis department at Volvo Group Trucks Technology during the period January to June 2013 as the final part of the Master's programme Applied Mechanics. This thesis contains the final results of the project. The aim was to perform an aeroacoustic analysis of the roofbar attached onto the roof of one of the trucks in the Volvo FH-series. The simulations were performed at the computer cluster of AB Volvo.

The industrial supervisor for the project was Ph.D. Zenitha Chronéer. The academic supervisor and examiner at Chalmers University of Technology was Professor Lars Davidson, Head of the Division of Fluid Dynamics at the Department of Applied Mechanics.

Acknowledgements

I would first like to thank my industrial supervisor Ph.D. Zenitha Chronéer for supervising, guiding and helping throughout the project time. Thanks for giving me the opportunity to come out to the industry and carry out this project.

Thanks to Professor Lars Davidson for providing thoughts and advices and for being supportive.

Thanks to CFD specialists Anders Tenstam and Fredrik Ekeroth for all the discussions about the project and helping with the CFD software.

Thanks to Ph.D. Lars Nordström, Ph.D. Thomas Englund and Anders Hedlund for introducing me to the field of acoustics and helping me out during the signal analysis.

I would like to thank the technical support of CD-Adapco, especially Ph.D. Axel Kierkegaard and Albert Gascón, for helping me out with everything from easy questions to hard questions.

Last but not least, thanks to my girlfriend for always being supportive, understanding and believing in me.

List of abbreviations

BCD	Bounded Central Differencing
CAA	Computational Aeroacoustics
CD	Central Differencing scheme
CFD	Computational Fluid Dynamics
CFL	Courant-Friedrichs-Lewy
DES	Detached Eddy Simulation
DDES	Delayed Detached Eddy Simulation
IDDES	Improved Delayed Detached Eddy Simulation
DFT	Discrete Fourier Transform
DNS	Direct Numerical Simulation
FFT	Fast Fourier Transform
FOU	First Order Upwind scheme
FVM	Finite Volume Method
FW-H	Ffowcs-Williams and Hawkings
LES	Large Eddy Simulation
MSD	Modelled Stress Depletion
NSE	Navier-Stokes Equations
RANS	Reynold-Averaged Navier-Stokes
SA	Spalart-Allmara
SGS	Sub-Grid Scale
SOU	Second Order Upwind scheme
SPL	Sound Pressure Level
SST	Shear-Stress Transport
WALE	Wall-Adapting Local Eddy-viscosity
WMLES	Wall-Modeled LES

Lists of symbols

Greek symbols	
α	Time-delay of vortice-impingements
β^*	Specific dissipation constant
δ	Boundary-layer thickness
δ_{ij}	Kronecker delta
Δ	Cut-off width
ϵ	Dissipation rate
ϕ	Generic flow variable
γ	Specific heat ratio
λ	Wave length
μ	Dynamic viscosity
ν	Kinematic viscosity
ν_T	Turbulent viscosity
$\nu_{T,SGS}$	SGS-viscosity
ω	Specific dissipation rate
Ω	Vorticity
ϕ	Generic flow-field variable
$\langle\phi\rangle$	Filtered variable
ρ	Density
τ_{ij}	Shear stress tensor
τ_{ij}^R	Reynolds stress tensor
τ_{ij}^S	SGS-tensor for incompressible flow
τ_{ij}^{SF}	SGS-tensor for compressible flow
$\tau_{ij,SGS}$	SGS stress tensor
τ_w	Wall shear-stress
θ	Angle
ξ	Generic variable in Fourier transform

Roman symbols	
a_∞	Speed of sound
A_n	Neck-area
C_D	Aerodynamic drag coefficient
C_{DES}	DES constant
C_P	Heat capacity at constant pressure
C_V	Heat capacity at constant volume
$\tilde{d}$	DES length scale
e	Internal energy
E	Internal total energy
f	Frequency or function
$\hat{f}$	Fourier transformed function
$\overline{f}_i$	Body-force
f_H	Helmholtz frequency
f_R	Rossiter frequency
F_i	External force for dipoles
H	Total enthalpy
h_n	neck height
k	Turbulent kinetic energy
ℓ	Turbulent length scale
l^+	Dimensionless transverse coordinate
M	Mach number
n_i	Directional vector in i-direction
n	Number of shear-layers vortices
p	Pressure
$\overline{p}$	Time-averaged pressure
p_{ref}	Reference pressure
p_{rms}	Root-mean-squared pressure
$p^{'}$	Pressure fluctuation
$p^{'}_{mono,di,quad}$	Pressure fluctuation of monopole, dipole or quadrupole
Q	A fluid's mass rate per volume
r	Distance between source and observer
R	Ideal gas constant
Re	Reynolds number
s^+	Dimensionless stream-wise coordinate
$\overline{S}_{ij}$	Time-averaged strain-rate tensor
St	Strouhal number
Δt	Time-step
T	Temperature

Roman symbols	
T_{ij}	Lighthill stress tensor
$\overline{u}_i$	Time-averaged velocity-vector and filtered velocity for LES
$\bar{U}$	Mean velocity
u_i	Instantaneous velocity vector
u_i'	Velocity fluctuation vector
u_∞	Freestream velocity
u^+	Dimensionless velocity
u^*	Friction velocity
ΔV	Finite volume
V_c	Cavity volume
Δx	Cell width
$\mathbf{x}$	Observer-coordinate
x_i	Coordinate in i-direction
y	Wall normal distance
$\mathbf{y}$	Source coordinate
y^+	Dimensionless wall number

Contents

1 Introduction

The aeroacoustic effects on the roofbar of a recently released truck from Volvo Trucks are to be studied using Computational Fluid Dynamics (CFD). This thesis will treat the aeroacoustic effects of the roofbar on a truck, on which e.g. external headlights could be mounted, and is a continuation of the previous years' Master's thesis written by Johan Tell [32]. The proceeding matter will be to build upon Tell's method in how to make aeroacoustic simulations.

1.1 Background

The comfort in the working environment is important for the truck driver in order to withstand the work in the long term. One way to increase the comfort is to reduce the noise emanating from cabin external sources of which there are four: the working engine, the power-train, wheel-road interaction and the exterior details on the truck impinged by air flow i.e. *aeroacoustical noises* [2].

The engine, power-train and wheel-road interaction noises are the major noise contributors. However, since the cabin has succesfully become more and more isolated from these noises, the aeroacoustic noises has incrementally emerged [2] and become more noticeable and it is desirable to identify these.

Volvo Group Trucks Technology (GTT) has fairly low experience regarding simulating aeroacoustics. During spring 2012 a Master's thesis was carried out on this subject. In that thesis, several turbulence models were used and compared for the same geometry. Large Eddy Simulation (LES) was used as well as Detached Eddy Simulation (DES). LES was as expected computationally demanding while the results of DES showed similar results behavior using half of the cell amount compared to LES and thus requiring much less computational effort. However, no validation data existed so the results could not be validated [32].

This thesis aims at finding a decent method in order to perform a successful aeroacoustic simulation.

1.2 Purpose

The purpose of this thesis is to provide Volvo GTT with knowledge about the aeroacoustic effects on the front of a truck in the FH-series focusing on the roofbar. The knowledge obtained comprises not only the actual results from the simulations but also a documented methodology from which future work in aeroacoustics at the company can emanate from.

The reason why Volvo Trucks is in need of this project is that the company has fairly low experience and knowledge about the area of aeroacoustics since these noises have quite recently become more noticeable due to efficient isolation.

The results of the simulations will contain numerous graphs describing the Sound Pressure Level (SPL) for a range of frequencies. Those results will be generated by using

probes deployed at interesting areas that will gather flow information. Also, SPL-values on the surface of the truck will also be part of the results.

1.3 Objectives

The objectives of the thesis are:

- Evaluate the domain used in last years' Master's thesis for the shortest truck model H1 in the Volvo FH-series.
- Use the same domain to compare incompressible and compressible results for aeroacoustics using DES.
- Compare different turbulence models' effect on the acoustic results.

1.4 Delimitations

The delimitations for the project are presented below.

- **Small domain**

  The results that are within the scope of this thesis will have transient behavior and will be generated through transient CFD-simulations in a small domain, comprising a 15 cm slice of the truck cabin along the x-axis. This slice will in turn contain the exterior details of the truck that are presumed to heavily affect the flow around the roofbar.

  The reason why the small domain needs to be created is that for accurate results extremely fine cells need to be adopted but the amount of cells is a constraint for the domain size. High resolution is especially crucial regarding aeroacoustics where resolving turbulent kinetic energy accurately is essential.

- **1D inlet velocity**

  A large windtunnel domain will be used in which the small domain is located. The inlet velocity of the larger domain is 90 km/h and in the positive x-direction which means that the air will flow in the truck's opposite direction of travel.

- **Time**

  The duration of this project is 20 weeks which is a fairly short period for a project of this magnitude. This will be especially significant since there is only one student working on this project.

- **Far-field noise**

  The noise generated will not be investigated at large distances from an observers' location where turbulence is absent or could be neglected, i.e. far-field simulations, but only in the proximity of the truck since it is the noise perceived by the truck driver that is of interest.

- **Cell-amount**

  The cases regarding DES had a specified restriction on approximately 5 million cells while the amount of cells specified for LES were less strict.

2 Theory

In this section the theory relevant for this project will be treated. It includes theory on fluid mechanics, turbulence modeling, aeroacoustics and signal processing.

2.1 Fluid mechanics

Here relevant theories of fluid mechanics will be described.

2.1.1 Governing equations

Below the governing equations of compressible and incompressible flows are treated.

2.1.1.1 Compressible fluids

The governing equations needed to fully describe a compressible Newtonian fluid such as air is described by Eqs. (2.1a)-(2.1c):

$$\frac{\partial \rho}{\partial t} + \frac{\partial (\rho u_i)}{\partial x_i} = 0 \tag{2.1a}$$

$$\frac{\partial (\rho u_i)}{\partial t} + \frac{\partial (\rho u_i u_j)}{\partial x_j} = -\frac{\partial p}{\partial x_i} + \frac{\partial \tau_{ij}}{\partial x_j} \tag{2.1b}$$

$$\frac{\partial (\rho E)}{\partial t} + \frac{\partial (\rho u_i H)}{\partial x_i} = \frac{\partial (u_i \tau_{ij})}{\partial x_j} + \frac{\partial}{\partial x_j}\left(k \frac{\partial T}{\partial x_j}\right) \tag{2.1c}$$

where Eq. (2.1a) is the continuity equation, Eq. (2.1b) the Navier-Stokes equations and Eq. (2.1c) the energy transport equation.

In Eq. (2.1b), which describes the motion of fluids, the stress-tensor τ_{ij} defined by:

$$\tau_{ij} = 2\mu S_{ij} - \frac{2\mu}{3}\frac{\partial u_k}{\partial x_k}\delta_{ij}$$

in which

$$S_{ij} = \frac{1}{2}\left(\frac{\partial u_i}{\partial x_j} + \frac{\partial u_j}{\partial x_i}\right)$$

is the strain-rate tensor [3].

In the energy equation (2.1c) Fourier's law is present inside the last term which is the most common way to model the heat flux. The quantities E and H are the total energy and the total enthalpy respectively defined as:

$$E = e + \frac{1}{2}u_i u_i; \qquad H = h + \frac{1}{2}u_i u_i = E + \frac{p}{\rho}$$

in which for a calorically perfect gas

$$e = C_V T; \qquad h = C_P T$$

for which the heat capacities C_P and C_V are constant.

A calorically perfect gas would imply that the ideal gas law

$$p = \rho RT \tag{2.2}$$

can be used as the equation of state in order to thermodynamically link the pressure with the density and thereby making Eqs. (2.1a) - (2.1c) to vary dependently on each other. Using Eq. (2.2) also leads to a relation between e and h:

$$h = e + RT$$

It now becomes obvious that Eqs. (2.1a)-(2.1c) and Eq. (2.2) together constitute a coupled system of equations that have to be solved simultaneously. In total there are six unknown scalars for this system of equations: temperature, density, pressure and velocity components in three directions.

2.1.1.2 Incompressible fluids

Incompressible Newtonian fluids are more easily described than compressible fluids. The fact that the density is constant gives changes to the governing equations (2.1a) and (2.1b) as follows:

$$\frac{\partial u_i}{\partial x_i} = 0 \tag{2.3a}$$

$$\frac{\partial u_i}{\partial t} + u_j \frac{\partial u_i}{\partial x_j} = -\frac{1}{\rho}\frac{\partial p}{\partial x_i} + \nu \frac{\partial^2 u_i}{\partial x_j^2} \tag{2.3b}$$

With the assumption of incompressibility the equation of state can no longer be used link the pressure with the density. This implies that the energy equation is no longer coupled with equation (2.3a) and (2.3b). The two latter equations can thus be solved without the energy equation since the properties of the fluid is not a function of the temperature anymore. This results in four remaining unknown scalars; pressure and three velocity components.

2.1.2 Relevant dimensionless numbers of fluid mechanics

Dimensionless numbers used to describe the characteristics of a fluid are presented here.

2.1.2.1 Reynolds number

The Reynolds number is the ratio of the inertial and viscous forces and thereby acts as an indicator of whether a flow is expected to be laminar or turbulent, regardless of the type of fluid considered.

$$Re = \frac{\rho u_\infty L}{\mu} \tag{2.4}$$

The Reynolds number for the point of transition between the flow types changes depending on whether the flow transitions from turbulent to laminar flow or vice versa.

2.1.2.2 Strouhal number

The Strouhal number is the ratio of the flow's inertial forces caused by the oscillating flow and the inertial forces due to the local flow velocity.

$$St = \frac{fL}{u_\infty} \tag{2.5}$$

Experiments for e.g. flows around a cylinder show that the Strouhal number approximately equals 0.21 for a wide range of Reynolds numbers [7]. This value is useful in order to estimate the frequency f at which e.g. a tonal peak caused by vortex shedding is located at in a frequency spectrum.

2.1.2.3 Mach number

The Mach number M is a dimensionless number used to compare the local speed of an object to the local speed of sound:

$$M = \frac{|u_i|}{a_\infty}$$

Physically it describes the ratio between the flow's intertial force and compressibility force. The Mach number also functions as an indicator of if the flow itself can be regarded as a compressible or an incompressible flow. For $M < 0.3$ air could be regarded as an incompressible fluid. This is because compressibility then has a marginal effect on the flow behavior [1].

2.1.3 Turbulent flow

When the Reynolds number for a flow increases and reaches a critical value the flow changes from laminar flow to turbulent flow. Laminar flows are characterized by shear-layers that slide past each other without mixing and can for a few assumptions of the flow, e.g. between two plates, be described by an analytical parabolic equation. In turbulence these shear layers are instead mixed. Turbulent flow has a number of characteristic properties. Some of them are:

- **Randomness**

  Turbulence has an irregular, unpredictable and stochastic behavior.

- **Vorticity and dissipation**

  Turbulence contains vorticity which vector is defined by:

  $$\omega_k = \frac{\partial}{\partial x_j} \times u_i = \epsilon_{ijk} \frac{\partial u_i}{\partial x_j}$$

  and locally describes the rotation of a fluid particle. ϵ_{ijk} is the Levi-Civita symbol. The equation above will always describe three dimensions as a consequence of the cross product. Physically this means that a fluid element will be affected by vortex tilting and vortex stretching which create vorticity in a third coordinate direction.

  Rotational structures of the flow are called *eddies* which are defined by a length scale ℓ. The largest eddies extract kinetic energy from the mean flow and have a length scale of the size of the region of turbulence. The larger eddies transfer part of their kinetic energy nonlinearly to smaller eddies in what is referred to as the *cascade process*. When the energy finally reaches the smallest eddies the energy is dissipated into heat although relatively small fractions of energy is in fact dissipated through the entire process. The smallest eddies are referred to as *Kolmogorov scales* and are isotropic.

- **Diffusivity**

  In turbulent flow there is an increased rate of mixing of the flow in order for the flow to become more homogeneous. Also, the governing properties of a fluid i.e. mass, momentum and energy is transported at an increased rate. This is referred to as *diffusivity*.

- **High Reynolds numbers**

  Turbulence occurs at high Reynolds numbers. For a plate the switch in boundary-layers (see section 2.1.4) are occurring at $Re \approx 250{,}000$ [35].

2.1.4 Boundary-layers

The boundary-layer is the thin layer of fluid closest to an impermeable surface which a fluid flows past. Inside the layer the velocity drops rapidly and the viscous forces are substantial for the behavior of the flow. At the wall the so called *no-slip condition* applies which means that the velocity is zero. Farther away from the wall the velocity increases. Finally, when the velocity is 99 % of the freestream velocity u_∞ the point of transition from the boundary-layer to the freestream flow is reached where the thickness of the boundary-layer is δ. Depending on the geometry's shape and flow type different thicknesses will be obtained. For a flat plate with length x the approximate thicknesses

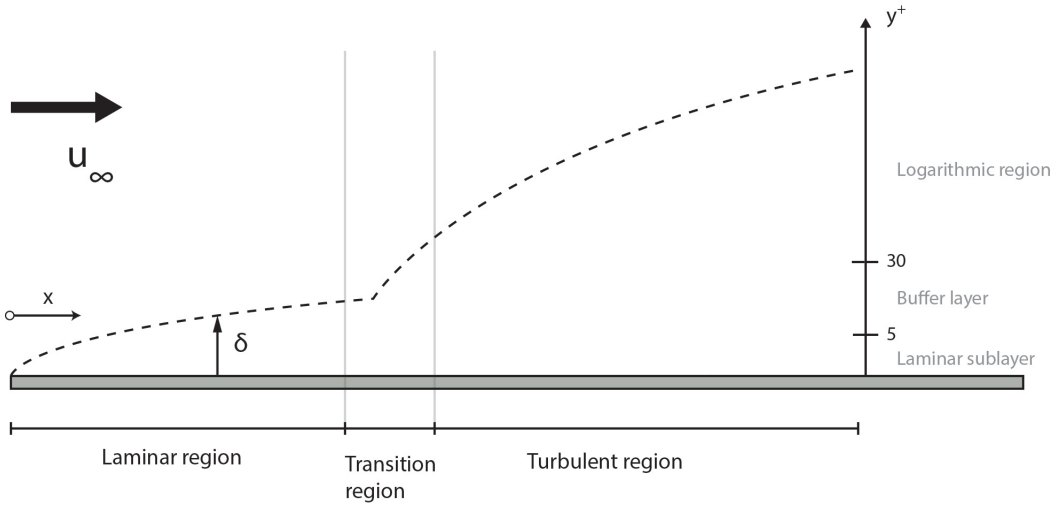

Figure 2.1: Schematic illustration of a boundary-layer. Note the axis for y^+ to the right.

of laminar and turbulent boundary-layers are [35]:

$$\frac{\delta}{x} = \frac{5}{\sqrt{Re_x}} \qquad \text{(Laminar)} \tag{2.6a}$$

$$\frac{\delta}{x} = \frac{0.385}{Re_x^{1/5}} \qquad \text{(Turbulent)} \tag{2.6b}$$

Laminar boundary-layers exist only for low Reynolds numbers. As the distance x grows the boundary-layer will be thicker until the point where the flow reaches the transition region, see Figure 2.1. In the transition region the flow will fluctuate between laminar and turbulent flow and if the distance x increases further the flow will reach the turbulent region in which the flow almost always will be turbulent. However, closest to the wall inside the boundary-layer there will be a thin film referred to as the *viscous sub-layer* in which the flow will be dominated by viscous forces. The boundary-layer consists apart from the viscous sub-layer also by the *buffer-region* and the *logarithmic region*. These are shown in Figure 2.1. The three regions mentioned always occur on a certain *dimensionless wall-distance* y^+ which is defined as:

$$y^+ = \frac{u^* y}{\nu} \tag{2.7}$$

where u^* is the friction velocity, y the distance normal to the wall and ν the kinematic viscosity. The friction velocity is in turn defined as:

$$u^* = \sqrt{\frac{\tau_w}{\rho}}$$

where τ_w is the wall shear-stress. Using the y^+-value laws for the regions inside the boundary-layer a velocity profile can be derived though not for the buffer-layer.

The dimensionless quantity y^+ will play a crucial part in CFD simulations as will be seen later.

2.2 Turbulence modeling

The most desirable way to describe turbulent flow numerically is to perform a Direct Numerical Simulation (DNS) in which the Navier-Stokes equations are numerically solved without any simplifications. However, this method is today practically out of reach because of the enormous amount of grids required to resolve even the Kolmogorov scales. Exceptions are simple flows with low Reynolds numbers [3]. Therefore, simpler methods by the mean of approximations of the Navier-Stokes equations need to be used.

Turbulence models are mainly divided into models based on Reynolds-Averaged Navier-Stokes equations, hybrid models, Large Eddy Simulation (LES) and Direct Numerical Simulation (DNS) [33]. Presented below are RANS-based eddy-viscosity models, LES and DES which are the models used in the simulations carried out in this thesis.

2.2.1 Reynolds Averaged Navier-Stokes (RANS)

One approach of approximating turbulent flow is Reynolds-averaging or time-averaging, first presented by Osborne Reynolds during the 19^{th} century. The idea was to decompose the instantaneous flow into one time-averaged part $\overline{u}_i$ and one fluctuating part $u_i^{'}$:

$$u_i = \overline{u}_i + u_i^{'}$$

Time-averaging is applied for incompressible flows and by averaging the Navier-Stokes equations that contain the decomposed velocity vector the following equation is obtained which is referred to as the Reynolds-Averaged Navier-Stokes (RANS) equation (cf. equation (2.3b)):

$$\rho\overline{u}_i\frac{\partial\overline{u}_j}{\partial x_i} = \frac{\partial}{\partial x_j}\left[-\delta_{ij}\overline{p} + \mu\left(\frac{\partial\overline{u}_i}{\partial x_j} + \frac{\partial\overline{u}_j}{\partial x_i}\right) - \rho\overline{u_i^{'}u_j^{'}}\right] \tag{2.8}$$

Note the disappearance of the transient term as well as the appearing term $-\rho\overline{u_i^{'}u_j^{'}}$ which is referred to as the *Reynolds stress-tensor*. This tensor describes the turbulent fluctuations' effect on the change in momentum of the fluid.

When considering a compressible fluid Favre mass-averaging, i.e. density-weighting, is applied partly instead of time-averaging. Most easily Favre-averaging is applied on all quantities except pressure and density on which time-averaging is instead used. This is further described in [33] and [3].

The aim of the eddy-viscosity RANS-models is to model the turbulent viscosity (also eddy-viscosity) ν_T which when added together with the laminar viscosity ν_L gives the total viscosity ν of the fluid.

There are numerous types of RANS-models within the group of eddy-viscosity models. They are based on the assumption that the turbulent viscosity interacts with the Reynolds stresses. The procedure of computing the Reynold-stresses is what separates different RANS-based models. For RANS-models of the first order the turbulent viscosity is assumed to be linearly dependent on the Reynolds-stresses following the Boussinesq assumption [25]:

$$\tau_{ij}^R = -\rho\overline{u_i'u_j'} = 2\mu_T\overline{S}_{ij} - \frac{2\rho k\delta_{ij}}{3}$$

where $k = \frac{1}{2}\overline{u_i'u_i'}$ is the turbulent kinetic energy and $\overline{S}_{ij} = \frac{1}{2}\mu\left(\frac{\partial\overline{u}_i}{\partial x_j} + \frac{\partial\overline{u}_j}{\partial x_i}\right)$ is the time-averaged strain-rate tensor [3].

In this thesis two RANS-based linear eddy-viscosity models are used: a one-equation model and a two-equation model are used. They will be briefly described below.

2.2.1.1 Spalart-Allmaras one-equation model

Spalart-Allmaras (SA) one-equation model utilizes a viscosity-reminding quantity $\tilde{\nu}$ to define the eddy-viscosity ν_T:

$$\nu_T = f_{\nu 1}\tilde{\nu} \tag{2.9}$$

where $f_{\nu 1}$ is a wall-damping function.

Since SA is a one-equation model it cannot compute the length scale. This must however be computed in order to determine the rate of dissipation due to turbulence. Instead of computing the length scale it is estimated by using the wall distance y multiplied by a modified von Karman constant $\kappa = 0.4187$.

Despite that SA is a one-equation model it shows better results than two-equation models such as the k-ϵ model and the k-ω model regarding external aerodynamics. However, for complex geometries such as in internal flows the model can face difficulties with defining length scales which results in poor predictions [33].

For details on the SA-model such as the transport equation, see [27].

2.2.1.2 SST Menter's k-ω two-equation model

The Menter's Shear Stress Transport k-ω two-equation model is simply a hybrid of the k-ϵ model and the k-ω model. SST combines the best of both models. The k-ω-model makes excellent predictions of the boundary-layer except for in the outer region. However, the model shows a strong dependence on the freestream value of the specific dissipation rate ω:

$$\omega = \frac{\epsilon}{k\beta*} \tag{2.10}$$

The k-ϵ model is a poor predictor of the boundary-layer since the shear-stress is over-predicted, especially for adverse pressure gradients, and the model is therefore used in the free shear-layers of the flow where it has proven to be accurate [3]. Another disadvantage is that a low Reynolds number damping-function needs to be specified close to the wall.

The SST-model has an improved function for calculating the eddy-viscosity in order to better predict adverse pressure gradients and detachment of the boundary layer caused by pressure. It is a general model that can handle complex flows [33].

The turbulent eddy-viscosity in the SST-model is defined as follows:

$$\nu_T = \frac{a_1 k}{max(a_1\omega, S_{ij}F_2)} \tag{2.11}$$

where a_1 is a constant and F_2 is a blending function. Blending function F_1 appears in the transport equation for ω. The specific dissipation rate ω is together with the kinetic energy k the transported variables in the SST-model. For more details on the SST-model such as the two transport equations, see [19].

2.2.1.3 Appropriate convective discretization scheme for RANS-models

When modeling RANS-models the appropriate convective discretization schemes to use are the upwind schemes of different orders depending on the complexity of the flow. Since the equations are averaged the details of the instantaneous flow vanish. Even if the details would have been left the upwind schemes are considered to be too numerically dissipative, i.e. the schemes smear out the solution due to that the values at the cell faces determine the cell values in, for instance, the downstream direction [3].

2.2.1.4 Wall treatment

A solution considered as valid needs to fulfill the requirement of $y^+ \leq 1$ closest to the walls. Another possibility if less grids are desired is to use wall functions so that the previously stated requirement is less strict.

2.2.2 Large Eddy Simulation (LES)

In the transient numerical method Large Eddy Simulation (LES) the eddies of a turbulent flow are categorized by the use of a cutoff width Δ so that the smaller eddies have a length scale $\ell \leq \Delta$ and consequently the larger eddies have a length scale $\ell > \Delta$.

The larger eddies exhibit a more anisotropic behavior and are substantially dependent on the shape of the geometry. The larger eddies also interact and extract energy from the mean flow and are therefore important to resolve sufficiently. Thus, DNS is applied to capture the motion of the larger eddies. Contrary to the larger eddies the smaller ones exhibit isotropic properties which make them ideal to model with a so called Sub-grid scale (SGS) model [33].

2.2.2.1 Spatial filtering

In order to achieve the division of eddies a spatial filter function $G(\mathbf{x},\mathbf{x}',\Delta)$ is applied to the Navier-Stokes equations:

$$\overline{\phi}(\mathbf{x},t) = \int_{-\infty}^{\infty}\int_{-\infty}^{\infty}\int_{-\infty}^{\infty} G(\mathbf{x},\mathbf{x}',\Delta)\phi(\mathbf{x}',t)\mathrm{d}x_1'\mathrm{d}x_2'\mathrm{d}x_3' \tag{2.12}$$

where ϕ is the unfiltered and $\overline{\phi}$ the filtered flow variable. Δ is the cutoff width which is set to a length at which the larger and smaller eddies are separated, commonly $\Delta = (\Delta x, \Delta y, \Delta z)^{1/3}$ [33].

The top-hat filter, Gaussian filter and Spectral cutoff filter are the most common filters used for LES. More can be read about them in [33].

The spatially filtered incompressible Navier-Stokes equations read:

$$\frac{\partial \overline{u}_i}{\partial t} + \frac{\partial}{\partial x_j}\left(\overline{u}_i \overline{u}_j\right) = -\frac{\partial \overline{p}}{\partial x_i} + \nu \frac{\partial^2 \overline{u}_i}{\partial x_j^2} - \frac{\partial \tau_{ij}^S}{\partial x_j} \tag{2.13}$$

where τ_{ij}^S is the so called *SGS-tensor*. The reader is referred to [3] for the filtered equations for compressible fluids.

2.2.2.2 Subgrid scale (SGS) models

The SGS-model used in an LES-simulation is primarily used to describe the transfer of energy between the larger and smaller eddies and is implemented to dissipate the larger scales. The transfer is described by the SGS-tensor that appears in Eq. (2.13) due to the non-linearity of the diffusion term [3]:

$$\tau_{ij}^S = \overline{u_i u_j} - \overline{u}_i \overline{u}_j \qquad \text{(Incompressible fluid)} \tag{2.14a}$$

$$\tau_{ij}^{SF} = \overline{\rho}(\widetilde{u_i u_j} - \widetilde{u}_i \widetilde{u}_j) \qquad \text{(Compressible fluid)} \tag{2.14b}$$

where superscript F and the tilde indicate Favre mass averaging. Note that the density is time-averaged and the velocity vector is Favre mass-averaged.

The first SGS-model was the *Smagorinsky-model* in which the Boussenisq assumption was thought to be reasonably valid so that a linear relationship persist:

$$\tau_{ij}^S = 2\nu_{T,SGS}\overline{S}_{ij} \tag{2.15}$$

where $\nu_{T,SGS}$ is the SGS-viscosity defined by:

$$\nu_{T,SGS} = (C_S\Delta)^2\sqrt{\overline{S}_{ij}\overline{S}_{ij}} \tag{2.16}$$

In equation (2.16) C_S is the Smagorinsky-constant which is often assigned values in the interval 0.065-0.25 depending on the features of the flow and the geometry [20, 15].

The Smagorinsky-model only predicts dissipation of energy and does not cover the phenomenon of *backscattering* which essentially means that energy does not travel solely from larger eddies to smaller eddies but also in the opposite direction. Also, the model requires a wall-damping function in order to accurately predict the wall-bounded flow.

Dynamic SGS-models use the same relationship (2.15) as the original Smagorinsky formulation. The difference is that the Smagorinsky-constant C_S is substituted by C_d which is a dynamic SGS-function. C_d is determined by applying a test-filter, after the filter-function G, that has to be larger than the cut-off width Δ.

The SGS-model used in this thesis for the pure LES-simulations is the *Wall-adapting Eddy-viscosity model* (WALE). As the original Smagorinsky-model it uses an SGS-constant C_w. However, the WALE-model is not sensitive to this constant and is good at predicting wall-behavior with a relatively small computational effort [6].

2.2.2.3 Wall treatment

Close to the wall, as for the wall-function free RANS-models, LES needs to have a near-wall grid resolution of $y^+ \leq 1$ in order to achieve an adequate solution. However, LES also have resolution requirements in the stream-wise direction

$$50 \leq s^+ \leq 150$$

and transverse direction according to Piomelli et al. [21]

$$15 \leq l^+ \leq 40$$

This implies a large amount of grids needed to give an adequate solution which is a drawback with LES. This is especially significant close to the wall when the boundary-layer is resolved. Since DNS is used on every grid until the point at which the turbulent length-scale ℓ is smaller than the cutoff width Δ where the SGS-modeling starts, extremely small grids are needed in order to accurately resolve the scales of the boundary-layer.

In the case of high Reynolds-numbers a wall-function is implemented.

2.2.2.4 Appropriate convective discretizing scheme for LES

The appropriate discretization scheme for LES is the second order accurate Central Differencing (CD) scheme. This is because the scheme is able to preserve turbulent kinetic energy which the upwind schemes cannot since they are too numerically dissipative. However, central differencing itself is not a bounded method which therefore allows for overshooting and undershooting values at the cell faces when convection dominates over diffusion, making the solution unstable. The Bounded Central Differencing (BCD) scheme utilizes a boundedness criterion so that when satisfied uses CD blended with Second Order Upwind (SOU) scheme and if not satisfied uses the First Order Upwind (FOU) scheme. BCD has the feature of the robustness of the upwind schemes and the accuracy of CD.

2.2.3 Detached Eddy Simulation (DES)

LES clearly is much less computationally demanding than DNS, however it is still too demanding to have a vast applicability and is with today's computers constrained only to low Reynolds-number flows in the case of when the entire boundary-layer is resolved.

In order to achieve a high numerical accuracy together with even less demanded computer power a hybrid RANS-LES model was developed so that an unsteady RANS-model

(URANS) is used for shear-layers and LES is used for unsteady regions such as when the flow separates from a solid boundary [27]. This is referred to as *Detached Eddy Simulation* (DES). Spalart-Allmaras model and the SST k-ω-model are two RANS-models that were modified for DES. The reason why these two were chosen to be implemented in DES was their high accuracy of estimating the point of flow separation [19].

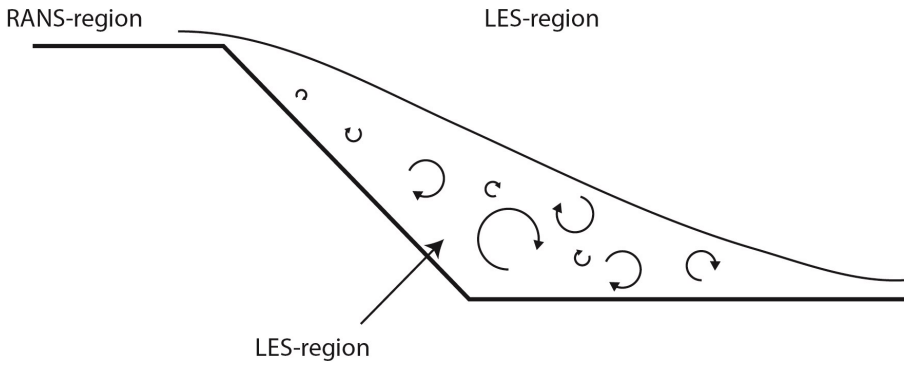

Figure 2.2: Schematic illustration of DES. Note that RANS is also activated inside the boundary-layer of the separated region even though it is not shown in the figure.

The point of switch between RANS and LES for the SA-model is determined by letting the distance to the nearest wall represent the length scale

$$\tilde{d} = min\left[d, C_{DES}\Delta\right] \tag{2.17}$$

where d is the wall distance and C_{DES} is a constant which usually is set to 0.65, however, the value depends on the flow.

The SST-model is slightly adjusted with a damping function F_{DES}:

$$F_{DES} = max\left(\frac{\ell}{C_{DES}\Delta}, 1\right) = max\left(\frac{\sqrt{k}}{C_{DES}\Delta\beta * \omega}, 1\right)$$

where ℓ is the turbulent length scale. F_{DES} is then implemented into the definition of the specific dissipation rate (cf. equation (2.10)):

$$\omega = F_{DES}\frac{\epsilon}{\beta^* k} \tag{2.18}$$

One problem with the DES-formulation occurs at the point of switch from RANS to LES. Especially in the case of carelessly generated meshes and thick boundary layers the cell size in the boundary-layer tangential to the wall could get less than the boundary-layer thickness. It is then a certain risk of a so called *Modeled Stress Depletion* (MSD) which essentially means that the switch from RANS to LES takes place inside the boundary-layer where only RANS should be activated. Thus, the turbulent

viscosity may be underestimated and consequently the skin-friction coefficient also becomes underestimated which could cause a premature separation point. A solution to MSD was presented by Spalart et al. (2006) [28]. The proposed *Delayed DES* (DDES) essentially utilizes a shielding function to preserve RANS in the entire boundary-layer. Two years later Shur et al. (2008) [26] presented an *improved DDES* (IDDES) which contains an LES wall-model (WMLES). IDDES has the feature of treating the boundary-layer flow in two ways: if the boundary-layer flow contains turbulent content only the part of the boundary-layer closest to the wall is assigned for RANS-modeling while the rest is modeled using WMLES. This requires that the boundary-layer inflow is turbulent and that the grids are satisfactorily fine for turbulence. If the requirements are not met ordinary DDES will be performed.

2.2.3.1 Appropriate convection scheme for DES

In Strelets [31] it was suggested that the RANS-regions and the LES-regions should be treated with different convective discretization schemes. His conclusion was to use BCD in the separated areas and a high-order upwind scheme in the flow-attached and freestream areas. The correspondent boundary condition in StarCCM+ is the *Hybrid BCD* in which the SOU scheme blends with the BCD scheme.

2.2.4 Dimensionless numbers in CFD

Here, dimensionless numbers relevant for CFD-simulations are presented.

2.2.4.1 Courant-Friedrich-Lewy number

The Courant-Friedrich-Lewy number, or CFL-number, is a local stability criterion for transient simulations and is defined by:

$$CFL = \frac{u\Delta t}{\Delta x} \leq 1 \tag{2.19}$$

It is the ratio of the length that a fluid particle travels during one time-step and the cell-size. If the particle's travel length during the time-step is longer than the cell-size, the cell-size is too small for the effective time-step and the time-step have to be decreased in order to reach the desired value $CFL = 1$. The appropriate time-step could therefore easily be chosen if there is a desired cell-size and the local velocity is known.

2.2.4.2 Wall distance y^+ in CFD

In order to accurately resolve a flow close to a solid boundary a certain near-wall normal distance is required. This distance is the normal length of the closest cell to the wall. A normalized length value based on the distance y, friction velocity u^* and kinematic viscosity ν is again the y^+-value:

$$y^+ = \frac{u^* y}{\nu} \tag{2.20}$$

2.3 Aeroacoustics

Aeroacoustics is the field of flow-induced sound generation and resonance. For vehicles Stapleford et al. [30] divided the flow-induced noises into three main parts:

- Unpitched noise - caused by air that flows past the vehicle externally.
- Monotone noise - caused by flow over gaps and sharp edges.
- Acoustic resonance - caused by various openings on the vehicle in which resonance is allowed to develop.

In this section a brief description of the area of aeroacoustics and Computational Aeroacoustics (CAA) will be given.

2.3.1 What is sound?

Sound is defined as mechanical vibrations propagating through a medium and which are perceived by an observer. The medium could be any of the states of matter but only gas will be covered here. The range of frequencies perceived by a human lies between 20 Hz to 20,000 Hz. However, the ears' sensitivity to sound decreases significantly below 100 Hz and above 10,000 Hz [23].

2.3.1.1 Definition of speed of sound

The speed of sound is dependent on the isentropic change in pressure over density:

$$a_\infty = \sqrt{\left(\frac{\partial p}{\partial \rho}\right)_s} = \sqrt{\gamma RT} \tag{2.21}$$

where γ is the specific heat ratio defined by:

$$\gamma = \frac{C_P}{C_V}$$

For a static temperature of $T = 300°\text{K}$, a specific heat ratio of $\gamma = 1.4$ and a gas constant of $R = 287\ \text{J}/(kg \cdot K)$ the speed of sound for air is $a_\infty = 347.2$ m/s.

2.3.1.2 Wave equation

In order for sound to propagate through a fluid medium the fluid needs to be compressible. As mentioned Eq. (2.1a) and Eq. (2.1b) describes the motion of a fluid. When sound propagates through the medium the speed of sound a_∞ needs to be accounted for since sound is pressure waves propagating with speed a_∞. By neglecting the diffusion term in Eq. (2.1b) and assuming isentropy, Eq. (2.1a), (2.1b) and (2.21) together become the *homogeneous wave equation* for acoustics:

$$\frac{\partial^2 \rho}{\partial t^2} - a_\infty \frac{\partial^2 \rho}{\partial x_i^2} = \Box^2 \rho = 0 \tag{2.22}$$

where $\Box^2$ is the d'Alembert operator. This equation describes the propagation of sound through a compressible medium which is the case for a medium at rest not affected by any external stress field. In a region with turbulence $\Box^2 \rho \neq 0$ and under certain assumptions the wave equation is by definition *inhomogeneous* which effect will be described in Section 2.3.4.1.

2.3.1.3 Sound Pressure Level

The human sound perception is logarithmically dependent on the pressure fluctuation as follows:

$$SPL = 10log_{10}\left[\left(\frac{p_{rms}^{'}}{p_{ref}}\right)^2\right] \tag{2.23}$$

where $p_{rms}^{'}$ is the root mean square value of the static pressure fluctuations and $p_{ref} = 2 \cdot 10^{-5}$ Pa is the reference pressure corresponding to to what a human being can perceive between the most sensitive frequency range $1{,}000 < f < 3{,}000$ [23]. It is obvious from equation (2.23) that the larger the pressure fluctuations the larger p_{rms} will be and thus the larger SPL-values.

Since the human ear perceives less below 100 Hz and above 10,000 Hz this can be accounted for by using *A-weighted SPL* which simply filters low and high frequencies so that the SPL-curve becomes a human perception-like SPL-curve and is given in dB(A) [23].

2.3.2 Acoustic sources

Any source in a volume that generates oscillations gives rise to sound. There are different types of sources that sounds emanate from: *monopoles*, *dipoles* and *quadrupoles* are three examples. Their features will be described below.

2.3.2.1 Monopoles

A monopole acoustic source is the strongest type of the acoustic sources and is defined as:

$$\Box^2 \rho = \frac{\partial Q}{\partial t} \tag{2.24}$$

in which Q is is the fluid's mass rate per volume.

The source acts as a pulsating sphere and radiates the sound uniformly in every direction. The source could be defined as any acoustic source which wave-length is large

compared to the characteristic dimensions of the monopole [23]. A typical example of a monopole distribution is resonance phenomena. According to Crighton [8] the pressure fluctuation of the monopole is dependent on the velocity roughly as follows:

$$p'_{mono} \propto u^2 \tag{2.25}$$

2.3.2.2 Dipoles

A dipole source consists of two identical monopole sources that alternately expand and contract. The result is a less effectively radiated sound field since the two resulting pressure fields are out of phase and cancels completely at an angle of $\theta = 90°$. Crighton [8] showed that an external force field acting on the fluid is exactly the same as a dipole source:

$$\Box^2 \rho = -\frac{\partial F_i}{\partial x_i} \tag{2.26}$$

When a solid boundary is struck by a flow the net force of the solid boundary acting on the fluid is what is generating a sound.

Crighton [8] showed its proportionality to the velocity and Mach number M to be roughly as follows:

$$p'_{di} \propto u^2 M \tag{2.27}$$

Curle [9] showed also that dipole sources are the most dominating sources for low Mach numbers.

2.3.2.3 Quadrupoles

Quadrupoles radiate sound even less efficiently than dipoles do. Quadrupoles consist of two pairs of identical dipoles. They could either exist in a *lateral state* (array) or in an *longitudinal state* (linear). The forces are, as in the case of dipoles, of equal magnitude and in opposite adjacent to one another. This corresponds to a pressure-stress in the lateral case and a shear-stress in the longitudinal case which is equivalent to an external stress-field T_{ij} so that:

$$\Box^2 \rho = \frac{\partial^2 T_{ij}}{\partial x_i \partial x_j} \tag{2.28}$$

As for the case of the monopoles and the dipoles Crighton [8] showed the quadrupoles dependence on the velocity and Mach number:

$$p'_{quad} \propto u^2 M^2 \tag{2.29}$$

Comparing Eq. (2.29) with Eq. (2.27) it is seen that quadrupoles gives less pressure fluctuations for $M \ll 1$ meaning less sound emitted. Obviously for Mach numbers close

to unity and above, quadrupoles becomes significantly more important than for low Mach numbers.

2.3.3 Aeroacoustics of cavity flows

The flow-induced noise over a cavity is a case that has been subject to many studies since it has a vast applicability in the vehicle industries. Two types of equation describing the plausible noises emanating from the cavity will be considered; *Helmholtz equation* and *Rossiter' equation*.

2.3.3.1 Helmholtz resonator

The Helmholtz resonator is an everyday phenomena mostly recognized for when blowing air over a bottle-neck which gives rise to a clear tone by resonance. This tone is of monopole type. It occurs when the air flows past an orifice that serves as the opening to a finite volume.

The Helmholtz resonance frequency is computed by:

$$f_H = \frac{a_\infty}{2\pi}\sqrt{\frac{A_n}{V_c h_n}} \tag{2.30}$$

where A_n is the neck-area, h_n the neck height and V_c the cavity volume.

2.3.3.2 Rossiter's model

A flow over, for instance, a simple rectangular cavity is characterized by unsteady motions inside the cavity that actually are self-sustained in the sense that a feedback-loop is created. When the free shear-layer flow flows past the leading edge of the cavity vortex shedding is created which creates a vortex that is transported to the trailing edge where it impinges onto the wall. This impingement leads to an acoustic wave that travels upstream and interacts with the free shear-layer flow which leads to the development of a Kelvin-Helmholtz instability at the interface between the grazing flow and the slower cavity flow which in turn triggers the creation of a new vortex further downstream.

Rossiter [24] developed a semi-empirical model which helps to estimate the frequency of the tone created at the trailing edge of the cavity flow which simply reads:

$$St = \frac{f_R L}{u_\infty} = \frac{n - \alpha}{u_\infty/u_v + M} \tag{2.31}$$

where n is the amount of vortices in the shear layer, α represents the delay in time between when the vortex hits the trailing edge and when the acoustic pressure wave is created and u_v represents the velocity of the vortex.

Brennberger [5] found as a result when sun-roof buffeting was studied that α could usually be neglected. This leads to:

$$f_R = \frac{u_v a_\infty}{L\,(u_v + a_\infty)} \tag{2.32}$$

2.3.4 Computational Aeroacoustics (CAA)

Computational Aeroacoustics (CAA) is the field of computing flow-induced generation of sounds and resonance. Performing a Direct Simulation (DS) would be the ideal way to simulate aeroacoustics since the governing equations of a fluid accounts for acoustic phenomena, however, this is even more computationally demanding than DNS. This is because DS not only requires grid resolution of the order of the Kolmogorov scales but also includes to accurately resolve the transport of sound. Therefore, simpler methods and additional assumptions are desirable. For the purpose scalar equations were developed and *Lighthill's equation* is the original formulation upon various methods have been built upon.

Neither of the models in transient form are actually used in this thesis since the only physical quantity considered and needed for calculating the SPL-values is the pressure fluctuation. This theoretical section serves only as a part of understanding the underlying analytical equations of aeroacoustics.

2.3.4.1 Lighthill's equation

The aerodynamically generated sound is partly governed by the Navier-Stokes equations (2.1b) since the sound is generated by a flow. In 1952 Sir James Lighthill published his article on the subject [18]. His idea was to analytically combine the compressible Navier-Stokes equations (2.1b) and the continuity equation (2.1a) to form a wave equation. By taking the divergence of equation (2.1b), the time derivative of equation (2.1a), combining the equations and rearranging the terms followed by the addition of $a_\infty^2 \frac{\partial^2 \rho}{\partial x_i^2} - a_\infty^2 \frac{\partial^2 \rho \delta_{ij}}{\partial x_i x_j}$ Lighthill's equation is obtained:

$$\frac{\partial^2 \rho}{\partial t^2} - a_\infty \frac{\partial^2 \rho}{\partial x_i^2} = \frac{\partial^2 T_{ij}}{\partial x_i \partial x_j} \tag{2.33}$$

where T_{ij} is the *Lighthill stress tensor* defined as:

$$T_{ij} = \rho u_i u_j + (p - a_\infty^2 \rho)\delta_{ij} - \tau_{ij} \tag{2.34}$$

Note that the right hand side of Eq. (2.33) can be found in the equation for the quadrupole Eq. (2.28). For details on the derivation of Lightill's equation, see [18].

Inside T_{ij} two of the included terms can be neglected. Lighthill argued that for flows of cold jets $(p - a_\infty^2 \rho)\delta_{ij}$ will be small because of absent entropy fluctuations (cf. Eq. (2.21)) and for high Reynolds flow the viscous term τ_{ij} could be neglected. Additionally, $\rho \approx \rho_\infty$ for low Mach numbers [18] where ρ_∞ is the constant atmospheric density. The result is $T_{ij} \approx \rho_\infty u_i u_j$.

Assume that the right hand side of Eq. (2.33) is known and that both sides are independent of each other. The equation could now be described as an inhomogeneous wave equation (cf. Eq. (2.22)), however, only if the surrounding fluid is at rest and isotropic. If so, the right hand side holds the source terms of the acoustics, i.e. the flow-field induced sound, while the propagation of the sound is solely described by the left hand side.

Inside the turbulent region in which Lighthill's analogy applies the density and consequently the pressure act on a quiescent fluid so for density $\rho = \rho_\infty + \rho^{'}$ and pressure $p = p_\infty + p^{'}$. Holding the same assumptions as in order to define the inhomogeneous wave function and by using Green's function Lighthill managed to integrate and find a solution to Eq. (2.33):

$$\rho^{'}(\mathbf{x},t) = \frac{1}{4\pi a_\infty^2} \frac{\partial^2}{\partial x_i \partial x_j} \int_V \left[\frac{T_{ij}}{|r|} \right] \mathrm{d}V(\mathbf{y}) \tag{2.35}$$

where $\rho^{'}(\mathbf{x},t) = \rho(\mathbf{x},t) - \rho_\infty$ and $r = |\mathbf{x} - \mathbf{y}|$ is the distance between the coordinate of sound generation ($\mathbf{x}$) and the coordinate of an observer ($\mathbf{y}$). The integrand is evaluated at retarded time, i.e. the elapsed time for the sound wave to propagate a distance r.

In reality, the assumption of independence between the left and right side stated above is not true. The acoustic field and the flow field are always dependent on each other but to different degrees depending on the characteristics of when the fields interact. For low Mach numbers the interaction can basically be considered as a *one-way coupled* case in which the acoustic field is dependent on the flow field while the flow field is independent of the acoustic field. In a *two-way coupled* case the fields are mutually dependent on each other. Sunroof buffeting is a typical example of such a flow.

Proudman [22] built upon Lighthill's work in order to derive an equation analytically valid for low Mach numbers and isotropic turbulence. In this formulation the acoustic intensity is described by using steady-state quantities making his analogy useful for steady-state pre-simulation studies prior to the transient simulation.

2.3.4.2 Curle's equation

Curle [9] derived an analogy extending from Lighthill's equation that would include sound induced by a solid surface. The surface integral represents the equivalence of a dipole distribution.

$$\rho^{'}(\mathbf{x},t) = \frac{1}{4\pi a_\infty^2} \frac{\partial^2}{\partial x_i \partial x_j} \int_V \frac{T_{ij}}{|r|} \mathrm{d}V(\mathbf{y}) + \frac{1}{4\pi a_\infty^2} \frac{\partial}{\partial x_i} \int_S \frac{n_j}{|r|} \left[p\delta_{ij} - \tau_{ij} \right] \mathrm{d}S(\mathbf{y}) \tag{2.36}$$

Adding the surface integral to Lighthill's equation makes the equation to account for diffraction and reflection by a solid boundary.

2.3.4.3 Ffowcs-Williams and Hawkings equation (FW-H)

This equation is also an extension from Lighthill's equation and accounts for propagation at far-field distances from the acoustic sources. The solid boundary at which sound is generated and reflected are allowed to be in motion. Two different approaches are possible regarding the formulation of the equation. Either an *impermeable surface* can be used in which the geometry of interest is chosen as the sound emitting source or a *permeable surface* can be defined which encloses the region containing acoustic sources - monopoles, dipoles and quadrupoles - and lets the sound to start its acoustic propagation at the permeable surface. For more information, though excluding permeable surfaces, see [11]. For a brief description of the use of the two different surfaces, see [6].

2.4 Signal processing

Signal processing is the field of measuring, analyzing and operating on signals.

In this section the settings used for analyzing the flow-field results from the simulations are briefly explained.

2.4.1 Fourier transform

Fourier transform is a mathematical method used to transform a continuous function $f(x), x \in \mathbb{R}$ into a continuous function that constitutes super-positioned oscillatory functions, each function based on $e^{i\xi x}$, $\xi \in \mathbb{R}$. For one dimension the transformed function is defined by:

$$\hat{f}(\xi) = \int_{-\infty}^{\infty} e^{-i\xi x} f(x) \mathrm{d}x \tag{2.37}$$

A common application of the transform is in signal analysis where the generic variables x and ξ are substituted by time t and frequency ω respectively, i.e. time dependent functions are transformed into frequency dependent functions.

In reality it is not realizable to sample continuous data leading to the use of *Discrete Fourier Transform* (DFT) in which finite vectors $\in \mathbb{C}$ are treated in a similar manner as for continuous functions. The number of operations in DFT are $O(N^2)$, N being the number of samples. By using certain algorithms it is possible to reduce the number of operations from $O(N^2)$ to $O(Nlog_{10}(N))$. These algorithms are what is referred to as *Fast Fourier Transform* (FFT) [12].

2.4.2 Window functions

One consequence when analyzing an assumed periodic signal that is discrete is a so called *leakage problem*. If the assumption of periodicity is not strictly valid for the sampled

signal, energies from the true obtained frequencies of the discrete signal leak into neighboring frequencies leading to a defective frequency spectra. The use of *Window functions* is one way to avoid or mitigate the effect of this problem. It involves a prescribed profile that acts on the time signal before the FFT is made.

In this thesis the so called *Hanning window* is used. More can be read about window functions in [10].

3 Method

3.1 Work-flow

The work-flow of the project can be divided mainly into two parts; creation of the geometry and the simulation process. The meshing process is integrated with the simulation process.

3.1.1 Geometry creation

1. The wind-tunnel with the entire truck inside of it was provided in ANSA-format by the corporation. The same wind-tunnel was also provided for StarCCM+ ready for simulation.

2. In ANSA a plane-cutting tool was used to create a 15 cm thick domain. The same coordinates for the domain's boundary was the same used by Tell [32]. The solid boundaries were divided into smaller parts in order to be able to easily manage the features of the wall.

3. The smaller domain was surface-meshed and then exported from ANSA to StarCCM+ where the pre-processing of the simulations was made.

3.1.2 Simulation process

1. The wind-tunnel domain was meshed.

2. Steady-state simulation for the wind-tunnel domain was made in order to obtain boundary conditions for the smaller domain.

3. The smaller mesh was generated.

4. A steady-state simulation for the smaller domain was made in order to estimate the sound sources with broadband noise models.

5. The smaller mesh was refined at interesting areas both in the volume and at the surface.

6. The transient simulation was made.

7. Post-processing of the transient simulation.

3.2 Software

The softwares that have been used in the project are described in this section.

3.2.1 CFD-software

In this thesis the commercial CFD software Star CCM+ v.8.02.008 developed by CD-Adapco was used for minor geometry operations, meshing, pre-processing, simulating and post-processing. It was also used to make minor changes on the geometry. The software contains many different engineering physics applications such as fluid mechanics, heat transfer, electromagnetism and combustion.

3.2.2 CAD-software

ANSA v.14.1.1 was used to create and modify the geometry of interest.

3.2.3 Numerical computing environments

MATLAB v.7.14 was used for minor calculations that were more complicated to use in StarCCM+.

3.3 Cases examined

In total six simulations were carried out during the project and they are briefly described below. Each case description begins with a case code used to separate the cases from each other.

1. **H1WSST** - The large domain is simulated by the use of steady-state condition and a RANS-model. The results are *mapped* onto the boundaries of the focus domain which means that the values are stored at the boundaries.

2. **H1FVLES** - An incompressible LES-simulation of the focus domain was made for reference purpose since no measure data exist. The method is generally more exact than DES.

3. **H1FVCSSTDES** - DES-simulation of a compressible flow was made with the SST k-ω model.

4. **H1FVSSTDES** - DES-simulation of incompressible flow was made with the SST k-ω model in order to compare it with the correspondent compressible simulation.

5. **H1FVSADES** - DES-simulation of incompressible was made with Spalart-Allmaras model in order to compare the turbulence model with the SST k-ω model.

6. **H1FNVSSTDES** - Using SST-DES for incompressible flow the effect of the volume beneath the spoiler was examined by removing the spoiler and sealing the gap.

3.4 Description of the truck

The truck used in the simulations was the truck model referred to as *H1*. There are two other heights of the same truck referred to as H2 and H3 which in ascending order are higher than H1. Model H1 is displayed in Figures 3.3 and 3.4 viewing the front and left side of the truck.

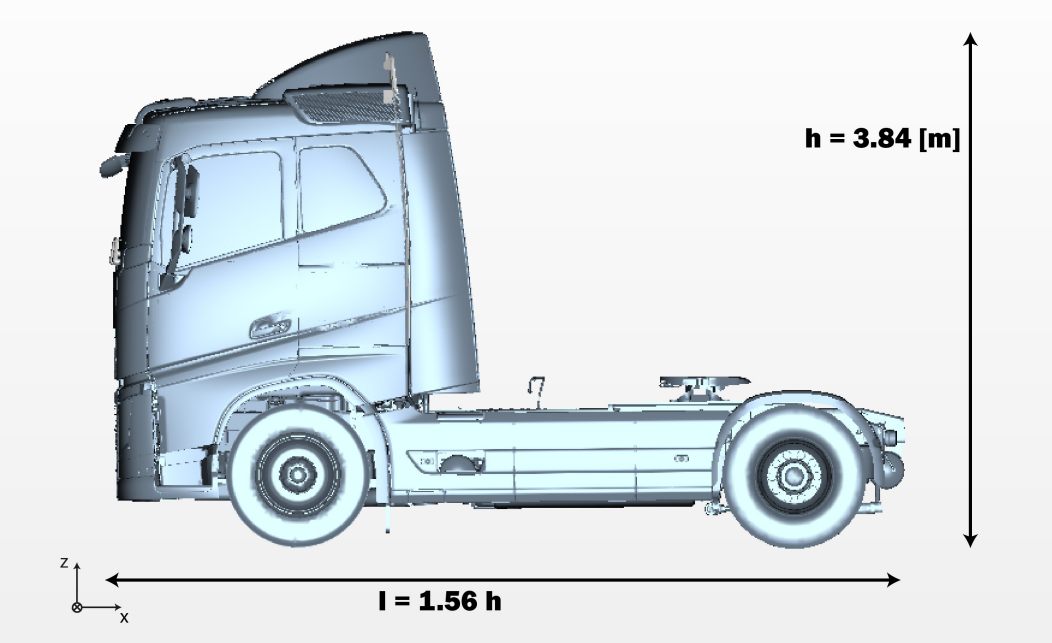

Figure 3.3: Scaled truck dimension length (l) in the x-z plane in terms of the height (h).

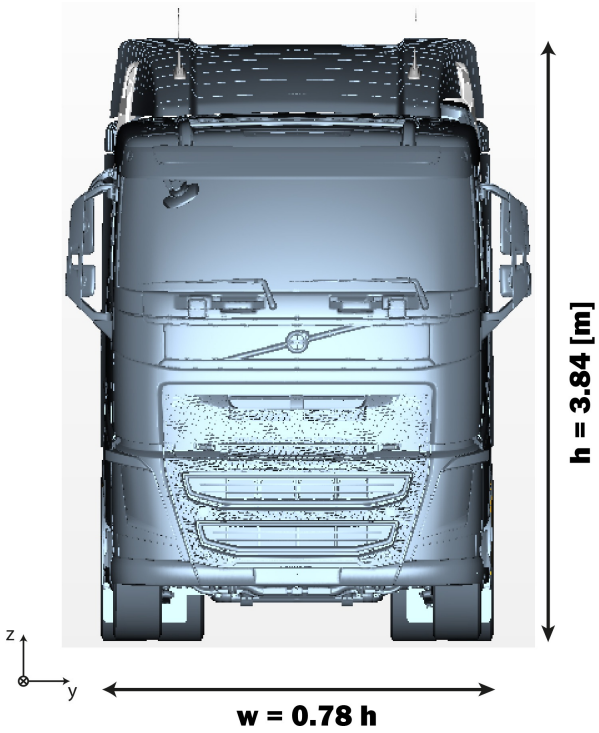

Figure 3.4: Scaled truck dimension width (w) in the y-z plane in terms of the height (h). Note the mirror in front of the passenger side of the cabin.

In Figure 3.5 some parts of the geometry that are repeatedly referred to in this thesis are viewed and they will be briefly explained. The *sunvisor* is the screen that dampens the incoming sunlight to the driver. The *roofbar* is the bar attached on the fronter side of the roof onto which accessories such as horns and warning lights can be mounted. The *hatch*, i.e. the sunroof, could be opened in order to, for instance, let air inside of the truck, to facilitate maintenance on the roof or to use as an escape route after an accident. The *cavities*, front and rear, are the small spaces between the hatch and the roof. Finally, the *spoiler* is the shield at the rear of the roof that leads the air smoothly upon the cargo in order to mitigate the drag effects of the cargo.

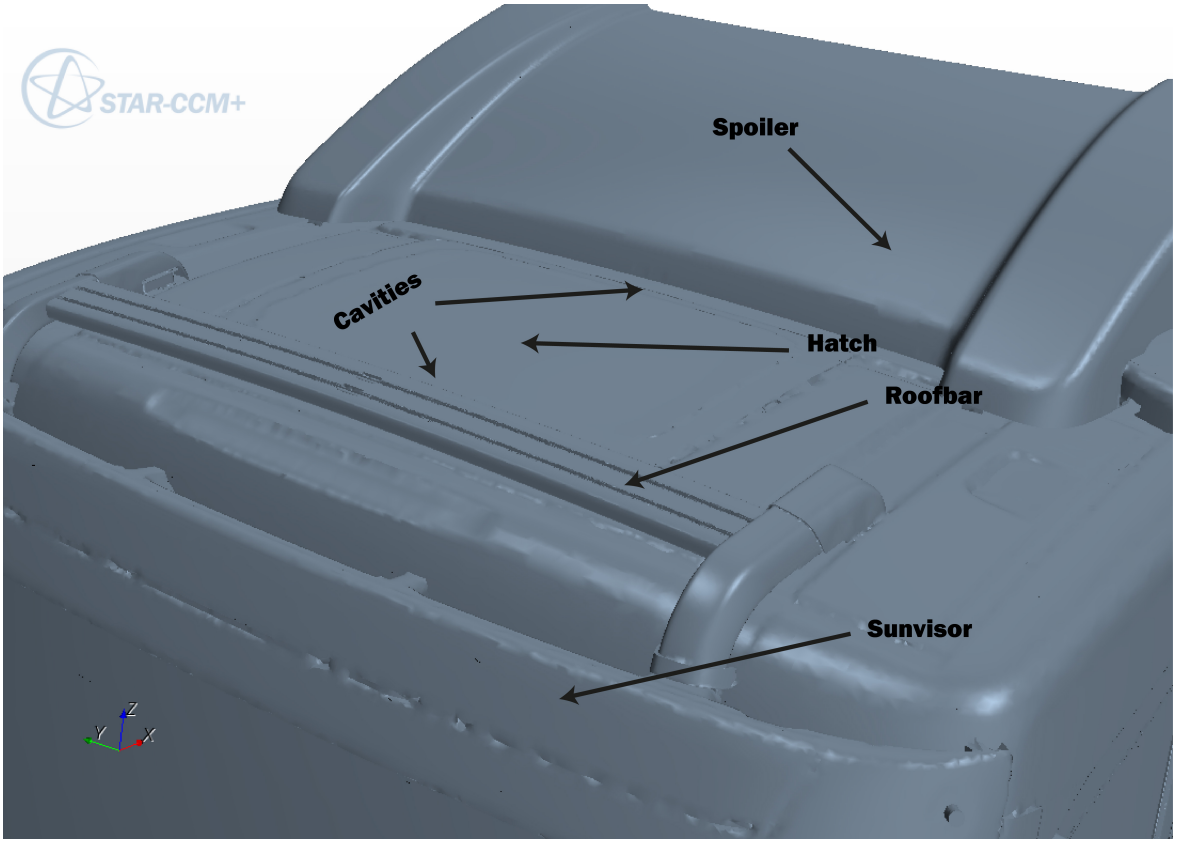

Figure 3.5: The described parts are visualized. Note that the closest cavity cannot be seen as the roofbar is in the way from this view. The hatch is not clearly observable, however, the hatch-arrow points at the center of the hatch while the rear cavity-arrow points at the cavity surrounding the hatch.

3.4.1 Domains

Two different computational domains were used. One wind-tunnel domain and one focus domain. Both are described in this section.

3.4.1.1 Wind-tunnel domain

The dimensions of the wind-tunnel domain can be seen in Figure 3.6 and 3.7. Based on the height of the truck the Reynolds number of the simulation is $Re_h \approx 6.32 \cdot 10^6$.

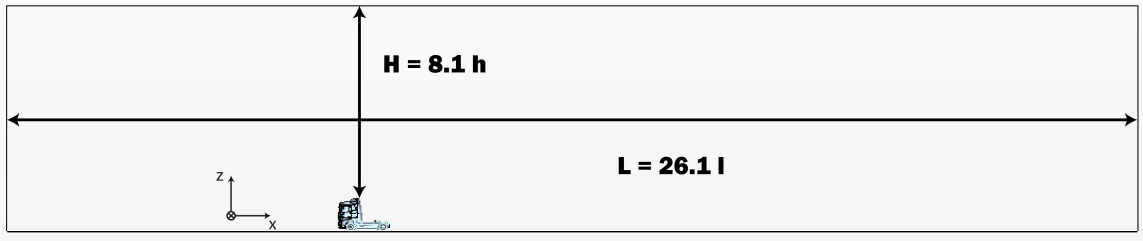

Figure 3.6: The scaled sizes of the wind-tunnel domain with respect to the height (h) and length (l) of the truck in the x-z plane.

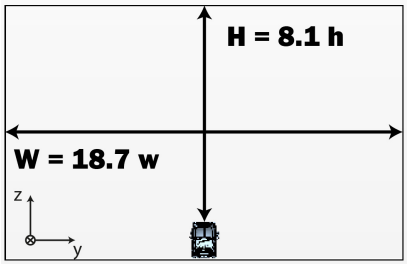

Figure 3.7: The scaled sizes of the wind-tunnel domain with respect to the height (h) and width (w) of the truck in the y-z plane.

3.4.1.2 Focus domain

The focus domain has a high aspect ratio of length and height with respect to the thickness of the domain. This is illustrated in Figure 3.8 where it can be seen that the length and the height is 19.3 and 37 times larger than the thickness respectively. Based on the height of the leading edge of the roofbar, $R = 0.025$ m, the Reynolds number is $Re_R \approx 41{,}100$.

Some simplifications on the geometry have been done. Small cavities prior to the roofbar have been sealed in order to put focus on the roofbars interaction with the front cavity and the hatch. Also, the volume of the cavity is in fact larger but has been cut off in the x-direction in order to save cells since the smallest cells in the domain exists here.

On the top of the roofbar two troughs have been covered. These troughs serve as mountings for the roofbar attachments and the noise they emit could be neglected according to Hedlund [14] since they compared to the noise created between the roofbar and the roof as well as the hatch have a minor importance on the noise perceived from inside the truck. In Figure 3.5 the troughs are left and are the two darker lines on the top of the roofbar.

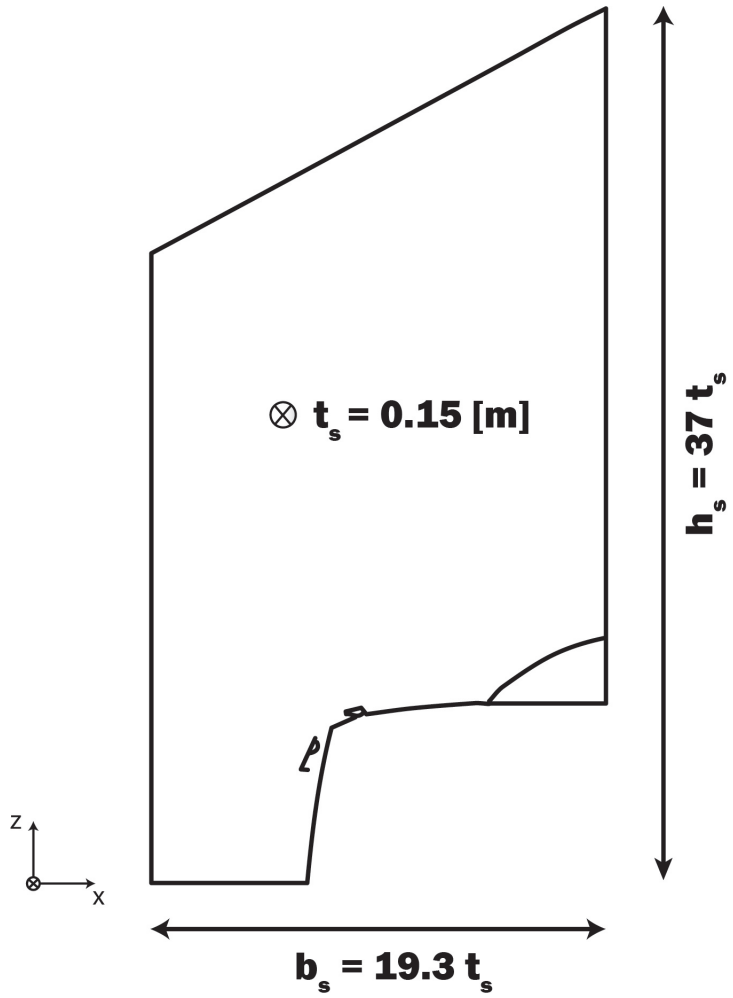

Figure 3.8: The smaller domain in the x-z plane with length (b_s) and height (h_s) expressed in terms of the domain thickness (t_s). Note $\otimes$ inside the domain which is the distance line going in to the plane and thereby representing the thickness of the domain.

There is one major difference between the domain in this thesis and the domain made in [32]. The volume beneath the spoiler is included in this thesis and is connected to the upstream flow by a small gap. Also, the largest cells in this domain were set to be anisotropic in order to let the flow to have a chance to develop in the y-direction. The anisotropic cells were set to be half of the size in the z- and x-direction, i.e. $\Delta y_{max} = 0.5max(\Delta x, \Delta z)$.

3.4.2 Measuring probes

Measuring probes were located in areas where interesting phenomena were to be expected. These probes monitor a specified quantity for a determined time-period during the simulation. In this thesis pressure fluctuations were monitored since they according

to Eq. (2.23) are of interest for the FFT-analysis.
Figure 3.9 and Figure 3.10 show the placement of the probes where the pressure fluctuations were measured.

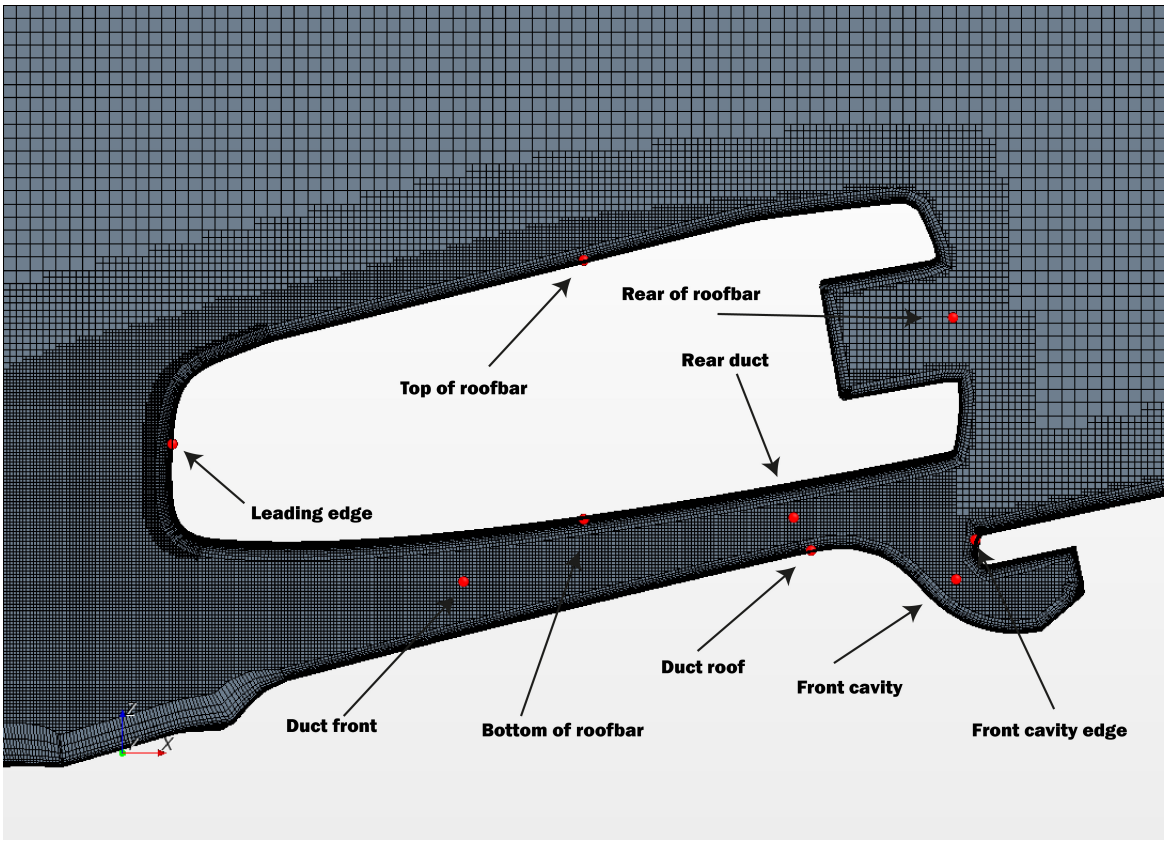

Figure 3.9: The probes surrounding the roofbar in mesh M2. Note the refinements due to the use of LES.

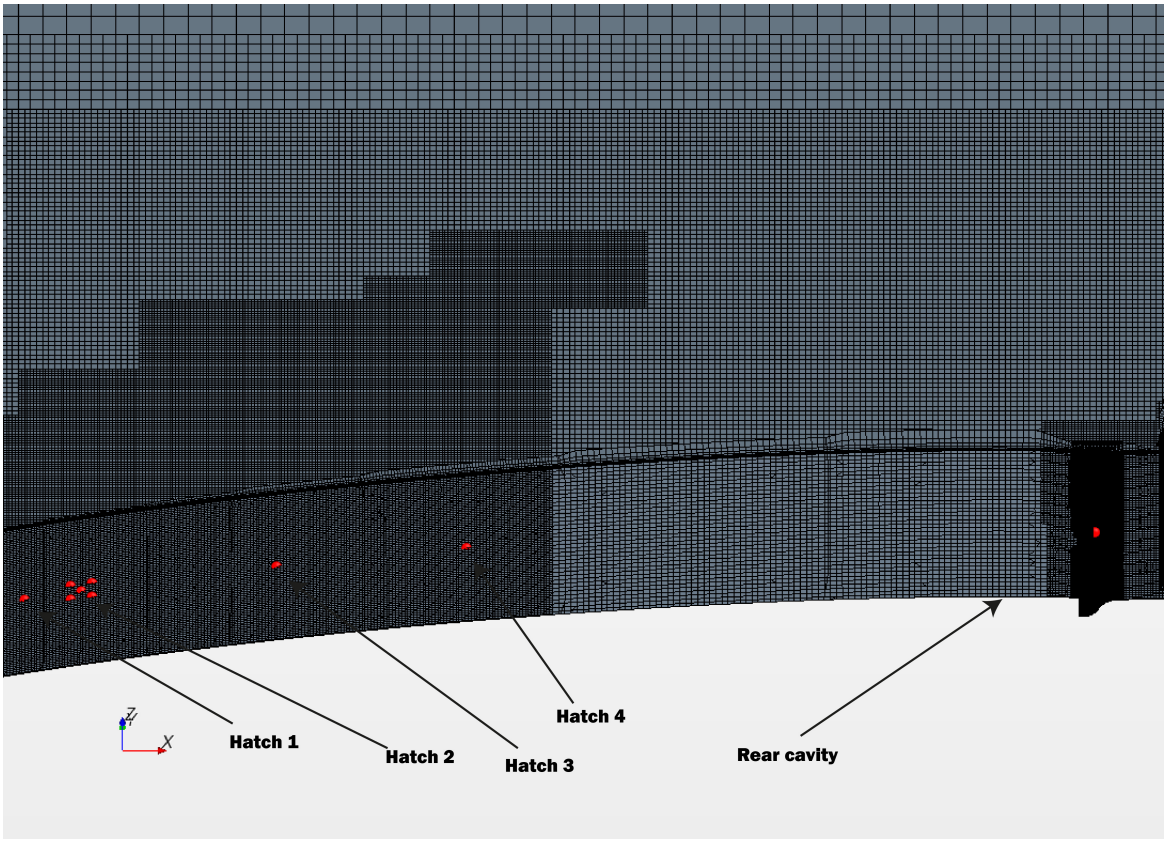

Figure 3.10: The probes downstream of the roofbar. Note that "Hatch 2" has four surrounding probes. These probes are used for making an attempt to find an average of the SPL-values.

The "Hatch 2"-probe is surrounded by four probes. It was observed in [32] that there were large spatial variations in pressure. Therefore, this is to be examined by taking the root-mean-square value of the the center-probe itself and the surrounding probes

$$\overline{p}^2 = \frac{\sum_{i=1}^{N} p_i^2}{N} \tag{3.1}$$

where N is the number of probes, here $N = 5$. In this way local variations are presumed to be accounted for.

Table 3.2: Mesh details for each case.

Mesh case	**Max cell size [m]**	**Min cell size [m]**	**Number of cells**
H1WSST (M1)	2.3	0.002	$45.7 \cdot 10^6$
H1FVLES (M2)	0.016	$0.25 \cdot 10^{-3}$	$17.1 \cdot 10^6$
H1FVCSSTDES (M3)	0.016	$0.5 \cdot 10^{-3}$	$4.92 \cdot 10^6$
H1FVSSTDES (M3)	0.016	$0.5 \cdot 10^{-3}$	$4.92 \cdot 10^6$
H1FVSADES (M3)	0.016	$0.5 \cdot 10^{-3}$	$4.92 \cdot 10^6$
H1FNVSSTDES (M4)	0.016	$0.5 \cdot 10^{-3}$	$4.86 \cdot 10^6$

3.5 Meshes

The mesh generations were made only in StarCCM+ which contains an automatic mesh generator. In Table 3.2 the maximum and minimum cell sizes as well as the number of cells for each mesh are displayed. Note that M2 contains more than three times as much cells as M3 and M4.

In total four different meshes were generated. Table 3.2 shows which case that belongs to which mesh.

Figure 3.11 shows how the focus domain is applied onto the truck. The mid-plane of the domain is the x-z plane located at $y = 0$.

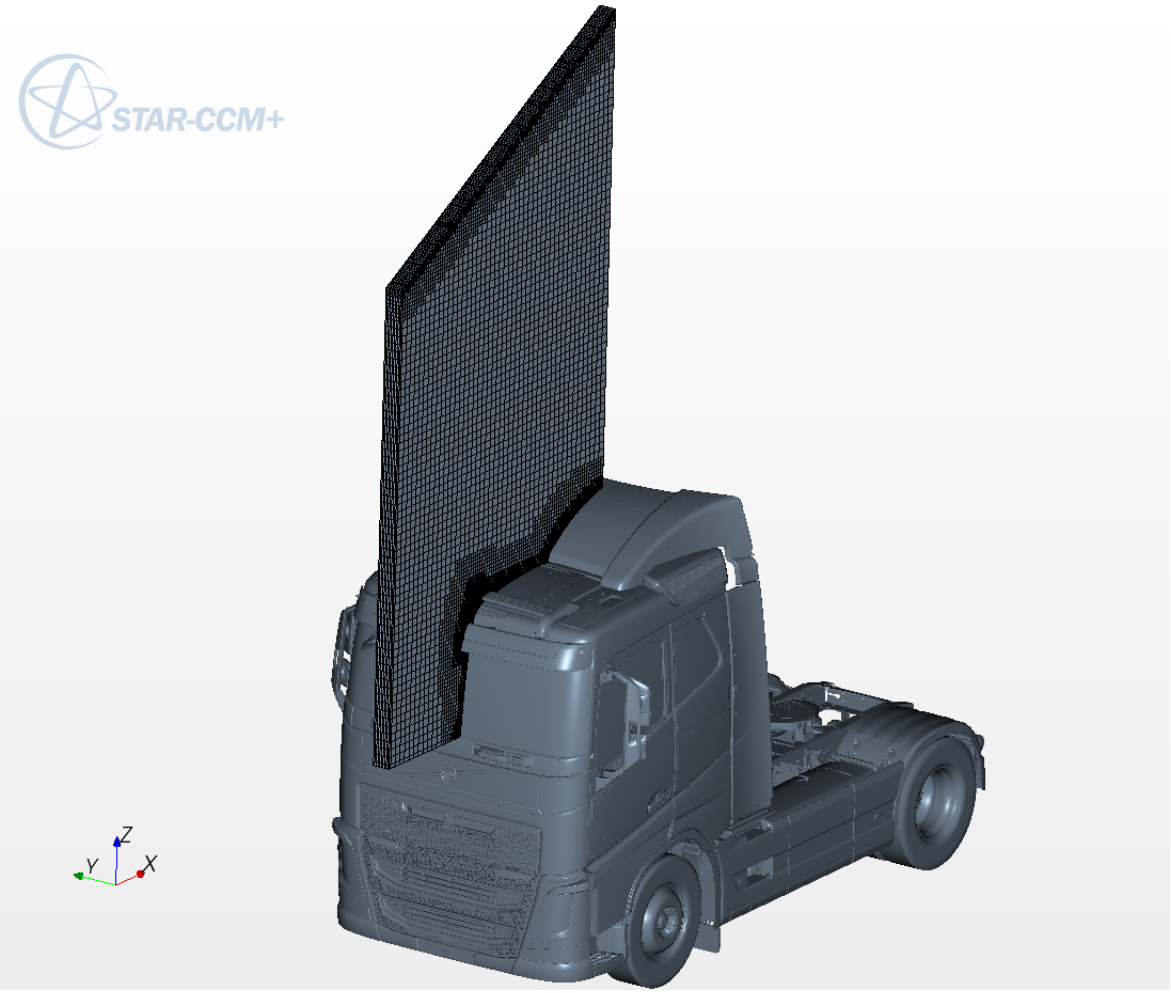

Figure 3.11: The focus domain is applied onto the truck.

3.5.1 Mesh for windtunnel simulation

The mesh for the windtunnel is a coarse mesh with rather large cells in the focus region. These cells could have been refined but were kept large in order to keep the total amount of cells lower.

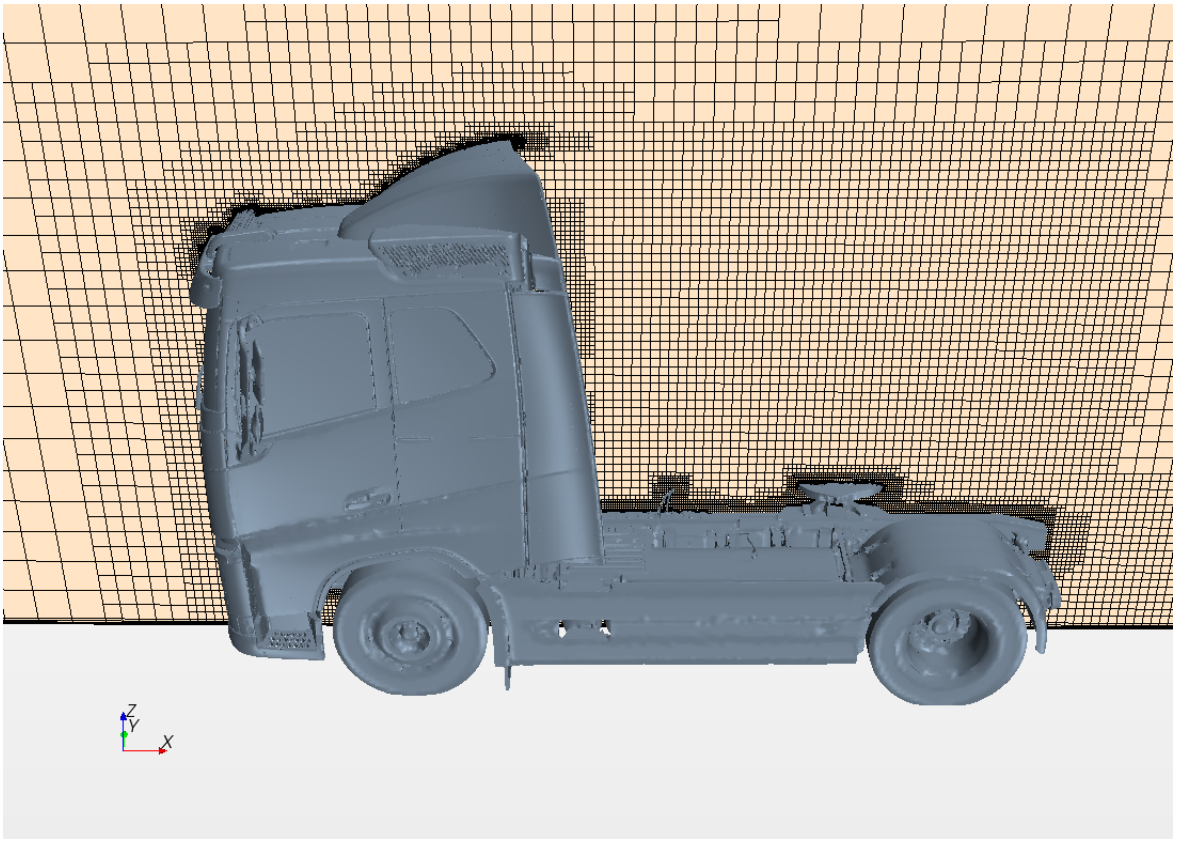

Figure 3.12: The mid-plane of the windtunnel mesh viewed slightly from above in order to capture the cells close to the surface.

3.5.2 Mesh for LES

Mesh M2 differs from mesh M3 mainly by the refinement of the boundary-layers. At the roofbar and the hatch the surface cell size is 0.5 mm. At the leading edge of the roofbar the surface size is 0.25 mm in order to fulfill the longitudinal and span-wise resolution requirements. The number of boundary-layer cells in the wall-normal direction were 18 for those areas. The wall-normal size of the closest cells to the wall were adjusted to fulfill the y^+-requirement $y^+ \leq 1$. For the entire roofbar, where the velocities are high all over except at the trailing edge, the distance is 0.0065 mm. At the trailing edge the wall-normal distance is 0.015 mm due to lower velocities. Under the roofbar, in the duct, the distance is 0.009 mm. At the hatch the distance is 0.018 mm. Refinement-boxes and the so called *trimmer refinement* function were used to create refined areas. The refinement boxes were used to refine the volume in the cavities with 0.5 mm cells, the volume of the duct with 0.5 mm cells and the volume around the roofbar as well as in the wake with 2 mm cells. Boxes were also used to create interfaces between finer and coarser cells. The trimmer refinement function refines with a desired cell size for a specified distance and direction. The function was used at the boundary of the roofbar

as well as at the hatch from the front cavity and beyond ”Hatch 4”.

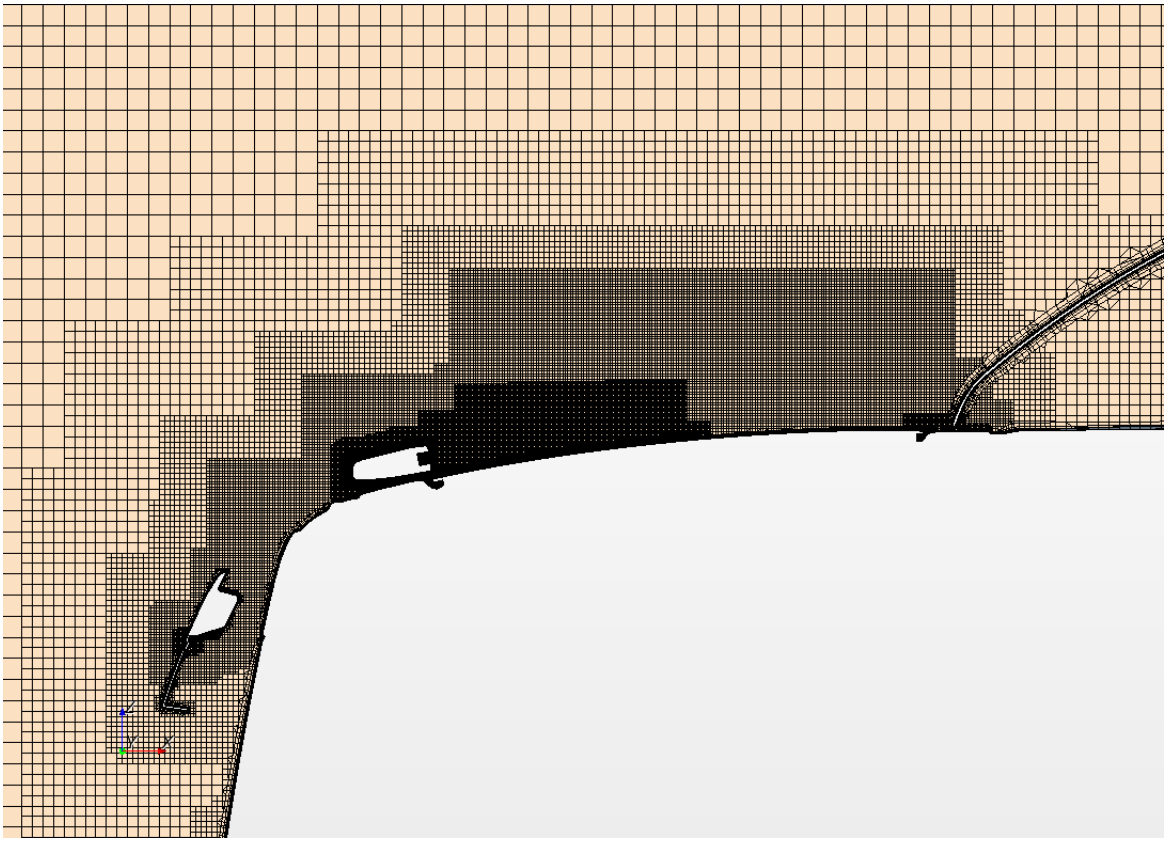

Figure 3.13: The mid-plane for mesh M2. By looking closely on the wall behind the roofbar it could be seen that the boundary layer is highly resolved.

3.5.3 Mesh for DES

For DES the mesh requirements are less strict. All over the roofbar and the front half of the hatch the surface cell size is 2 mm. The number of boundary-layer cells are 14 at the roofbar and 12-13 at the hatch. As well as for LES the wall-normal distances to the closest cell were adjusted by fulfilling $y^+ \leq 1$. This led to 0.01-0.02 mm at the roofbar with the thinnest cells at the leading edge. The same distance in the duct is 0.009 mm and the distance for the hatch is 0.013-0.021 mm. Refinement-boxes were used in the same areas as in mesh M2 though using 1 mm grids in the duct. Trimmer refinement was not used for mesh M3 and mesh M4.

DES is very sensitive and highly dependent on the mesh. Therefore, guidelines for successful DES-meshing produced by Spalart [29] were used for guidance. Basically, the guidelines divides the domain into several types of regions depending on the features of the flow and the mesh is constructed thereafter.

The smallest cell size for M3 and M4 is found in the cavities where the size is 0.5

mm. In comparison with the mesh for LES the isotropic cell size in the duct is 1 mm.

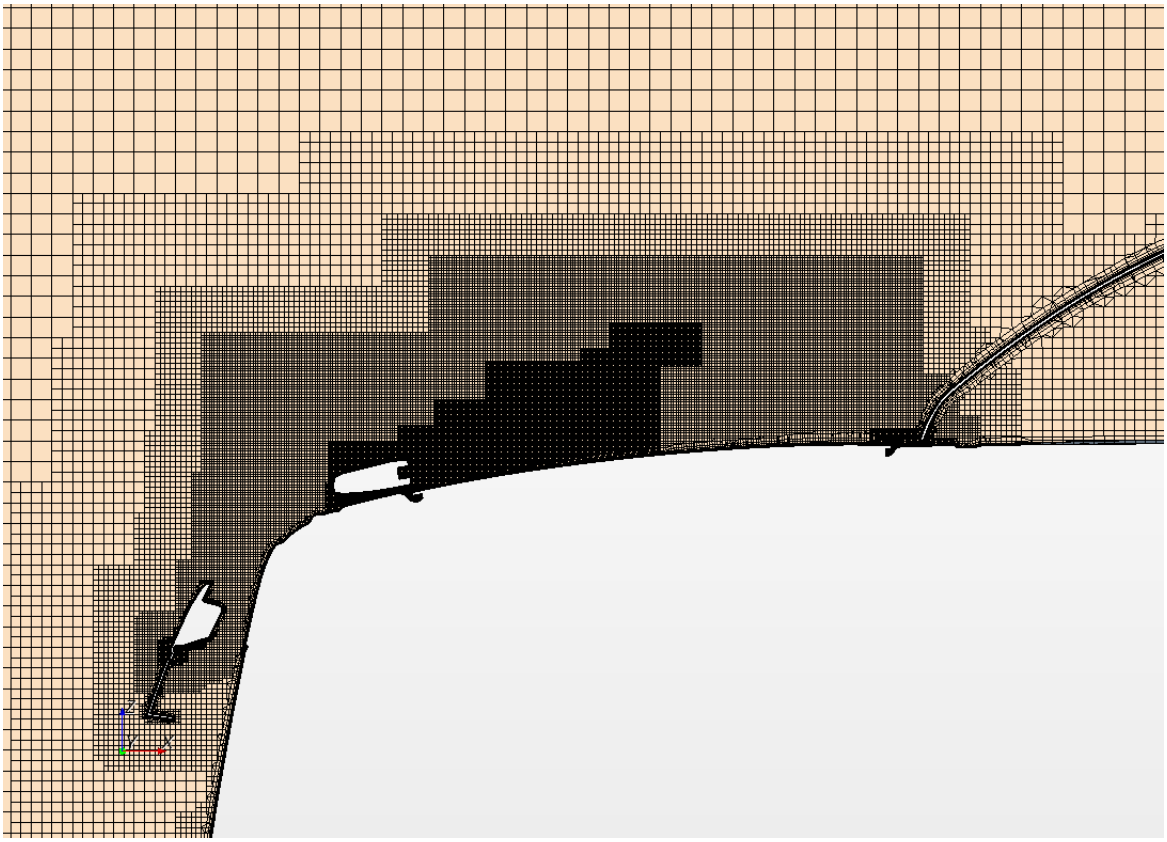

Figure 3.14: The mid-plane (y=0) for M3. For M4 the volume under the spoiler is simply to the right removed.

Comparing Figure 3.14 with Figure 3.13 shows that the refined region is smaller for LES than for DES. This is due to keep the number of cells down for the LES-mesh.

3.5.4 Meshing for aeroacoustics

Creating a mesh for aeroacoustics requires extremely fine grids. There are different approaches for determining the grid size needed to resolve sufficiently high frequencies. In this thesis Curle's method and Proudman's method were used during steady-state simulations prior to the transient simulations. Curle's method was used for estimating surface sources while Proudman's was used to find volume sources. If it is not the case of resonance phenomena the volume sources have quadrupole behavior, however, those acoustic sources are still good indicators of where high turbulent kinetic energy is located which might be essential to resolve since it might affect the acoustic noises on nearby walls. The turbulent kinetic energy is directly related to the *mesh cut-off frequency* which indicates how high frequencies the mesh can resolve. The cut-off frequency is

dependent on the resolved turbulent kinetic energy as:

$$f_{max} = \frac{\sqrt{\frac{2k}{3}}}{2\Delta} \tag{3.2}$$

When the desired cell size is determined by Eq. 3.2 it has to be correlated with the stability criterion $CFL = 1$ in Eq. 2.19 so that a proper time-step can be found.

Another thing to bear in mind is that since M2-M4 are trimmed meshes issues can occur at the interface at which the grid coarsenes. The coarsening can make the structures of the flow to attenuate the pressure effects of the acoustics since the coarsening is practically performed by that two cells become one twice as large cell over the interface. It is therefore recommended by CD-Adapco to use 20 cells per acoustic wavelength and higher if the local convective discretization scheme goes down to first order [6].

3.6 Simulation setup

The settings for the simulations are described in this section.

3.6.1 Steady-state wind-tunnel simulation

The wind-tunnel simulation was a steady-state simulation using SST as turbulence model. The resulting steady-state values were applied to the boundaries of the focus domain which during the simulation was set as wall boundaries. However, by using a so called *in-place interface* that is available in StarCCM+ the air flows through the boundaries as if they were permeable. By saving variable data at the boundaries the boundary conditions for the focus domain were generated.

SST was used as turbulence model since it is an accurate general model that calculates two turbulent quantities, turbulent kinetic energy k and specific dissipation rate ω. Only one RANS-model was used since every case will have the exact same boundary conditions in order for them to be comparable.

3.6.1.1 Boundary conditions

The boundary conditions of the wind-tunnel are summarized in Table 3.5. The velocity inlet was set to 25 m/s and the velocity at the wall is zero while the other boundaries are dependent on the features of the inlet and bottom.

Table 3.3: Boundary conditions for the wind-tunnel domain simulation. Note that these boundaries are not the ones represented in Figure 3.15.

Boundary	Boundary condition
Inlet	Velocity inlet
Outlet	Pressure outlet
Left boundary	Symmetry
Right boundary	Symmetry
Bottom boundary	Wall
Top boundary	Symmetry

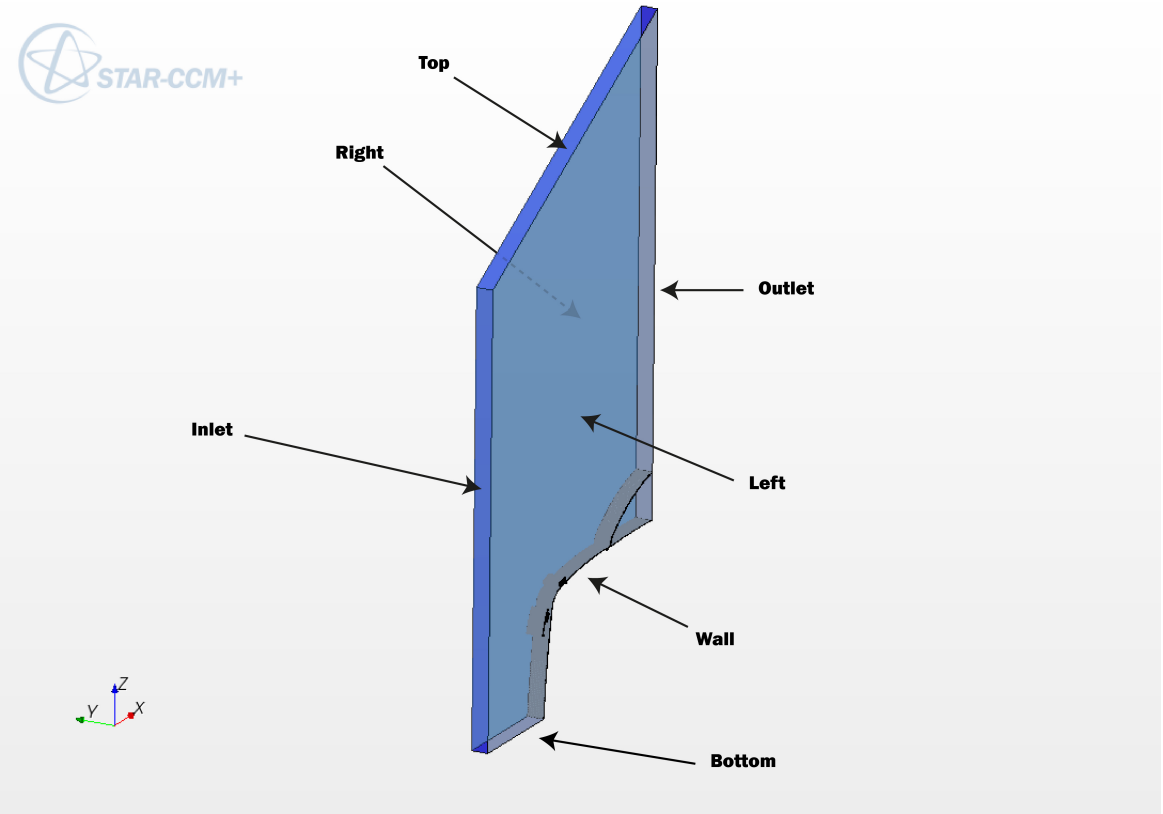

Figure 3.15: The boundaries of the focus domain.

3.6.2 Transient simulations

Tell [32] determined a physical time of 0.5 s to be sufficient for a valid FFT-analysis. The same physical time were used in this thesis in order for the results from the two

theses to be comparable. The transient simulations had a time-step $\Delta t = 1.5 \cdot 10^{-5}$ s, as in [32], converged by performing 10 inner iterations. Constant temperature $T = 300°K$ was used. Segregated solution of pressure and velocities was assumed for all the transient simulations as well as an under-relaxation factor (URF) of 0.8 for the velocity while the pressure URF was set to 0.2. The SIMPLE-algorithm helped with correcting the pressures in the solution. A second order Euler scheme was used for temporal discretization as the Euler scheme is the only type available.

3.6.2.1 LES-settings

The SGS-model used in the LES-simulation was the WALE-model in which the default WALE-coefficients were used:

$$C_w = 0.544$$
$$C_t = 3.5$$
$$\kappa = 0.41$$

BCD was used as convective scheme with an upwind blending factor of 0.15. The blending factor acts to blend CD and UDS by adding 15 % of the upwind scheme.

The *all* y^+ *wall-treatment* was used which is a general wall-treatment. If y^+ is high wall functions are used and if y^+ is satisfactorily low the boundary-layer is solved without wall-functions.

3.6.2.2 DES-settings

For the DES-simulation Hybrid-BCD was used as the convective scheme and as for LES the upwind blending factor was set to 0.15. IDDES was activated in order to avoid MSD. The following IDDES coefficients were used:

$$C_t = 1.87$$
$$C_l = 5$$

The SST-DES-model used a k-ω turbulence URF of 0.8 while the SA-DES-model used a Spalart-Allmaras turbulence URF of 0.7. The turbulent viscosities for both models were upgraded with an URF of 1.

It is unclear which SGS-model that is used for DES in StarCCM+. According to [16] the SGS-model used is the ordinary Smagorinsky model with some further modifications that were unclear at the time of conversation.

The *all* y^+ *wall-treatment* was used also for the DES-cases.

3.6.2.3 Boundary conditions for compressible flow

Unique for the compressible transient simulation in StarCCM+ was the use of the so called *freestream* boundary condition which is said to be non-reflective to boundary-normal disturbances. The boundary condition was selectable only when assuming ideal

Table 3.4: Boundary conditions for the compressible transient simulation.

Boundary	Boundary condition
Inlet	Freestream
Outlet	Pressure outlet
Left boundary	Freestream
Right boundary	Freestream
Bottom boundary	Freestream
Top boundary	Freestream

gas. According to [6] it is based on extrapolated Riemann-invariants assuming that the vorticity is zero and that the flow is a quasi-1D-flow normal to the boundary. The boundaries are therefore advised to be set at far-field distances in order to escape turbulent structures so that the vorticity assumption still is valid. If there exist turbulent structures on the boundary it may give rise to unphysical pressure waves propagating in the domain [6]. This may affect not only the acoustic field but also the flow field if the resulting pressure waves are severe. Also, if the boundary is not perpendicular to the compressible waves this may also lead to errors.

The pressure outlet was expected to be reflective and the freestream boundary is a non-reflective boundaries [6]. However, Tell [32] showed that the outcome at the hatch did not show any significant difference between choosing freestream or pressure outlet at the outlet boundary when examining the SPL-values. The pressure outlet was chosen since the freestream boundary condition at first was thought to be too constraining.

The quantities specified at the freestream boundaries were velocity vector u_i, turbulent kinetic energy k, specific dissipation rate ω, pressure p and Mach number M.

3.6.2.4 Boundary conditions for incompressible flow

Velocity inlet was chosen as boundary conditions for the incompressible cases in order to apply the steady-state boundary conditions since the freestream boundary condition does not support incompressible fluids.

For the SST-DES simulation the same quantities as for the compressible case except for the Mach number was specified at the velocity inlet boundaries. The pressure outlet boundary was specified with turbulent kinetic energy, specific dissipation rate and pressure.

The SA-DES simulation was provided with values of the velocity vector and turbulent viscosity-ratio at the velocity inlet boundaries. At the pressure outlet turbulent viscosity-ratio and pressure were specified.

The LES simulation was specified with velocity at the inlet and pressure at the outlet.

Table 3.5: Boundary conditions for the incompressible transient simulation.

Boundary	**Boundary condition**
Inlet	Velocity inlet
Outlet	Pressure outlet
Left boundary	Velocity inlet
Right boundary	Velocity inlet
Bottom boundary	Velocity inlet
Top boundary	Velocity inlet

3.6.2.5 Compressible or incompressible flow?

For low Mach numbers unsteady hydrodynamic flow is most of the times the dominating noise source. Thus, an incompressible approach could be undertaken which is desirable since the computational costs can be substantially reduced compared to a compressible approach. However, there are some implications for such an approach that one has to be aware of.

Firstly, since propagation of sound is caused by compressibility the propagation is lost which implies that reflections on solid boundaries also will be lost. This problem can be remedied by using a so called *hard wall Green's function* so that all reflections at the wall is included in this function. The method has been used for instance by Wang and Moin on the noise-generation by an airfoil trailing-edge [34]. According to Kierkegaard [17] the hard-wall Green's function is what is effectively used in the FW-H-equation when using an impermeable surface. However, this method is believed to add to the computational costs so that it even exceeds the computational costs of the compressible approach since an additional equation has to be solved.

Secondly, Ask [2] concluded the following for an incompressible approach in his PhD-thesis:

- The acoustic sources and their magnitude were satisfactorily predicted, however, the directivity of the sound was somewhat mispredicted.
- The pressure term of the incompressible governing equations is elliptic which means that any distortion may be instantly present in the entire domain.
- If there is a fast variation in the geometry the incompressible flow cannot compensate by compressing the fluid which may affect the acoustic results.
- Incompressible flows can only change pressure and velocity when the flow for instance flows into singularities of a mesh. This can therefore cause oscillations.

3.6.2.6 FFT-analysis

The FFT-analysis is based on the monitored pressure fluctuations mentioned in Section 3.4.2. Since the solution was quite unstable in the beginning of the simulation a buffer time-period of 0.25 s was used in order to make the simulation fully developed so that the pressure fluctuations stabilizes. From 0.25 s until the end at 0.5 s the FFT-analysis was activated. A-weighted SPL-values were calculated using a Hanning window. Temporal spectral averaging was used in the sense that three analysis blocks were used in order to smooth the FFT-analysis. Here, an overblock factor of 0.5 was used which says that the second half of the first analysis block overlaps the first half of the second block and so on.

StarCCM+ provides the possibility to save pressure fluctuations in the entire volume as well as on the boundaries. Thus, it is possible to see where the largest acoustic sources exist either for a certain frequency or for a range of frequencies.

During the analysis of the entire surfaces a distinct frequency will not be considered but an interval of frequencies called *1/3 octave band* in which an octave is the range between a certain frequency and the double of the same frequency. The value of 1/3 represents the lower and upper limits surrounding the *center frequency*. When using 1/3 octave band the signals are averaged over the interval of frequencies [4].

The chosen center frequencies as well as their lower and upper band limits are presented in Table 3.6:

Table 3.6: Center frequencies with the correspondent lower and upper band limits.

Center frequency (Hz)	**Lower limit (Hz)**	**Upper limit (Hz)**
125	112	141
250	224	282
500	447	562
1,000	891	1122

In contrast to the FFT of the pressure fluctuations at the surfaces the FFT-analysis regarding the probes is made for the center frequencies in Table 3.6 without band limits.

4 Results

First the flow-field results are presented by viewing contour-plots of the velocity field. These results are essential in order to explain phenomena and the complexity of the flow. Secondly, the aeroacoustic results are presented. Two types of aeroacoustic results are mainly shown: FFT of the monitored probes and FFT at the walls mainly focusing on the top side of the roofbar, duct roof and the hatch. The FFT based on the pressure fluctuations on the surface reveals where on the surface noise sources exist. In Figure 4.16 the geometry of the top side of the roofbar and the hatch is viewed on which the surface FFT results will be plotted. Figure 4.17 is the same type of plot only putting more focus beneath the roofbar as well as giving a close-up of the front cavity.

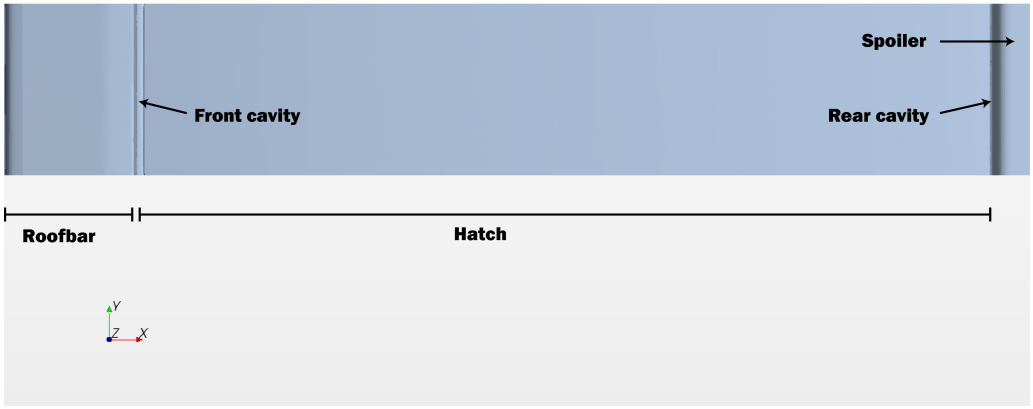

Figure 4.16: The surface at which the surface FFT results are presented.

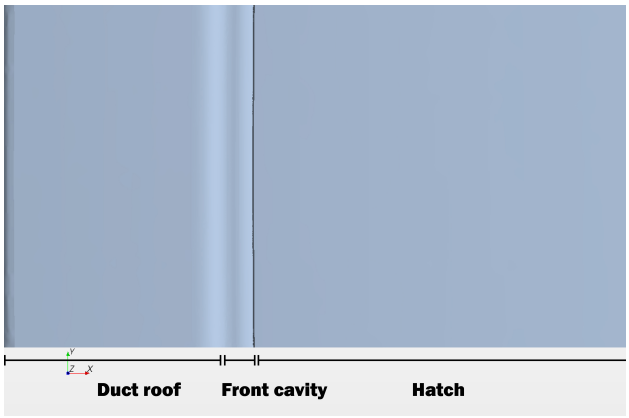

Figure 4.17: The surface at which the surface FFT results at the duct are presented. The roofbar has simply been removed for display purposes.

The frequency of the monitor plots ranges from 20 Hz to 6,000 Hz. The motivation why the lower limit was chosen is that, as mentioned, 20 Hz is the lowest frequency a

human being can perceive while the upper limit was arbitrarily chosen to a rather audible frequency since interesting numerical properties could occur for higher frequencies.

4.1 Flow-field results

In Figure 4.18 the instantaneous velocity-fields of incompressible LES, incompressible SST-DES and compressible SST-DES are shown. This figure together with animations reveal that the sunvisor creates a vortex shedding which in turn alternately sends small portions of high and low velocities onto the leading edge of the roofbar. The air that flows beneath the roofbar is accelerated before most of the flow escapes over the hatch. A small fraction of the air flows down in the front cavity where the air starts to rotate.

The incompressible DES-simulations were unable to develop scales in the lower wake behind the roofbar and over the hatch which is revealed in Figure 4.18b. By observing also Figures 4.18a and 4.18c showing LES and compressible SST-DES respectively it could be seen that turbulent scales are developed far downstream in the wake.

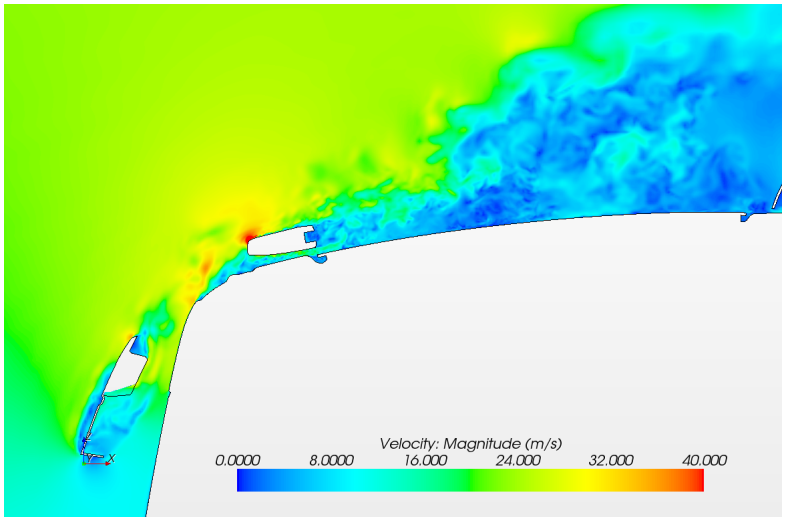

(a) Incompressible LES

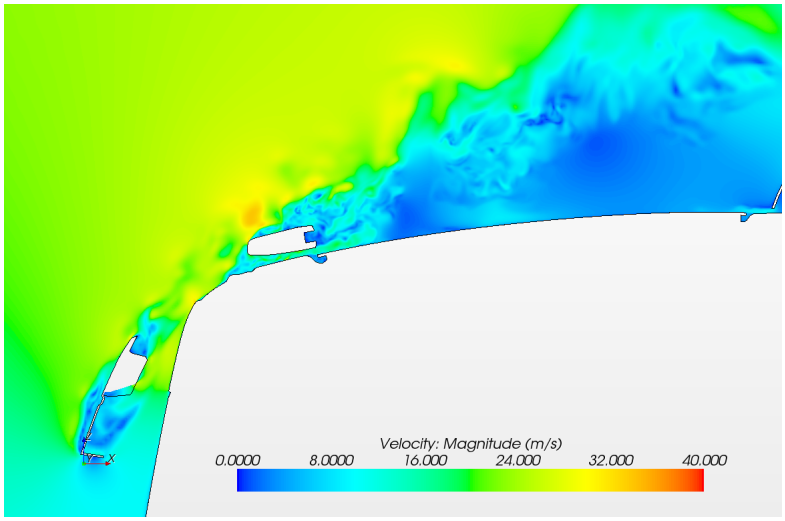

(b) Incompressible SST-DES

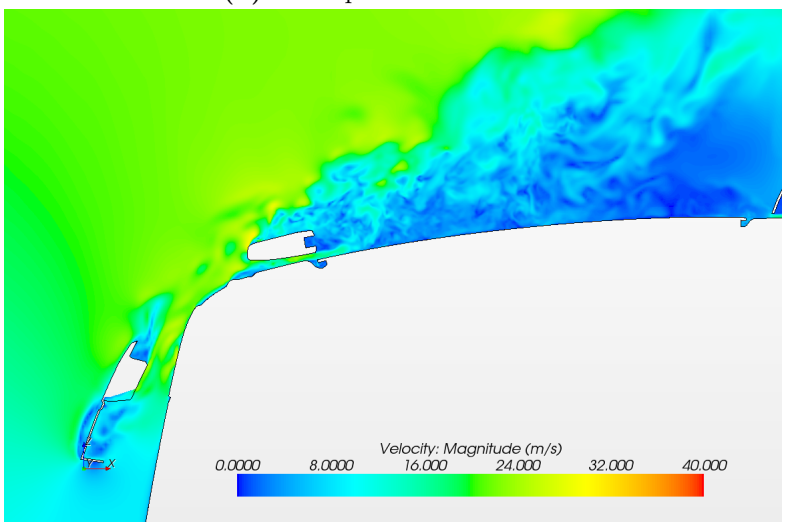

(c) Compressible SST-DES

Figure 4.18: Contour-plots of the instantaneous velocity-fields for incompressible LES and SST-DES as well as compressible SST-DES. SST-DES is representable for all incompressible DES-simulations. Note the vortex shedding at the rear of the sunvisor.

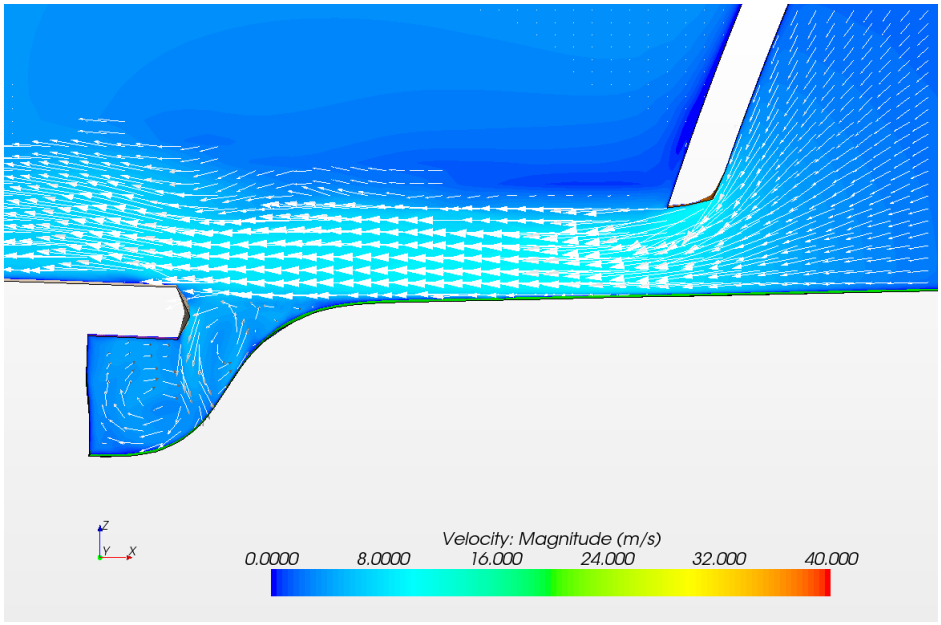

Figure 4.19: The instantaneous velocity field for the spoiler-gap using incompressible SST-DES. Note that the velocity is flowing in negative x-direction.

Looking at Figure 4.19 it can be seen that for incompressible DES the air flows in the negative x-direction, out of the volume beneath the spoiler, with a velocity of approximately 9 m/s. Neither of the two latter phenomena are observed for the LES-simulation nor the compressible SST-DES simulation which could be seen in Figures 4.18a and 4.18c respectively. The turbulent scales for LES and compressible DES are instead developed in the entire turbulent region and the air is flowing in the positive x-direction into the volume beneath the spoiler.

Figures 4.20a - 4.20c show the mean velocities of the incompressible simulations where the volume beneath the spoiler is meshed. SA-DES and SST-DES are identical while LES differs with a distorted separated profile. On average the DES-simulations separate from the roofbar while the LES on average lies attached to it. The time-averaged velocity-fields are included since the separation angle fluctuates, especially for DES.

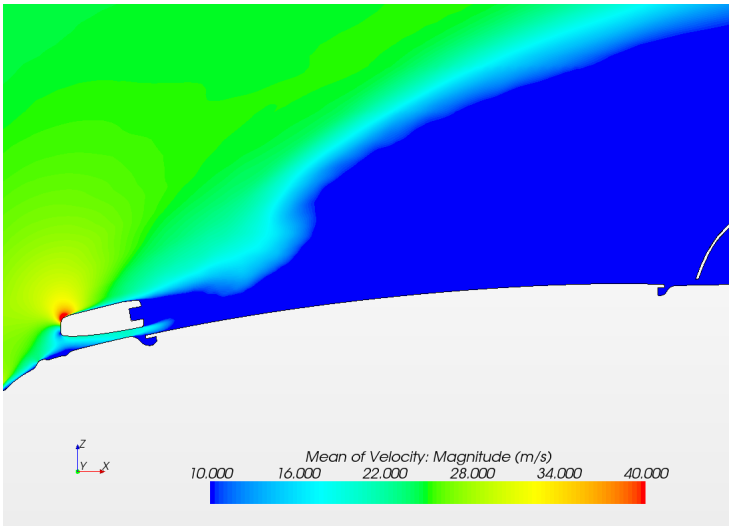

(a) LES

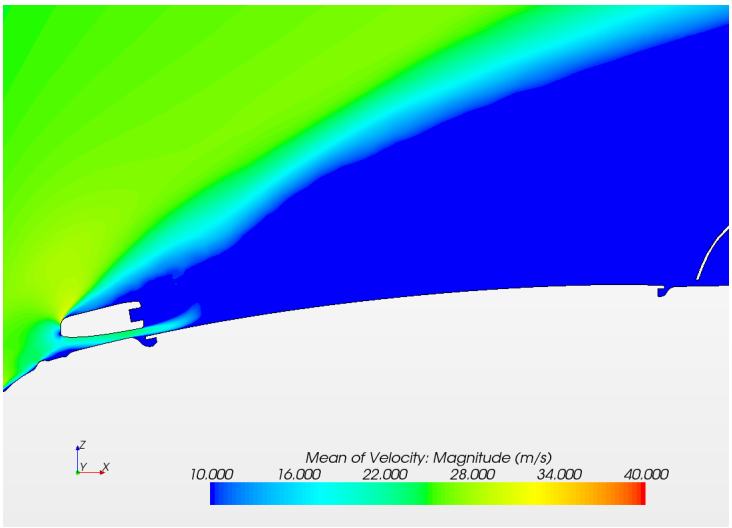

(b) SA-DES

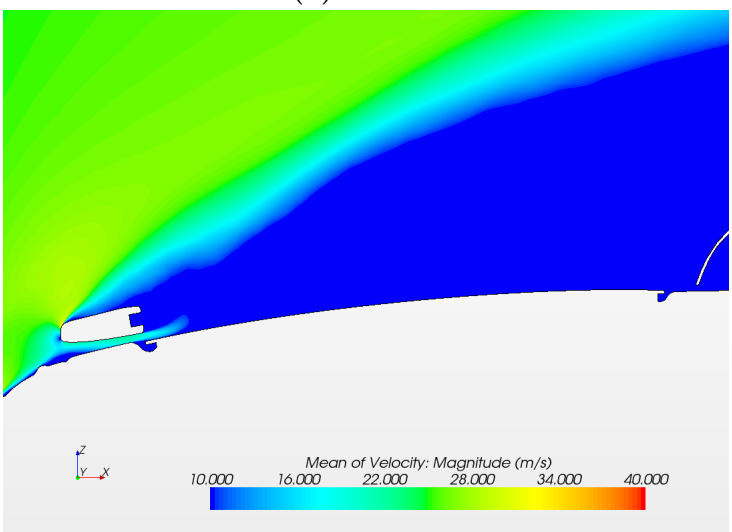

(c) SST-DES

Figure 4.20: Contour-plots of the time-averaged velocity for the incompressible simulations for LES and DES. Note that the scale is changed compared to Figure 4.18 in order to bring a larger contrast from high to relatively low velocities

4.1.1 Dimensionless wall-distance y^+

In Figure 4.21 the instantaneous distribution of the y^+-number is viewed. The other dimensionless numbers for the LES-simulation, s^+ and l^+, were not explicitly available in the software but could be created by assuming that all cells have the same size in the transverse and stream-wise direction. However, the cell sizes are not always the same so the method is not exact and therefore not viewed.

Regarding y^+ most of the areas fulfilled the criteria. Some areas with $y^+ > 1$ are hid behind the roofbar, in small cavities as well as below the spoiler and are not included in Figure 4.21. However, these are not believed to have a large impact on the solution are therefore neglected.

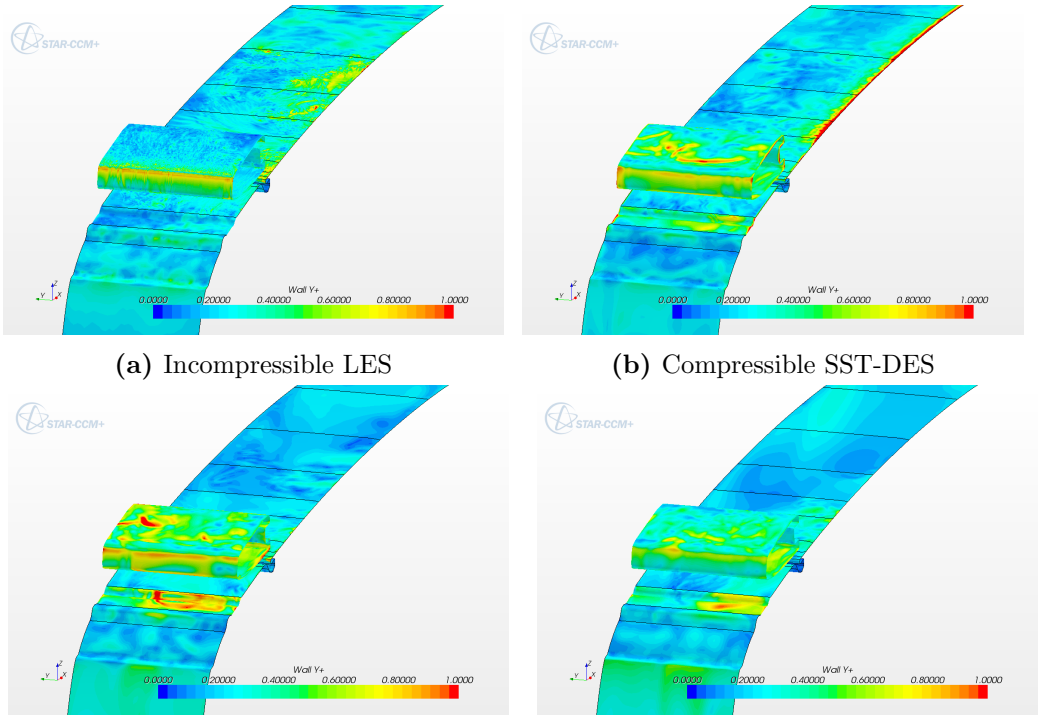

(a) Incompressible LES **(b)** Compressible SST-DES

(c) Incompressible SST-DES **(d)** Incompressible SA-DES

Figure 4.21: Dimensionless wall-distance y^+ for the cases involving mesh M2 and M3.

4.1.2 CFL-numbers

Figure 4.22 shows the CFL-numbers for around the roofbar for the four most central cases. Only close-ups of the roofbar are shown since this is the area where the highest velocities occur as well as where the smallest cells exist. Thus the largest CFL-values will be obtained here. It can be seen that every case has reasonable CFL-values except in the case of LES. Here, values well beyond $CFL = 1$ are found.

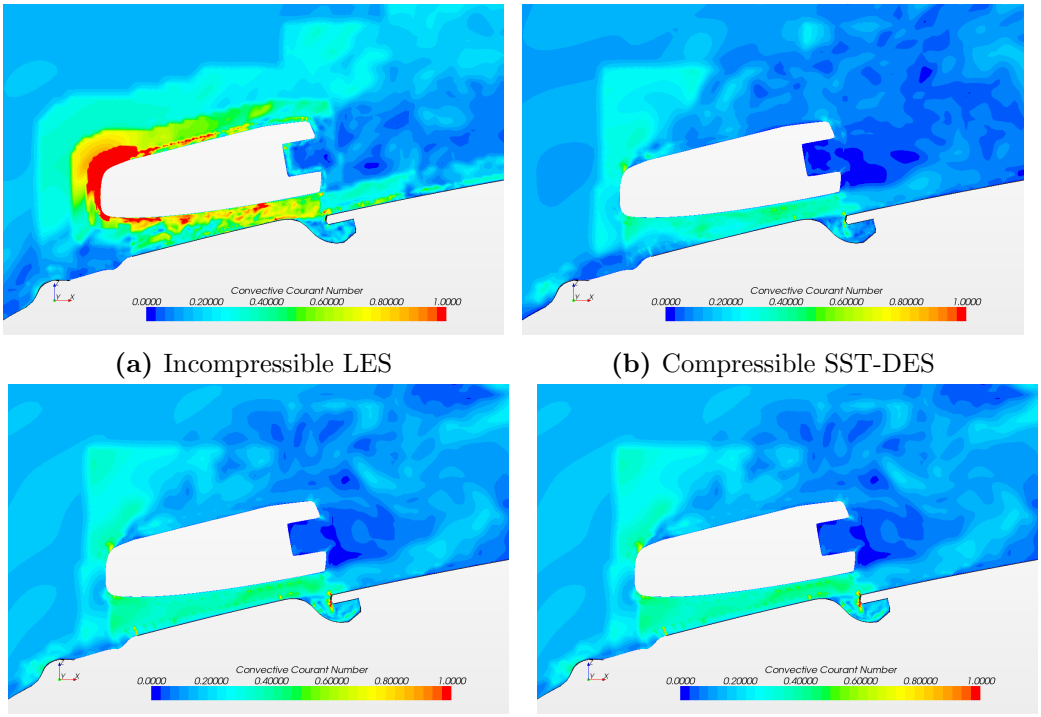

(a) Incompressible LES **(b)** Compressible SST-DES

(c) Incompressible SST-DES **(d)** Incompressible SA-DES

Figure 4.22: Contour-plot for the mid-plane (y=0) showing the CFL-number for the cases involving mesh M2 and M3.

4.2 The aeroacoustic effects of compressibility

Comparisons of the incompressible case and compressible case using SST-DES are presented here.

4.2.1 FFT of monitors

For all figures a tonal peak is significant for the compressible case located at 2,400 Hz. Also, for "Hatch 1", "Hatch 2" and "Leading edge" in Figures 4.23, 4.24 and 4.27 respectively a broad-banded peak is significant. For the incompressible case the peaks above 1,000 Hz vanish entirely.

"Hatch 1" and "Hatch 2" in Figures 4.23 and 4.24 respectively show good overall agreement between the compressible and incompressible case. For "Hatch 2" the curves have an internal distance of 5 dB below 100 Hz. They merge at 100 Hz and separate at about 1,000 Hz.

For "Duct roof" in Figure 4.25 an exceptional broad-banded behavior is shown with almost constant SPL-values from 100 Hz to 1,000 Hz. The compressibility has no significant effect until 1,700 Hz where the curves suddenly separate.

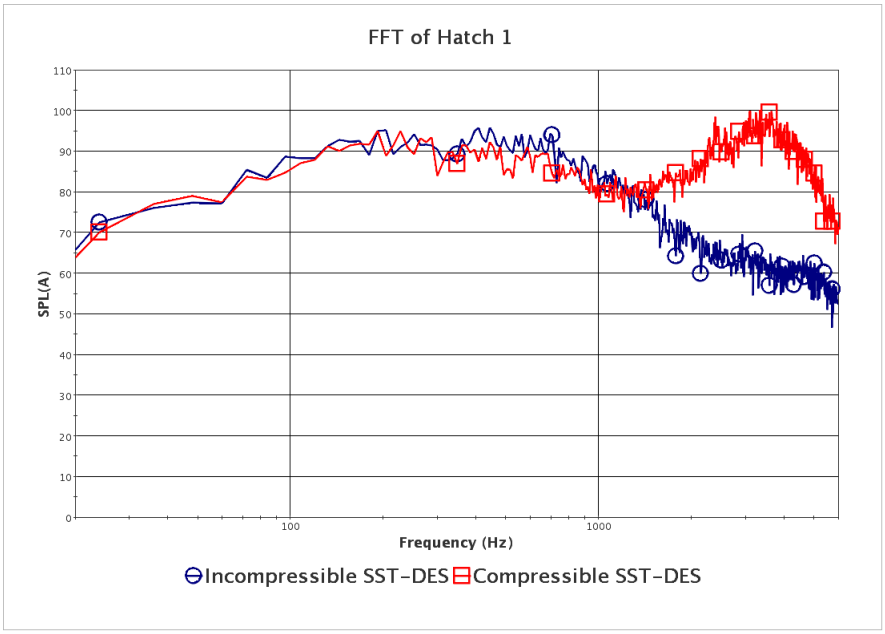

Figure 4.23: Comparison of "Hatch 1"-probe for the incompressible and compressible case using SST-DES. Note the peak at the 2,400 Hz for the compressible flow-curve.

The curves at "Front cavity edge" in Figure 4.26 show a rather good agreement from 20 Hz to 2,000 Hz except for the interval 40 Hz to 100 Hz where they deviate by 5 dB.

For "Leading edge" seen in Figure 4.27 the largest deviations are observed. In the interval 20 Hz to 1,700 Hz the curves deviate at most by 8 dB. At a frequency of 1,700 Hz the curves separate.

To conclude the incompressible simulation agrees mostly very well to the compressible simulation according to the probes that were spread out in the domain. Exceptions occur for high frequencies where abnormally high SPL-values are found.

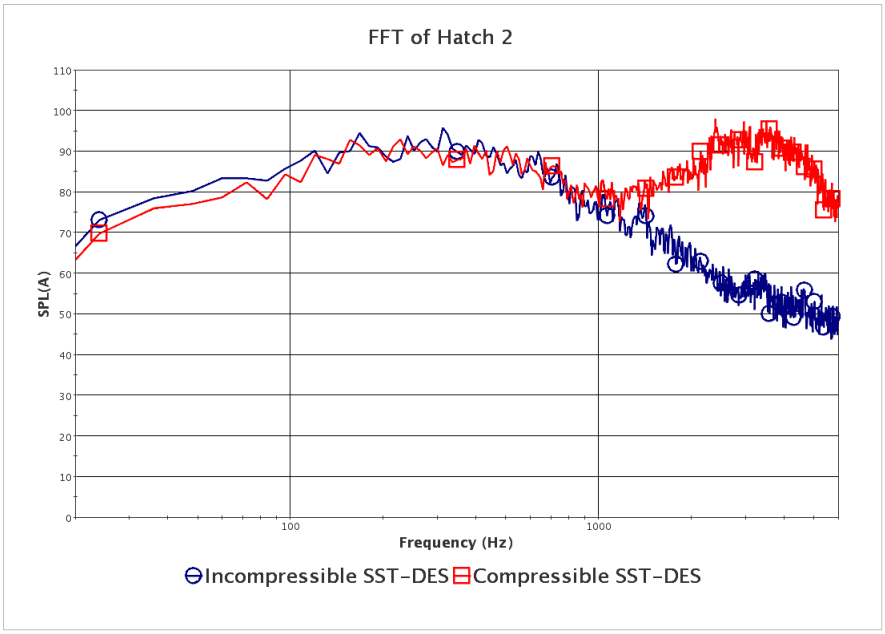

Figure 4.24: Comparison of "Hatch 2"-probe for the incompressible and compressible case using SST-DES. Note the peak at the 2,400 Hz for the compressible flow-curve.

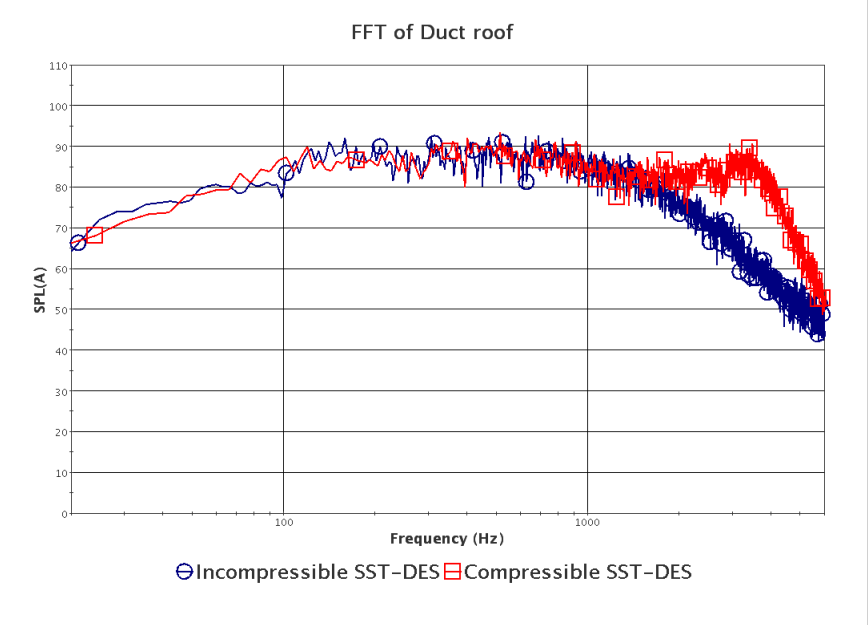

Figure 4.25: Comparison of "Duct roof"-probe for the incompressible and compressible case using SST-DES.

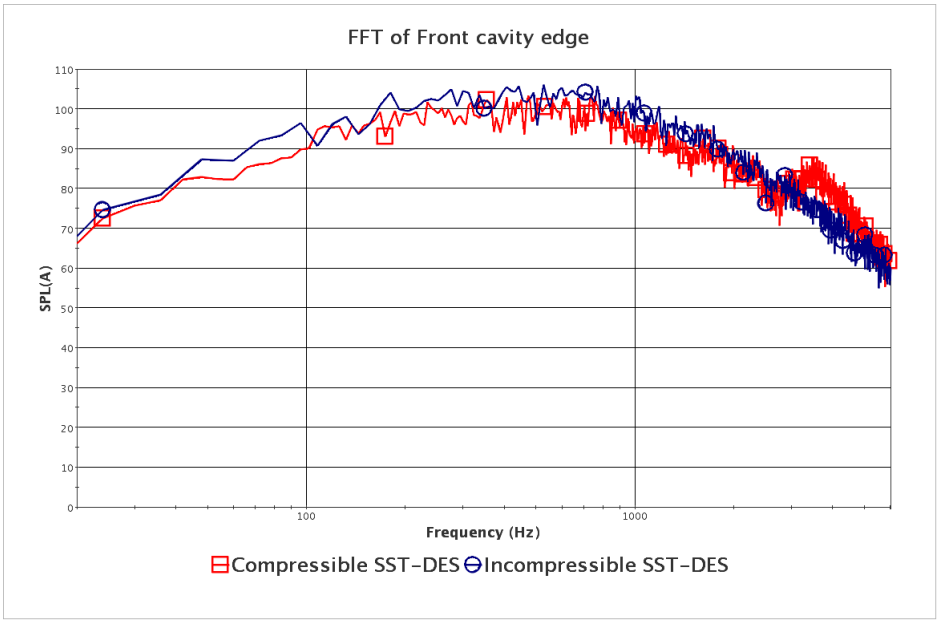

Figure 4.26: Comparison of "Front cavity edge"-probe for the incompressible and compressible case using SST-DES.

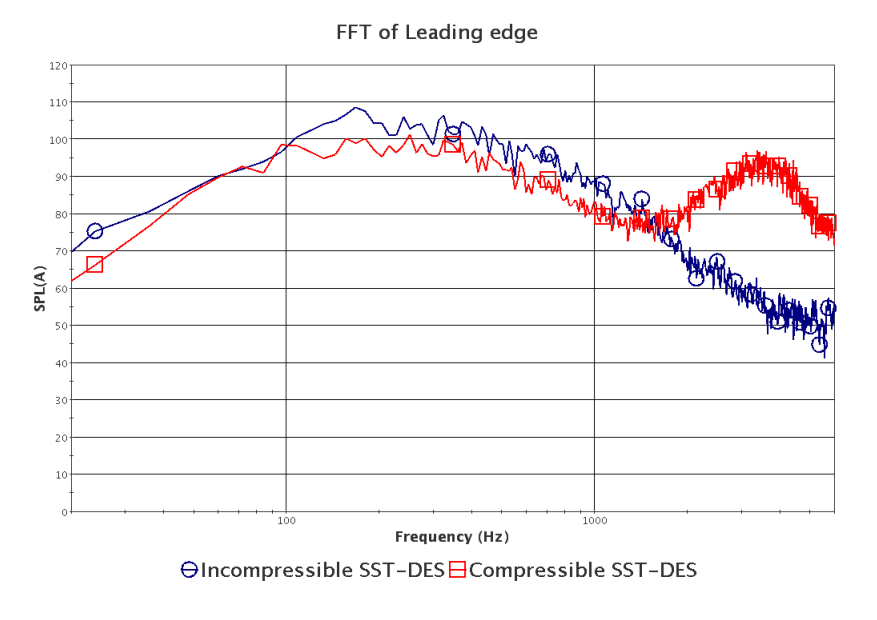

Figure 4.27: Comparison of "Leading edge"-probe for the incompressible and compressible case using SST-DES. The peak at 2,400 Hz is less significant.

4.2.2 FFT of the surface

In Figure 4.28 for 125 Hz the differences due to compressibility effects are fairly small where the incompressible case predicts somewhat stronger sources. For the same frequency the duct figures in Figure 4.29 show off a similar behavior beneath the roofbar. They are almost identical in magnitude with the acoustic sources somewhat spread out.

In Figure 4.30 for 250 Hz the differences become significant. Locally, in the proximity of the roofbar the incompressible case predicts the strongest noise sources, however, the noise sources of the compressible case are more spread out over the hatch with about 10 dB stronger noises on the downstream half. Beneath the roofbar in Figure 4.31 some differences are observed where the incompressible case predicted slightly higher acoustic sources, though at the same areas, as compared to the compressible case.

Considering the downstream part of the hatch the differences become even more significant in Figure 4.32 for 500 Hz where the incompressible case has weak sources with SPL mostly below 60 dB while the compressible case in the same areas have strong sources around 100 dB. Looking at the duct roof in Figure 4.33 higher acoustic sources compared to 250 Hz are observed especially for the incompressible approach. Note the high SPL-values at the edge of the front cavity.

The surface FFT in Figures 4.34a and 4.34b for 1,000 Hz show the same tendencies at the roofbar though not the same magnitude of SPL-values. At the downstream part of the hatch the compressible case shows an almost constant behavior with approximately 25 dB higher SPL-values than for the incompressible case. The SPL-values beneath the roofbar seen in Figure 4.35 are much lower for 1,000 Hz with the incompressible case having the highest values. For the figures so far the incompressible approach seem to predict the same acoustic sources, however, overall the sources the two approaches have in common are more highly predicted in the incompressible case.

Figure 4.36 at a center frequency of 2,500 Hz covers the peak at approximately 2,400 Hz that was found in the monitor plots in Section 4.2.1. The differences here are extremely different as the compressible case have values much larger than the correspondent incompressible case in agreement with the monitor plots viewing the broad-banded and the narrow-banded peak. Under the roofbar in Figure 4.37 there are significant differences as well. The compressible case has a symmetric distribution of pressure fluctuations centrally beneath the roofbar. The incompressible case for the same area have very low SPL-values and a more familiar distribution of fluctuations.

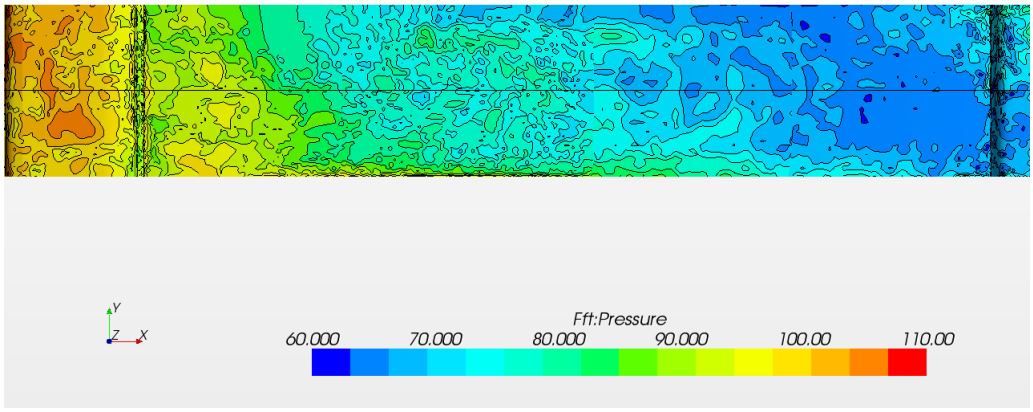

(a) Compressible flow

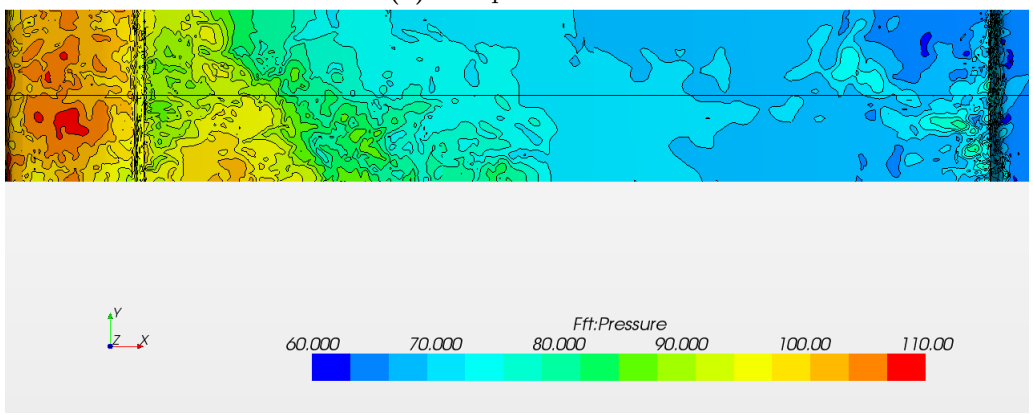

(b) Incompressible flow

Figure 4.28: Comparison of surface FFT between compressible and incompressible flow for a 1/3 octave band with a center frequency of 125 Hz using SST-DES. The results are plotted at the geometry shown in Figure 4.16.

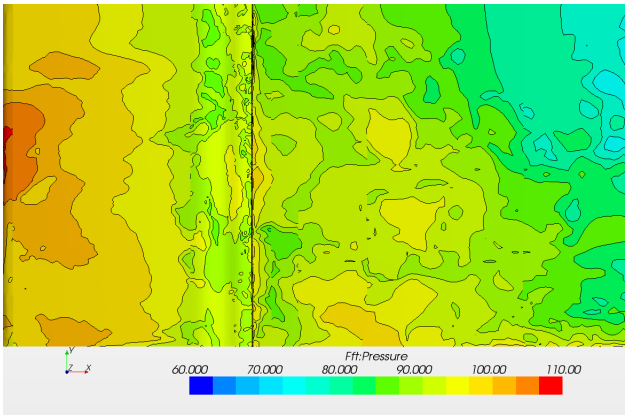

(a) Compressible flow

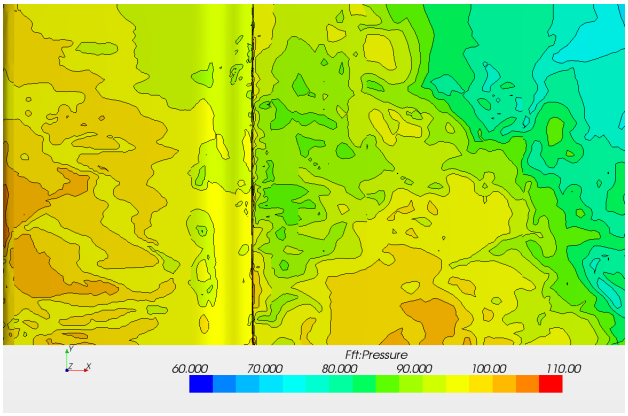

(b) Incompressible flow

Figure 4.29: Comparison of surface FFT between compressible and incompressible flow for a 1/3 octave band with a center frequency of 125 Hz using SST-DES. The roofbar is removed in order to display the duct roof. The results are plotted at the geometry shown in Figure 4.17.

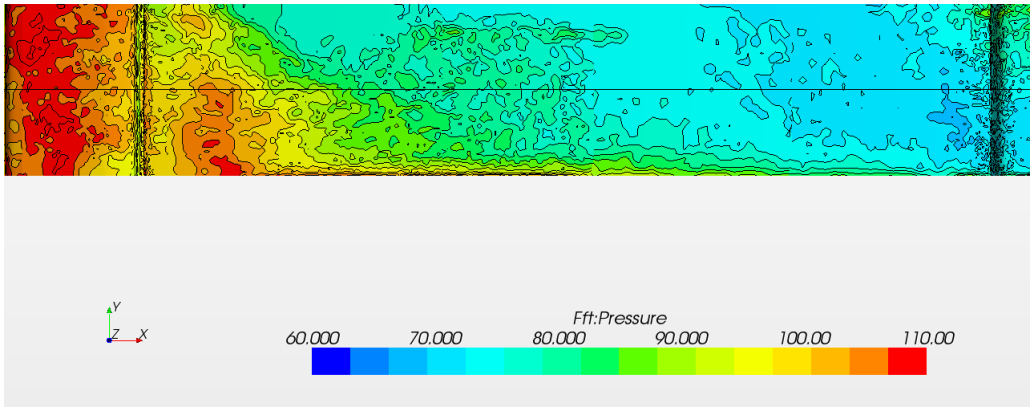

(a) Compressible flow

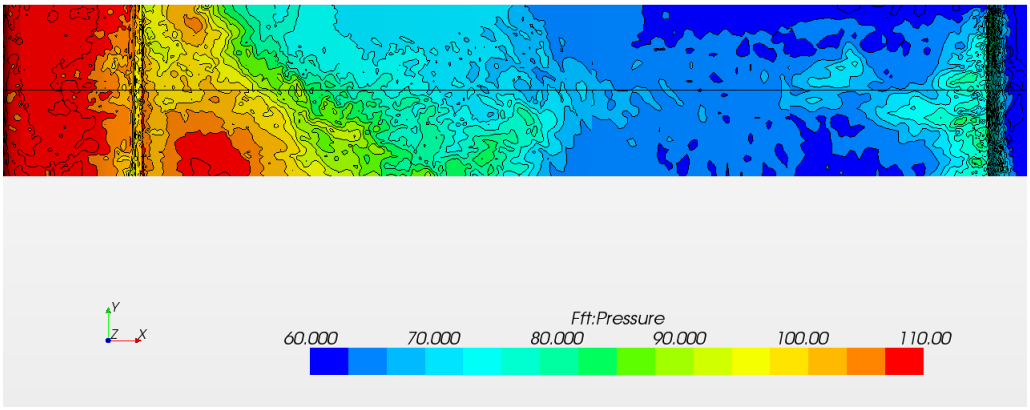

(b) Incompressible flow

Figure 4.30: Comparison of surface FFT between compressible and incompressible flow for a 1/3 octave band with a center frequency of 250 Hz using SST-DES. The results are plotted at the geometry shown in Figure 4.16.

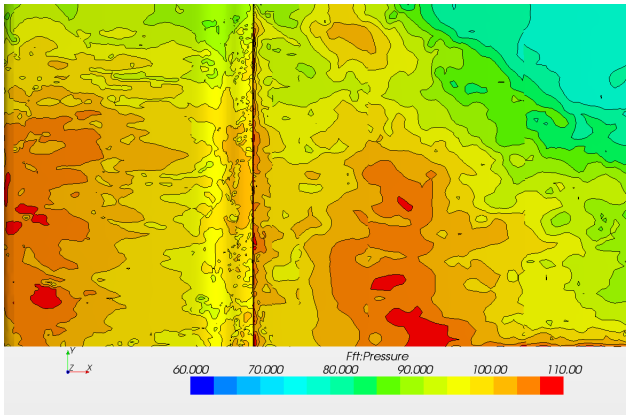

(a) Compressible flow

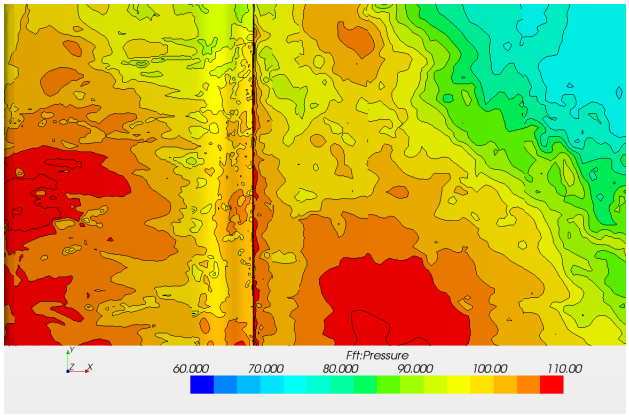

(b) Incompressible flow

Figure 4.31: Comparison of surface FFT between compressible and incompressible flow for a 1/3 octave band with a center frequency of 250 Hz using SST-DES. The roofbar is removed in order to display the duct roof. The results are plotted at the geometry shown in Figure 4.17.

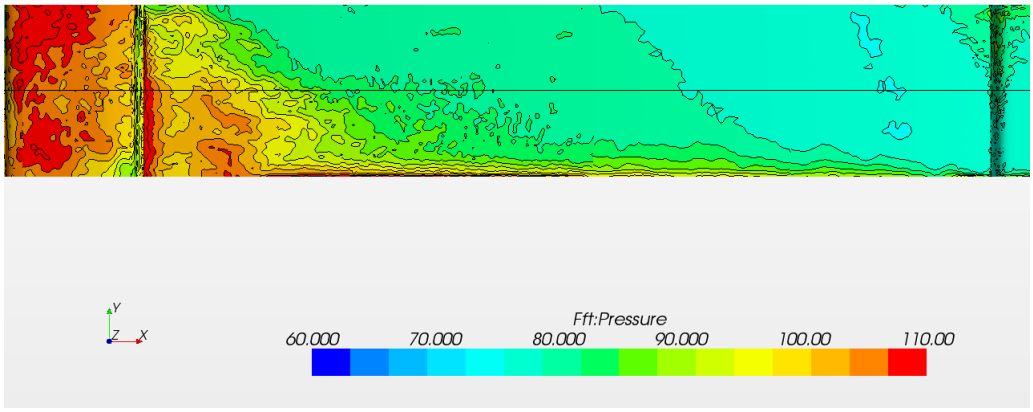

(a) Compressible flow

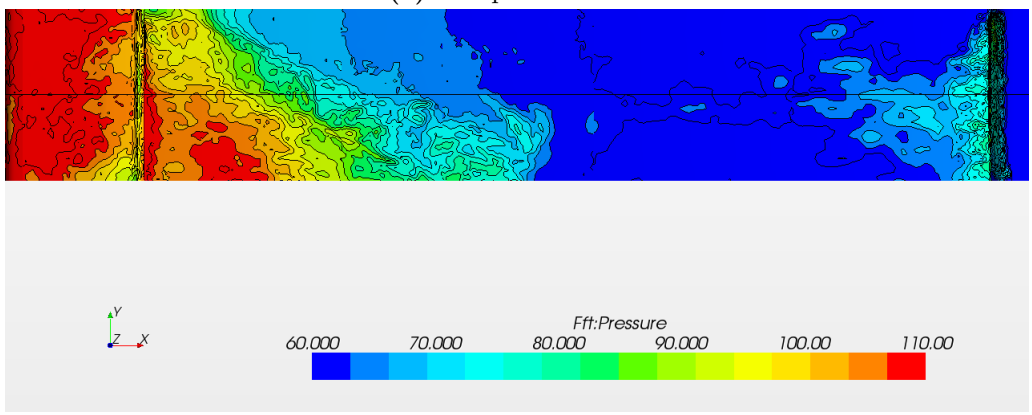

(b) Incompressible flow

Figure 4.32: Comparison of surface FFT between compressible and incompressible flow for a 1/3 octave band with a center frequency of 500 Hz using SST-DES. The results are plotted at the geometry shown in Figure 4.16.

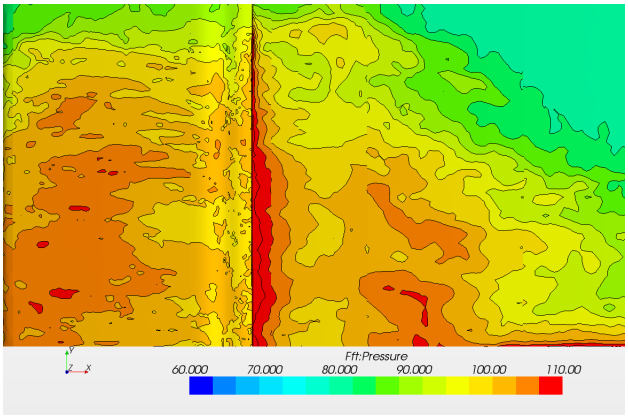

(a) Compressible flow

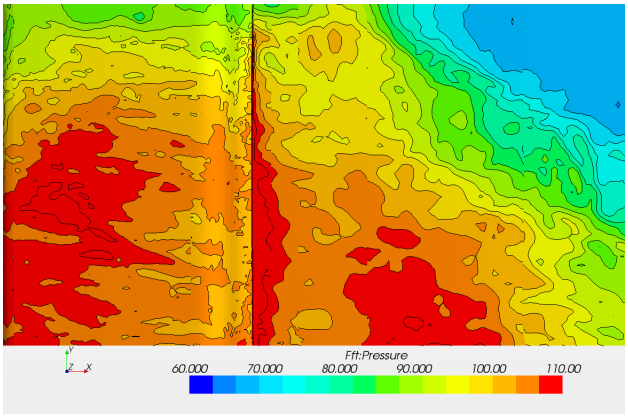

(b) Incompressible flow

Figure 4.33: Comparison of surface FFT between compressible and incompressible flow for a 1/3 octave band with a center frequency of 500 Hz using SST-DES. The roofbar is removed in order to display the duct roof. The results are plotted at the geometry shown in Figure 4.17.

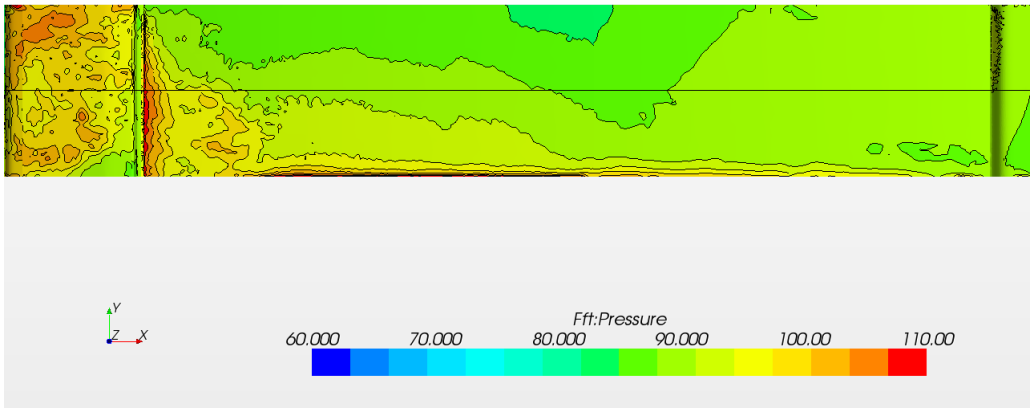

(a) Compressible flow

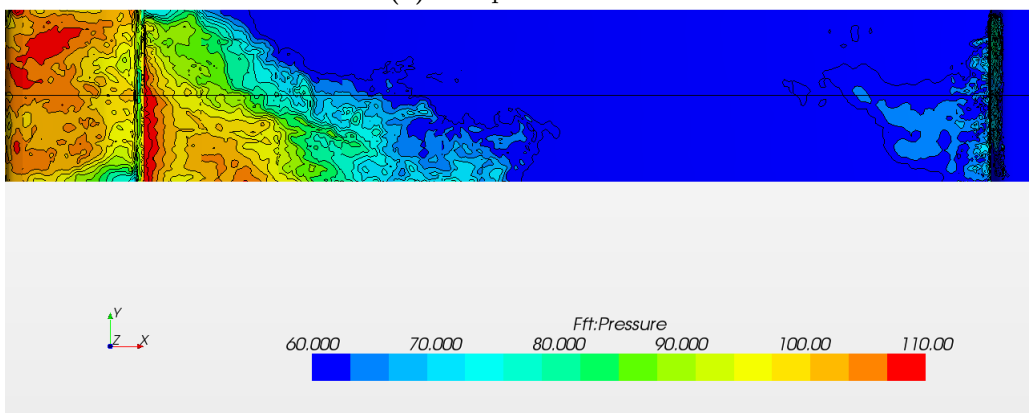

(b) Incompressible flow

Figure 4.34: Comparison of surface FFT between compressible and incompressible flow for a 1/3 octave band with a center frequency of 1,000 Hz using SST-DES. The results are plotted at the geometry shown in Figure 4.16.

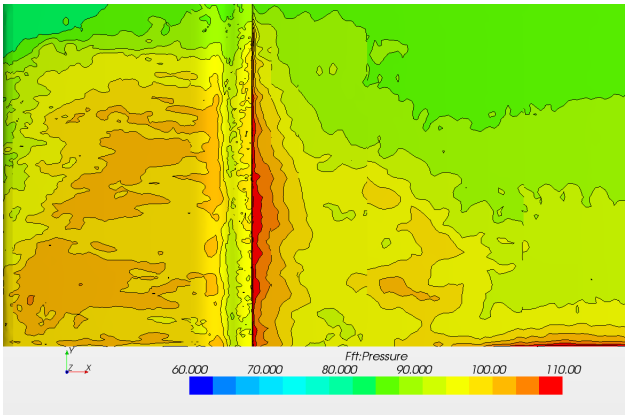

(a) Compressible flow

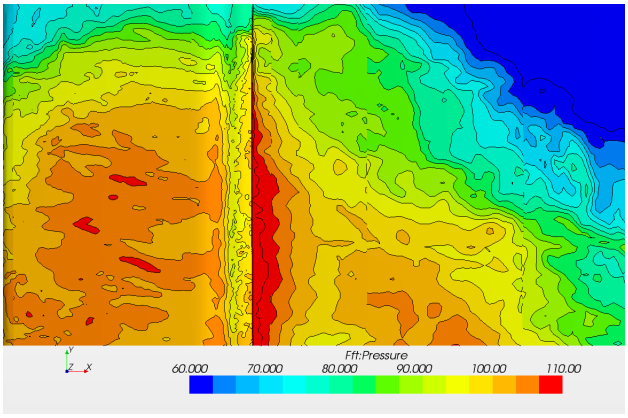

(b) Incompressible flow

Figure 4.35: Comparison of surface FFT between compressible and incompressible flow for a 1/3 octave band with a center frequency of 1,000 Hz using SST-DES. The roofbar is removed in order to display the duct roof. The results are plotted at the geometry shown in Figure 4.17.

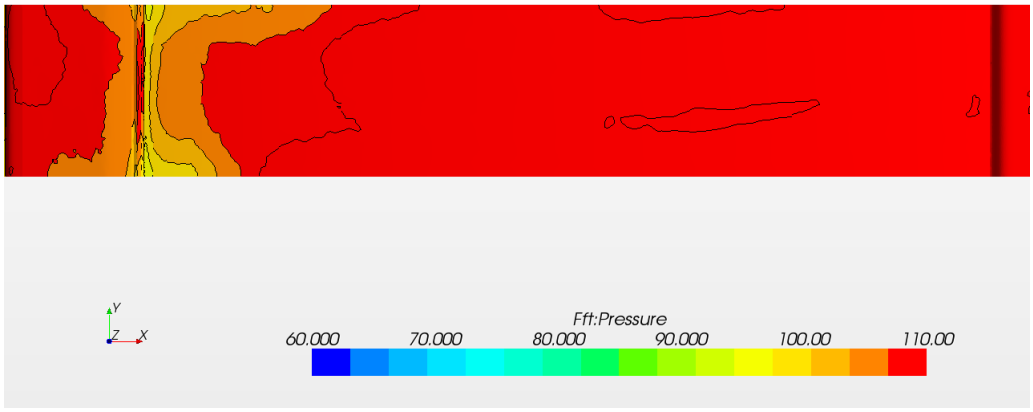

(a) Compressible flow

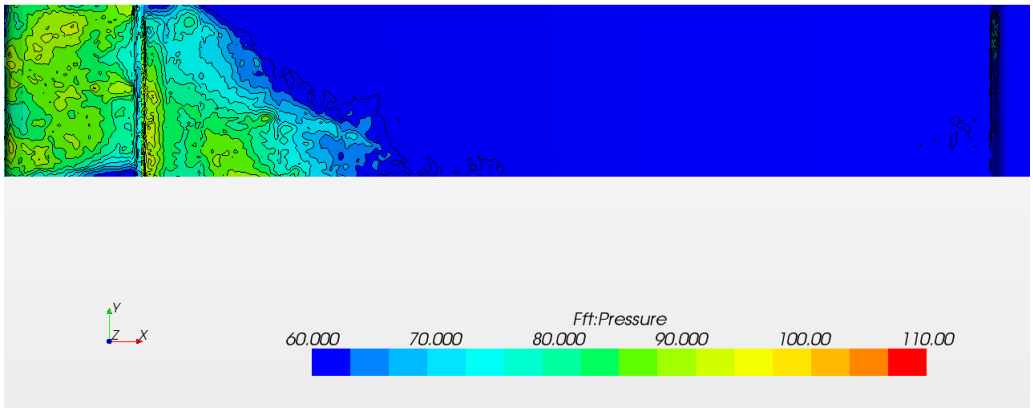

(b) Incompressible flow

Figure 4.36: Comparison of surface FFT between compressible and incompressible flow for a 1/3 octave band with a center frequency of 2,500 Hz using SST-DES. This interval covers the narrow peak at 2,400 Hz. The results are plotted at the geometry shown in Figure 4.16.

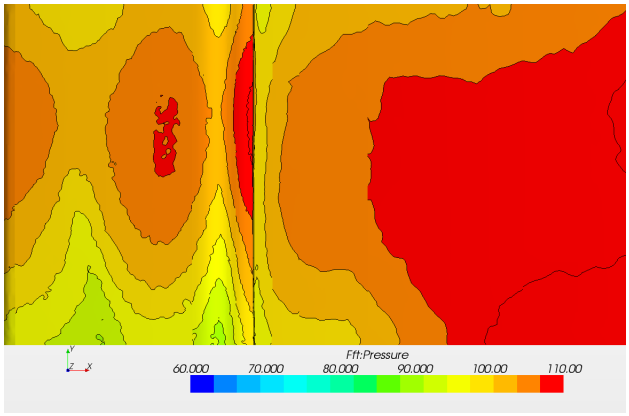

(a) Compressible flow

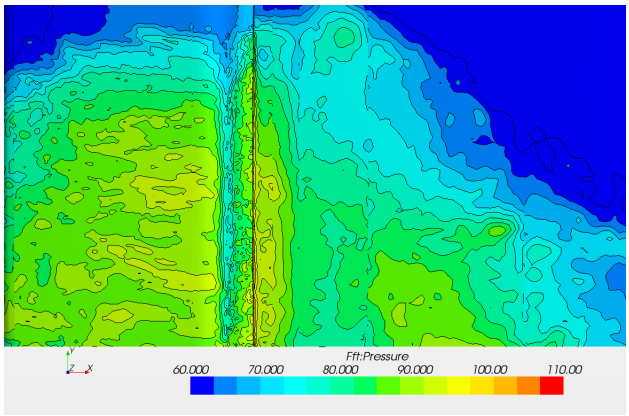

(b) Incompressible flow

Figure 4.37: Comparison of surface FFT between compressible and incompressible flow for a 1/3 octave band with a center frequency of 2,500 Hz using SST-DES which involves the peak observed. The roofbar is removed in order to display the duct roof. The results are plotted at the geometry shown in Figure 4.17.

4.3 Comparing the incompressible DES-models with the incompressible LES

In this section the DES-models are compared with LES using an incompressible approach.

4.3.1 FFT of monitors

In Figure 4.38 for "Hatch 1" the curves agree fairly good for both of the DES-models although SST-DES seems to lie slightly closer to LES than SA-DES does. Looking at "Hatch 2" in Figure 4.39 the difference is more significant although neither one of the models are actually close until 1,000 Hz where the curves of the DES-models connects with the LES-curve and then dive.

Focusing on "Leading edge" which results can be seen in Figure 4.40 the DES-models and LES are lying aligned with each other until 400 Hz where the first curves are diving. In Figure 4.41 where the "Top" is considered rather large deviations are observed from low frequencies up to about 600 Hz where the curves of the DES-models turn downwards. LES has much lower values than the DES-models.

The behavior for "Front cavity edge" can be seen in Figure 4.42. SST-DES and SA-DES follows the same path through the entire interval of the frequency spectrum. They are both overestimating by 5 dB and connects with the LES-curve at 300 Hz but separate at 1,200 Hz.

In Figure 4.43 SST-DES lies closer to LES than SA-DES does. The first follows LES perfectly up to 1,100 Hz where it dives. Up to the same frequency SA-DES makes a constant overestimation of 5 dB.

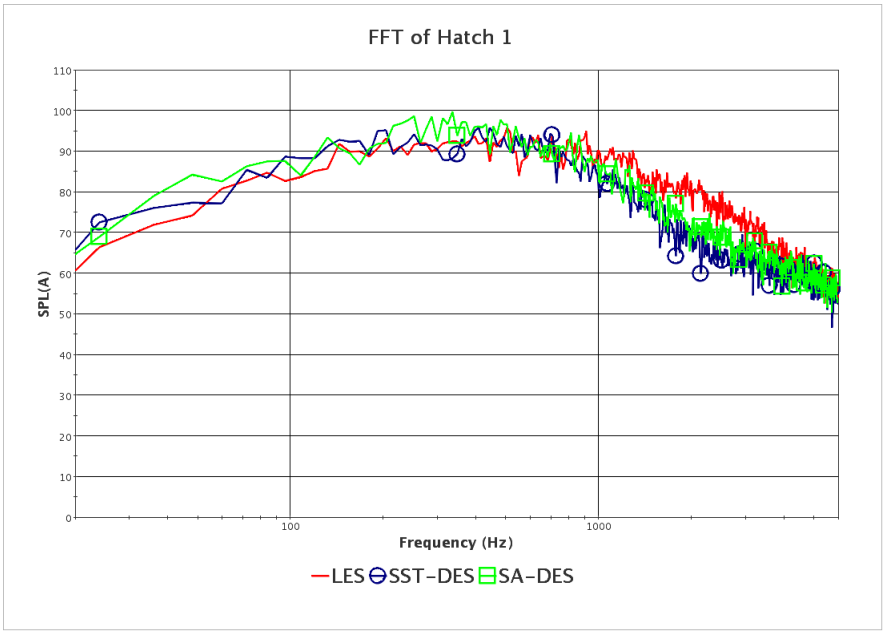

Figure 4.38: Comparison of the DES-models with LES for the "Hatch 1"-probe.

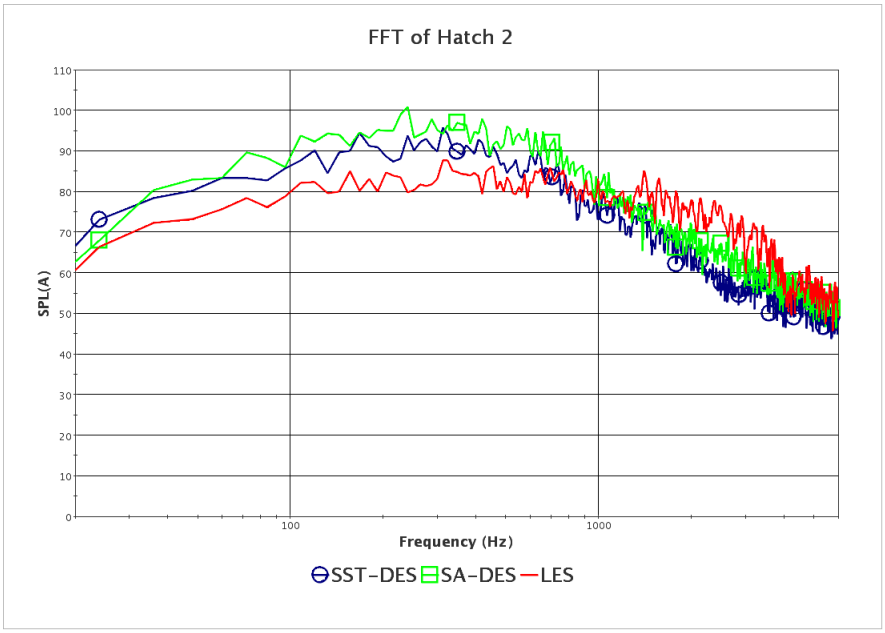

Figure 4.39: Comparison of the DES-models with LES for the "Hatch 2"-probe.

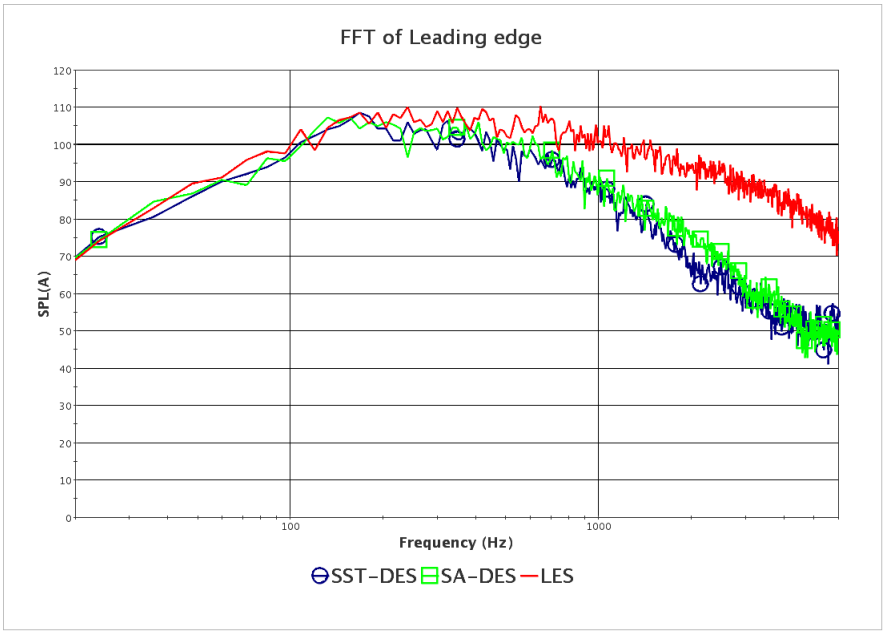

Figure 4.40: Comparison of the DES-models with LES for the "Leading edge"-probe.

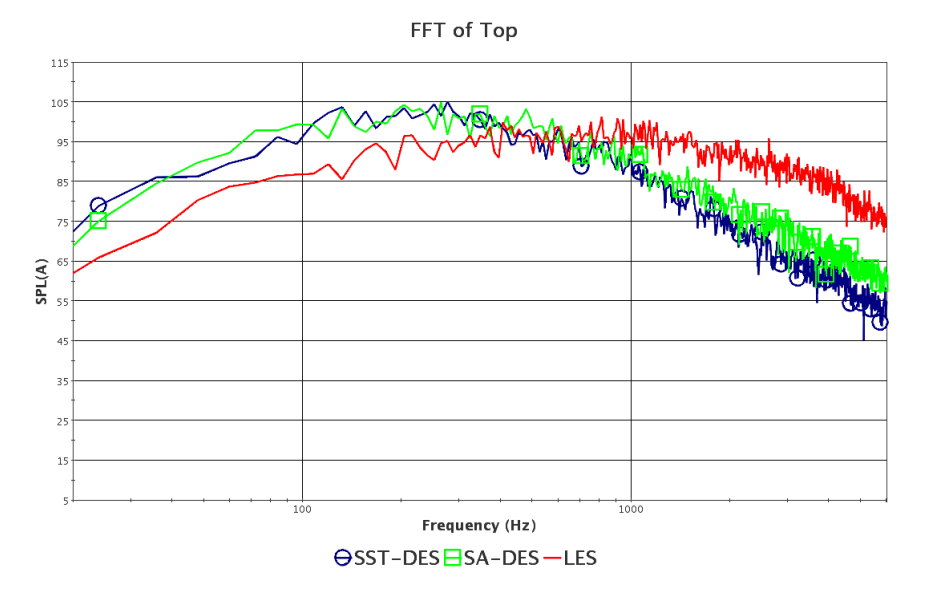

Figure 4.41: Comparison of the DES-models with LES for the "Top"-probe.

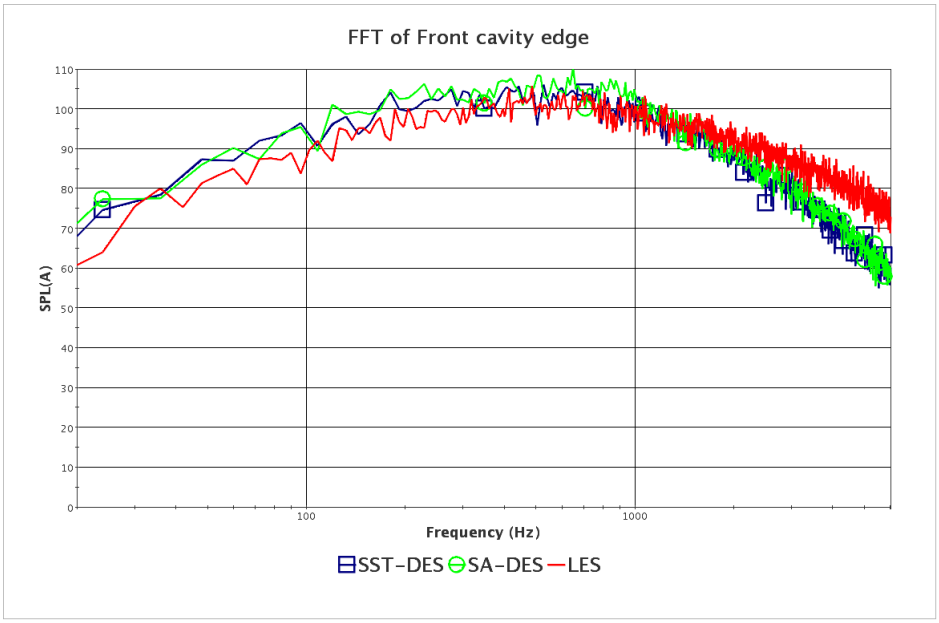

Figure 4.42: Comparison of the DES-models with LES for the "Front cavity edge"-probe.

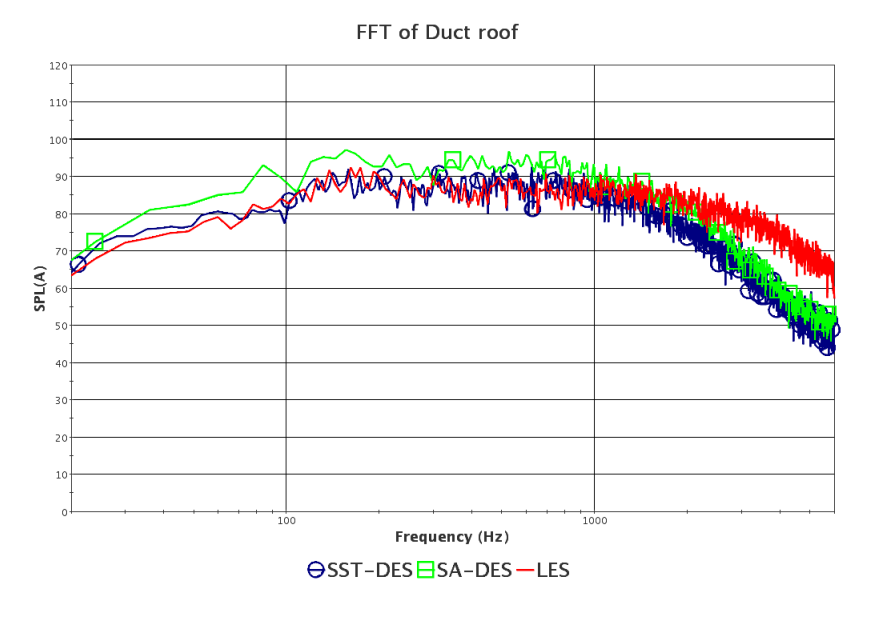

Figure 4.43: Comparison of the DES-models with LES for the "Duct roof"-probe.

4.3.2 FFT of the surface

Figure 4.44 shows that for 125 Hz there is a resemblance between the DES-models while LES is different since it produces a long "tail" of noise down the hatch. The LES result reminds of the results of the compressible SST-DES but with higher levels. LES has the largest acoustic sources at the leading edge while the other two have their largest values on top of the roofbar.

The same results although larger SPL-values are found for 250 Hz in Figure 4.46. At the far right of the hatch the DES-simulations produce noise close and inside the rear cavity that are isolated from the noise at the left side of the hatch. The DES-simulations also produce stronger noise on the top of the roofbar. They match LES fairly good until the point of one third downstream on the hatch where they suddenly drop below 60 dB. The same tendencies are found for 500 Hz and 1,000 Hz, however, the sources become weaker for increasing frequencies which is shown in Figures 4.48 and 4.50.

Under the roofbar in Figure 4.45 for 125 Hz the SPL-magnitudes SST-DES lies closer to LES than SA-DES does since SA-DES over-predicts to some extent.

In Figure 4.47 for 250 Hz SA-DES generally predicts as closely to LES as SST-DES does. The front cavity and the sources at the hatch have lower values for SST-DES.

In Figure 4.49 for 500 Hz SST-DES lies closer to LES than the overpredicting SA-DES does. However, SST-DES seems, relative LES, to under-predict the inlet to the cavity which SA-DES manages to capture.

For 1,000 Hz, in Figure 4.51, the largest differences occur between DES and LES. Except for at the cavity inlet SA-DES and SST-DES are almost identical. LES, however, has larger values at the duct roof.

Generally, for all surface FFT-plots the noise sources seem to be twisted towards the negative y-direction instantly after the roofbar.

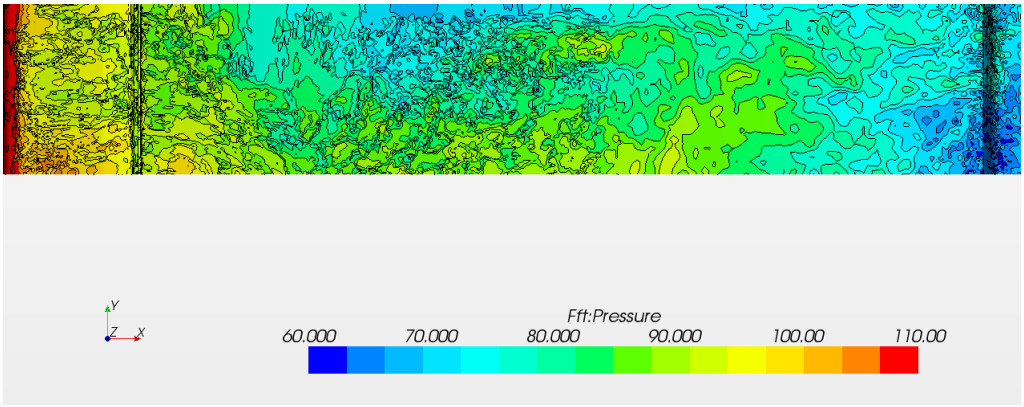

(a) LES

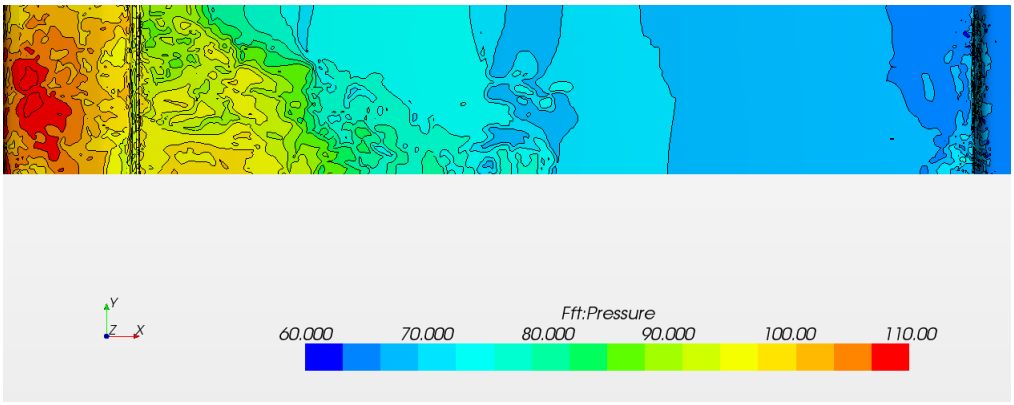

(b) SA-DES

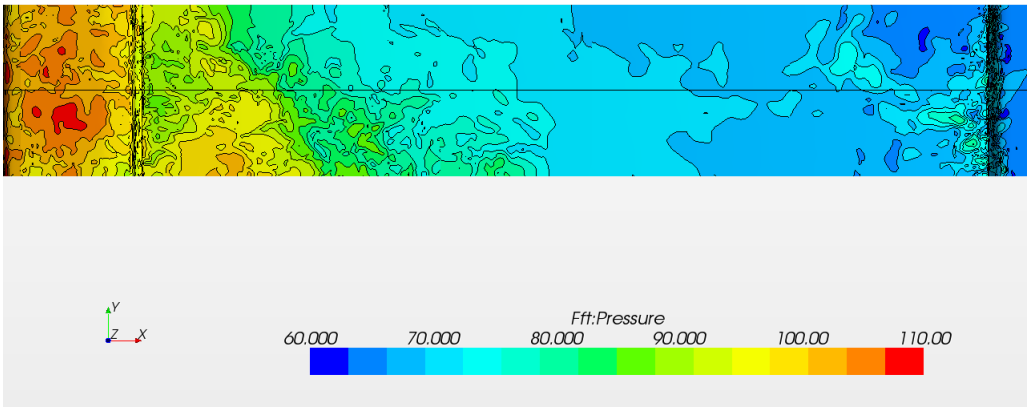

(c) SST-DES

Figure 4.44: Comparison of surface FFT between LES and the DES-models for a 1/3 octave band with a center frequency of 125 Hz. The results are plotted at the geometry shown in Figure 4.16.

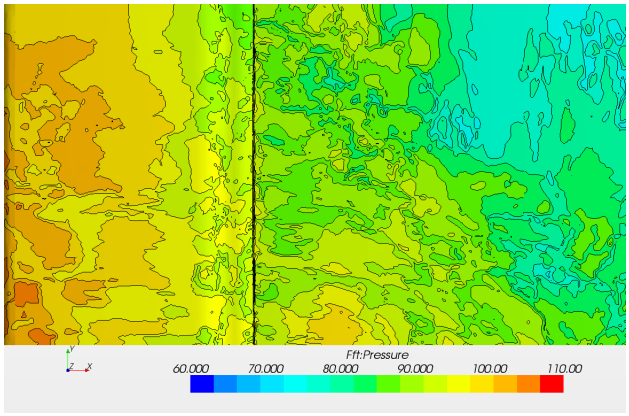

(a) LES

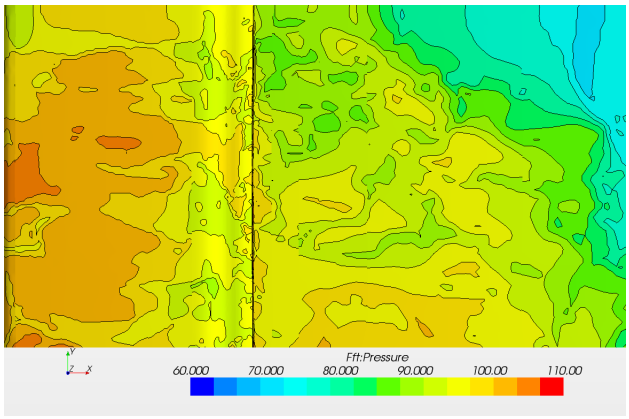

(b) SA-DES

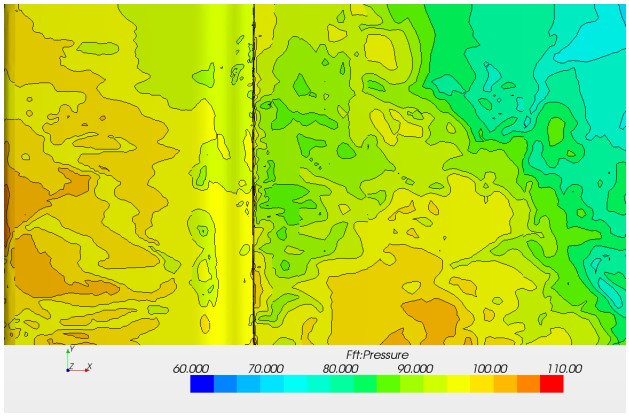

(c) SST-DES

Figure 4.45: Comparison of surface FFT between LES and the DES-models for a 1/3 octave band with a center frequency of 125 Hz. The roofbar has been removed in order to display the duct roof. The results are plotted at the geometry shown in Figure 4.17.

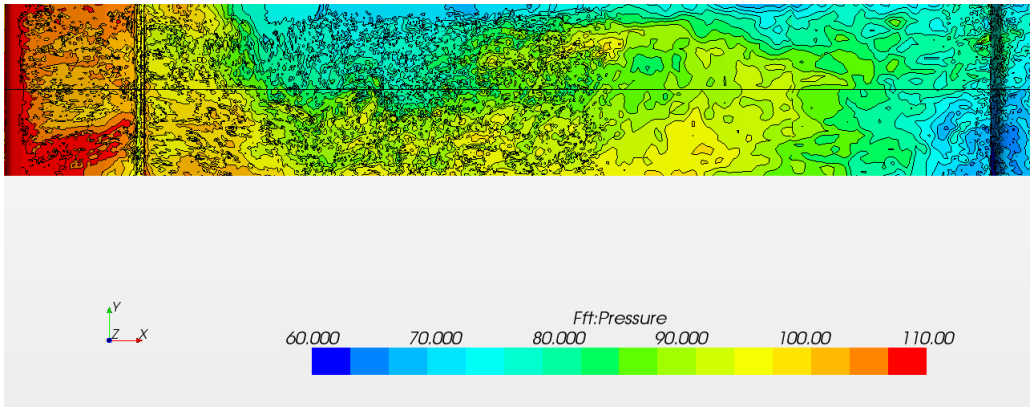

(a) LES

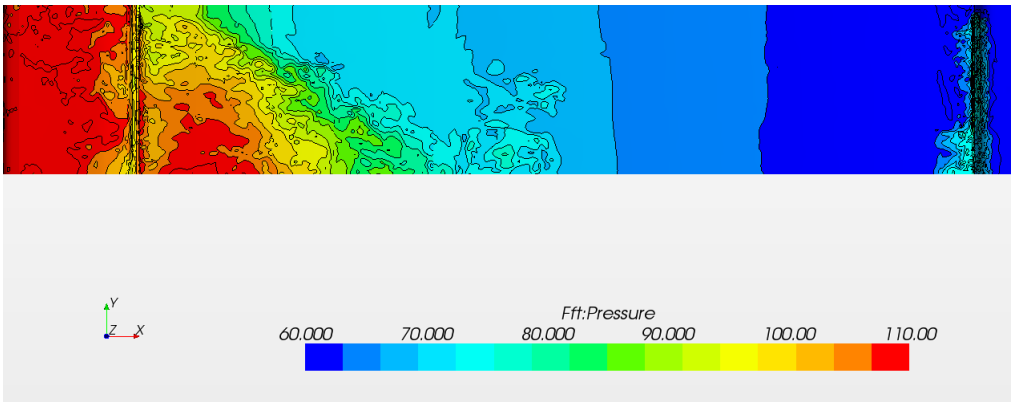

(b) SA-DES

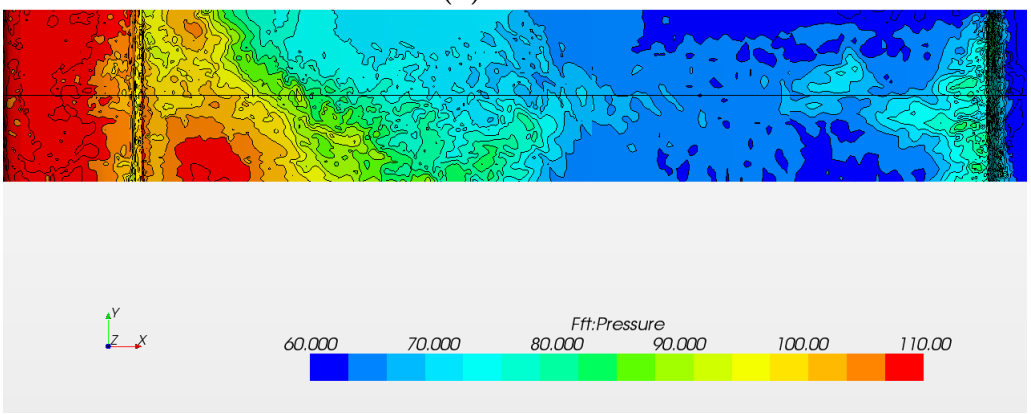

(c) SST-DES

Figure 4.46: Comparison of surface FFT between LES and the DES-models for a 1/3 octave band with a center frequency of 250 Hz. The results are plotted at the geometry shown in Figure 4.16.

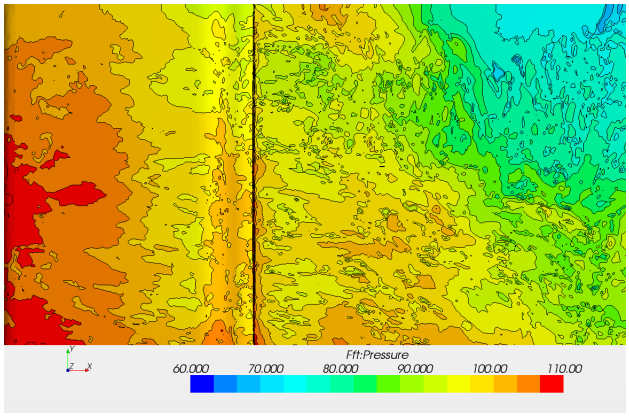

(a) LES

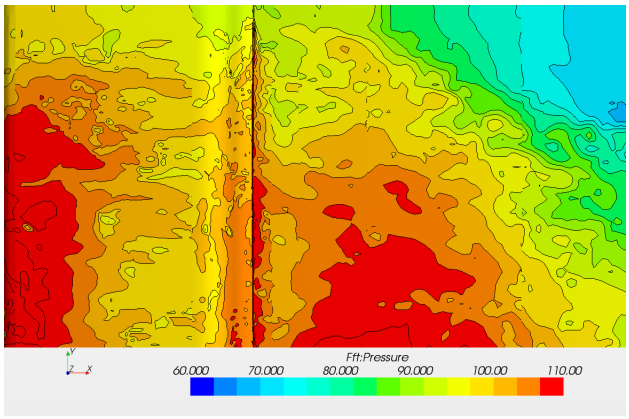

(b) SA-DES

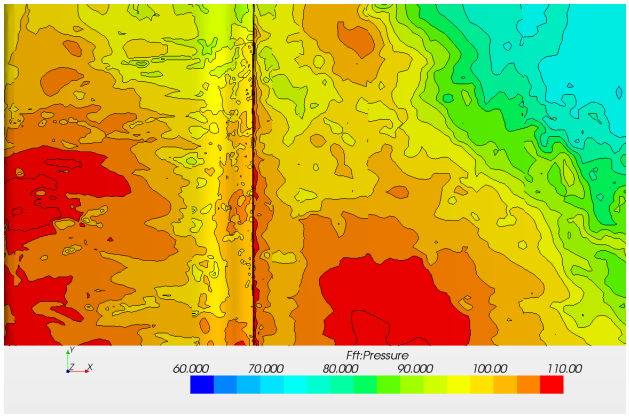

(c) SST-DES

Figure 4.47: Comparison of surface FFT between LES and the DES-models for a 1/3 octave band with a center frequency of 250 Hz. The roofbar has been removed in order to display the duct roof. The results are plotted at the geometry shown in Figure 4.17.

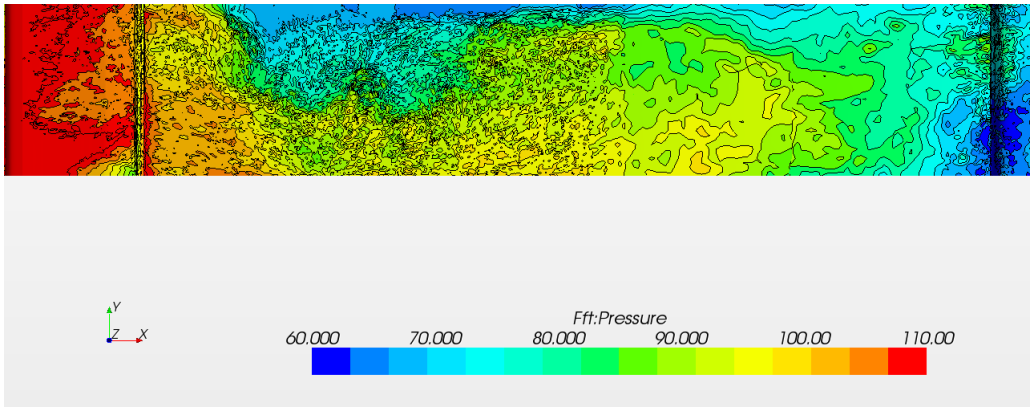

(a) LES

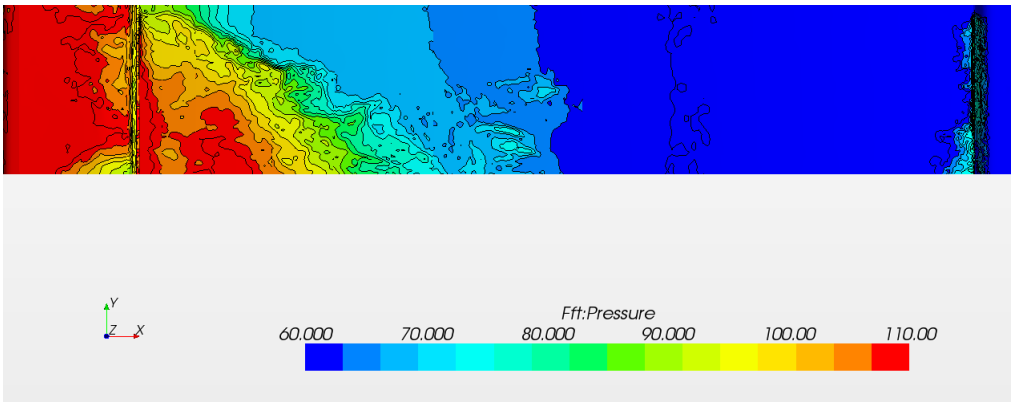

(b) SA-DES

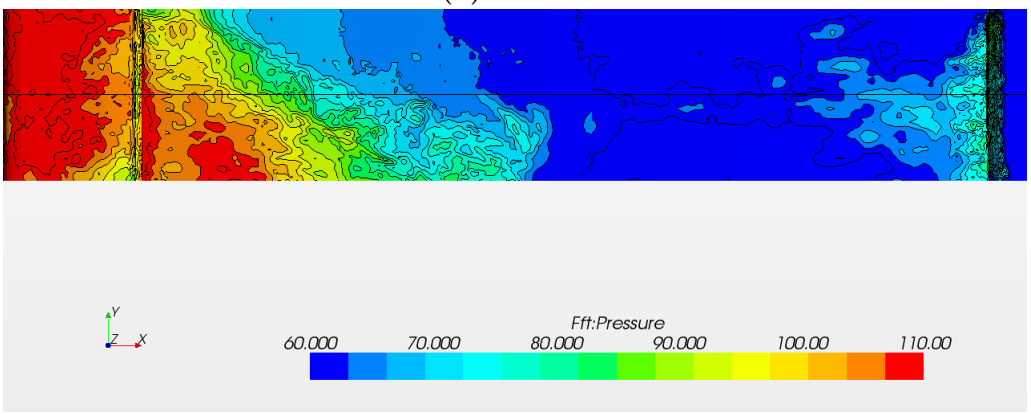

(c) SST-DES

Figure 4.48: Comparison of surface FFT between LES and the DES-models for a 1/3 octave band with a center frequency of 500 Hz. The results are plotted at the geometry shown in Figure 4.16.

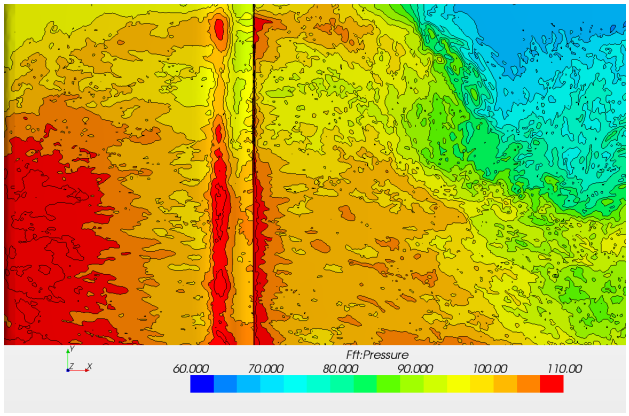

(a) LES

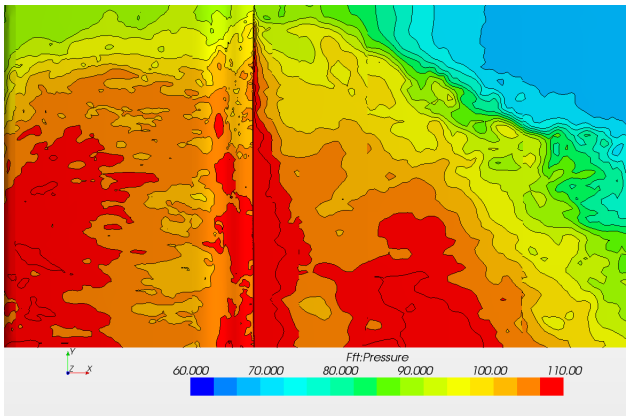

(b) SA-DES

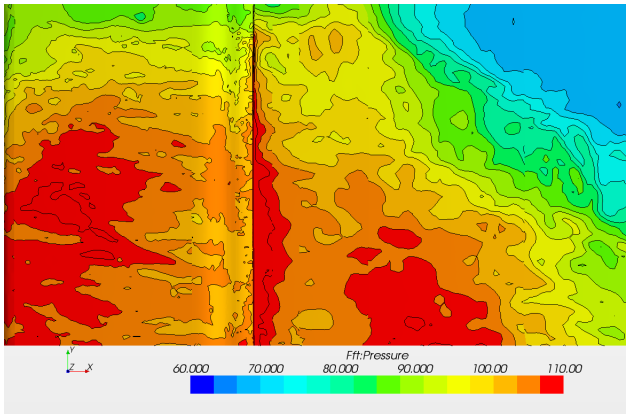

(c) SST-DES

Figure 4.49: Comparison of surface FFT between LES and the DES-models for a 1/3 octave band with a center frequency of 500 Hz. The roofbar has been removed in order to display the duct roof. The results are plotted at the geometry shown in Figure 4.17.

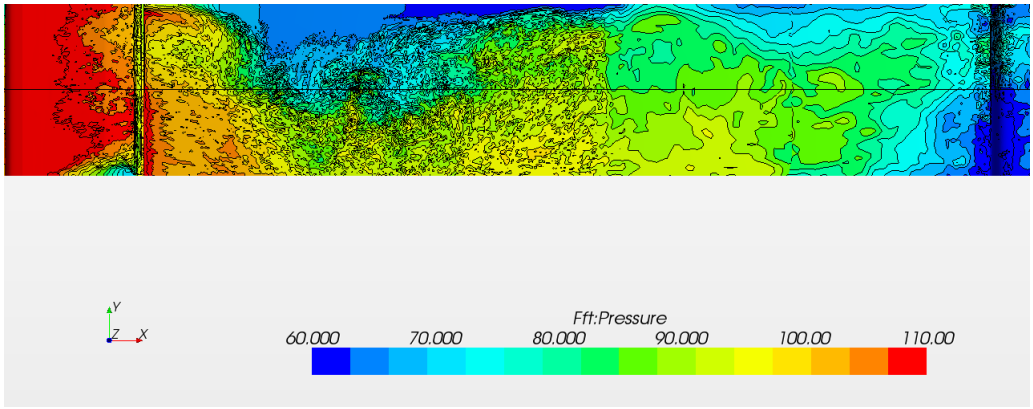

(a) LES

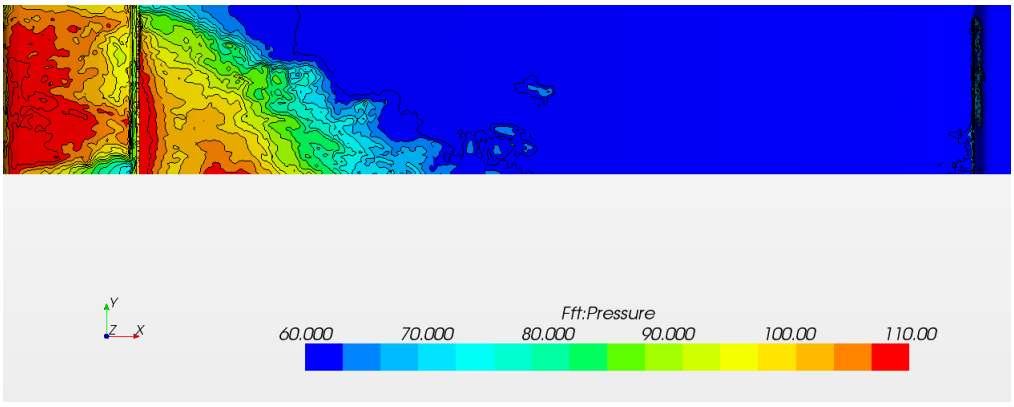

(b) SA-DES

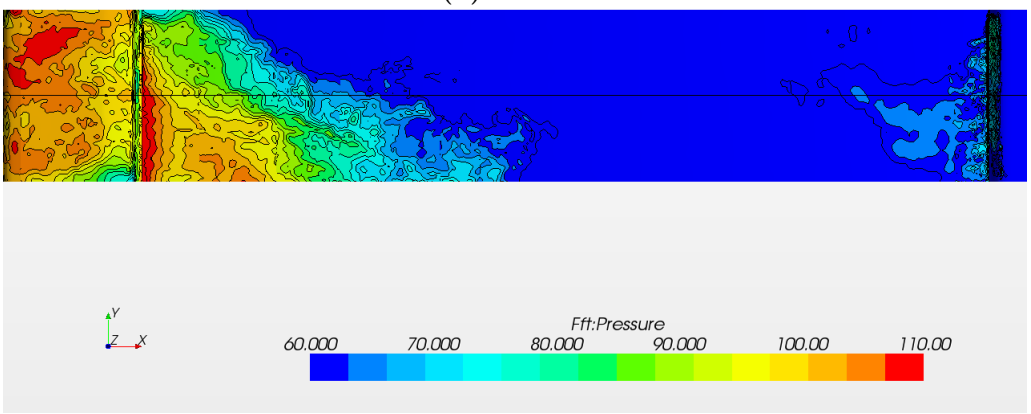

(c) SST-DES

Figure 4.50: Comparison of surface FFT between LES and the DES-models for a 1/3 octave band with a center frequency of 1,000 Hz. The results are plotted at the geometry shown in Figure 4.16.

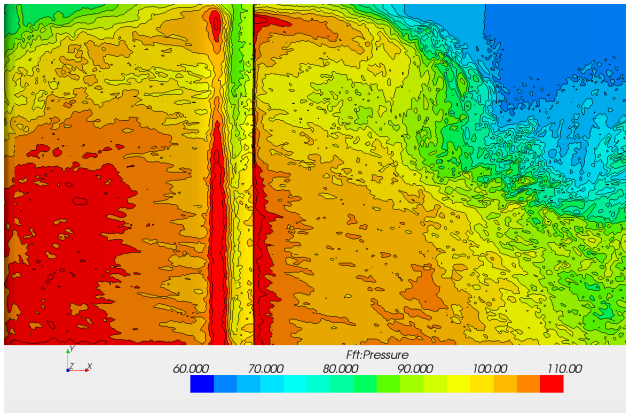

(a) LES

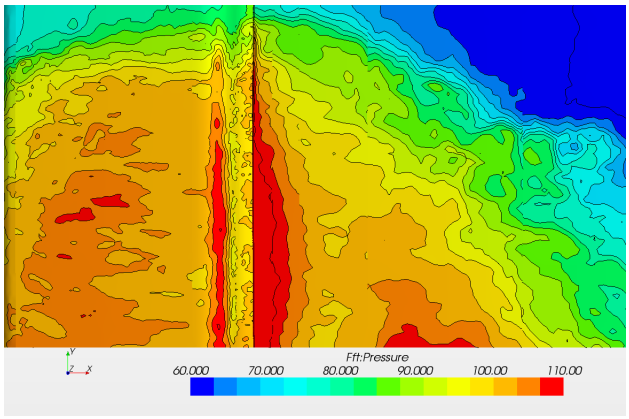

(b) SA-DES

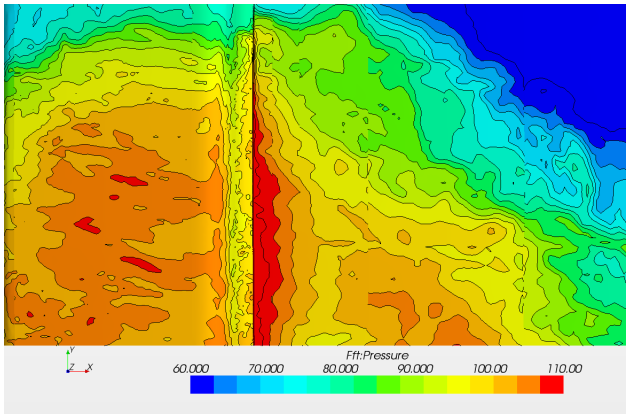

(c) SST-DES

Figure 4.51: Comparison of surface FFT between LES and the DES-models for a 1/3 octave band with a center frequency of 1,000 Hz. The roofbar has been removed in order to display the duct roof. The results are plotted at the geometry shown in Figure 4.17.

4.4 Impact of the spoiler

From Figures 4.52 and 4.53 showing ”Hatch 1” and ”Hatch 2” it could be seen that the results are identical from low to high frequencies with some minor differences.

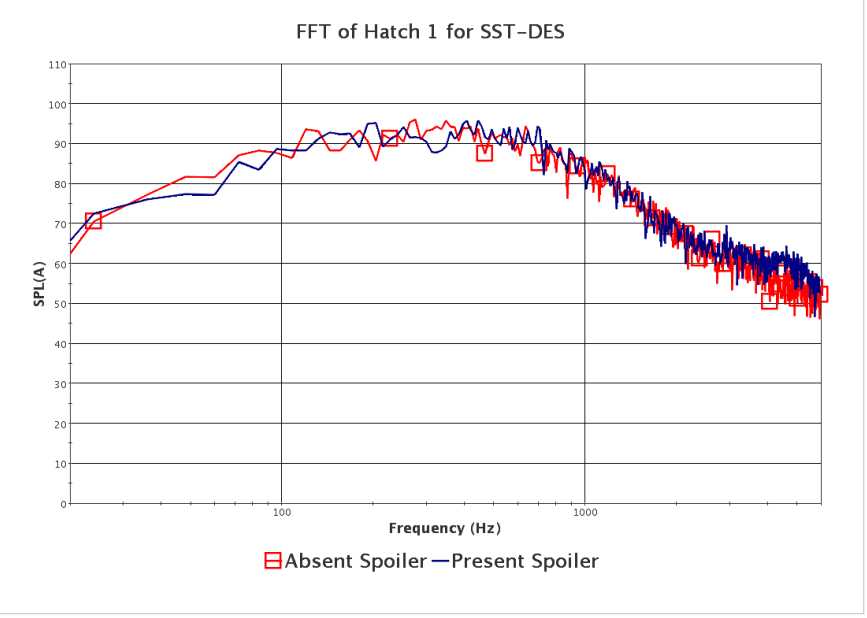

Figure 4.52: Impact of the removed spoiler for ”Hatch 1”-probe.

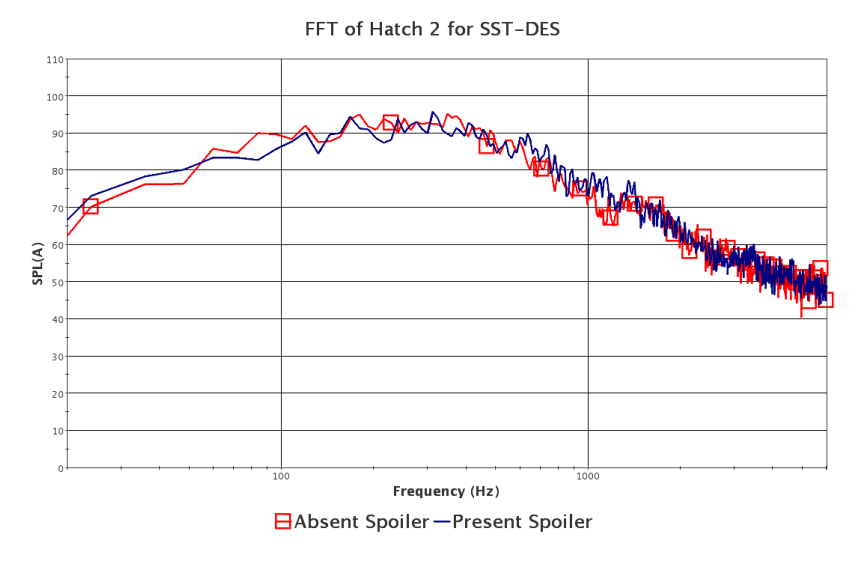

Figure 4.53: Impact of the removed spoiler for ”Hatch 2”-probe.

4.5 Averaging "Hatch 2"

As mentioned in Section 3.4.2 and seen in Figure 3.10 "Hatch 2" is surrounded by four other probes in order to compute an average so that spatial variations of pressure fluctuations can be accounted for. This is seen in Figure 4.54a where the averaged curve lies in between the others. The average was made in MATLAB and is described in Appendix A.2.2. Note that the SPL-value is not A-weighted since no A-weighting filter was available.

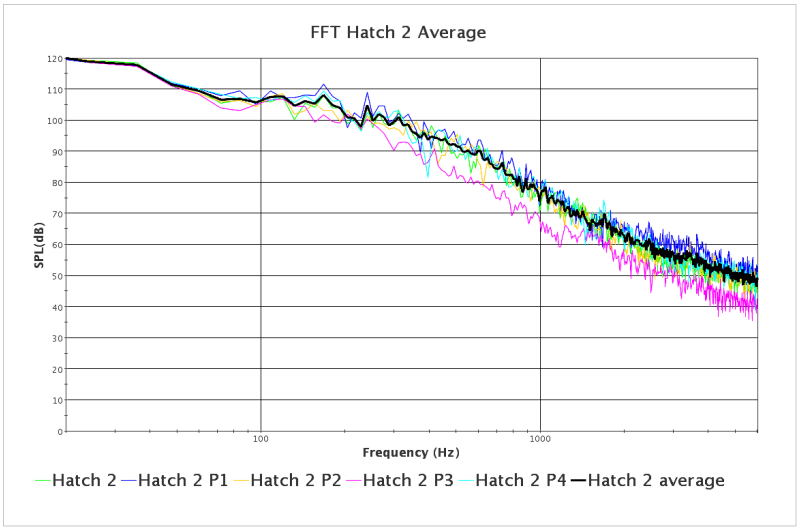

(a) Correct approach.

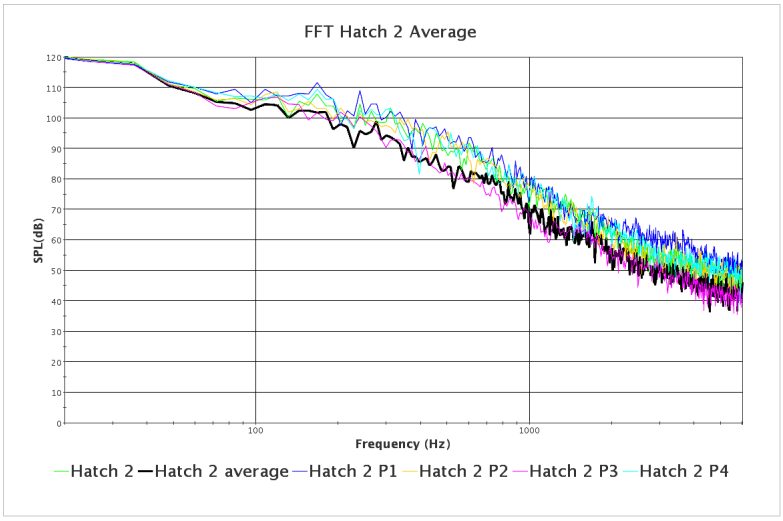

(b) Incorrect approach.

Figure 4.54: Average of the probes involved with "Hatch 2" using unweighted SPL-values. The averages are the thick black curves.

At first the averaging was made in the time-domain which gave an average that lied beneath the curves that it was supposed to lie in between which can be seen in Figure 4.54b. This average was made using StarCCM+-code and the procedure is described in Appendix A.2.1.

4.6 Tonal peaks

Using Eq. (2.31) with an estimated vortex transport velocity of $u_v = 21$ m/s obtained from picking a value from the contour-plot and a length of $L = 0.012$ m the Rossiter's frequency becomes $f_R = 1650$ Hz which is not visible in any of the monitor plots displayed.

In [32] the Helmholtz frequency was calculated to be approximately 2,600 Hz which lies rather close to the peak at 2,400 Hz observed in the monitor plots.

4.7 Total solver time

The times needed for solving each case for mesh M2 and M3 using 144 cores are presented in Table 4.7. LES was as expected the most computationally demanding approach followed by the compressible SST-DES. The incompressible case of the latter was the second least demanding while SA-DES was the least demanding.

Table 4.7: Solver times for cases with meshes M2 & M3.

Case	**Solver time (h)**
H1FVLES	150
H1FCSSTDES	120
H1FVSSTDES	95
H1FVSADES	83

5 Discussion

Under the discussion section attempts to explain the results are made.

Probes "Hatch 3", "Hatch 4" and "Rear cavity" were not included in the results since no turbulent scales were developed that far downstream in the domain when using the incompressible DES-models. "Bottom of roofbar" was not included since "Duct roof" was representing the section where they both were located. The probes that were not placed at a solid surface but in the volume were not included because only dipole sources were relevant.

5.1 On the flow-field results

The incompressible DES-simulations showed good resemblance with each other, however, for the compressible flow turbulent scales were developed further downstream in the domain as seen in Figure 4.18. Firstly, this might be due to that the freestream boundary conditions are flexible in the sense that the flow can slightly affect the values at the boundary. Secondly, air is flowing into the volume beneath the spoiler which creates a pressure drop which might induce downstream transportation of scales. In contrast, for the incompressible case, velocity inlet boundary conditions are more stiff of nature than the freestream boundary conditions and do not change values. Since the domain is only 15 cm wide the left and right boundary conditions are expected to have an abnormally large impact on the solution. Additionally, since air is flowing upstream from the spoiler volume this decelerates the flow field over the hatch.

In Figure A.57 it is obvious that the boundaries of the incompressible approaches were not changed while this was not the case for the compressible approach although the boundary conditions initially were identical. By looking closely at Figure A.57b it is seen that the backward flow under the spoiler-gap, which is visible for the other cases, is dissolved for the freestream boundary condition and instead directed in the opposite direction which should help the turbulent scales from the roofbar to be transported downstream.

The reason why the flow accelerates beneath the roofbar is that the cross-sectional area becomes smaller in the stream-wise direction. The acceleration occurs in accordance with the continuity equations, Eq. (2.1a) and Eq. (2.3a) .

5.2 On the compressibility effects

Compressibility had a large impact on the results during the simulations. By looking at Figures 4.23 - 4.27 a clear broadbanded peak emerged above 1,000 Hz. Inside this broadbanded peak a narrowbanded peak is visible at a frequency of 2,400 Hz. By using the fundamental frequency-wavelength relationship $\lambda = a_\infty / f$ the acoustic wavelength becomes $\lambda = 0.145$ m which approximately corresponds to the thickness of the computational domain which is 0.15 m. A strong standing wave is most likely developed. Figure A.58 shows the state of the left boundary where huge pressure fluctuations have appeared. This phenomenon could be explained by the features of the freestream bound-

ary condition. As mentioned in Section 3.6.2.3 this boundary condition cannot handle turbulent structures very well. The fact that the domain is much thinner than the height and length of the domain does not mitigate the problem. Additionally, a spherical domain would have been more appropriate to use since the boundaries then are normal to the acoustic propagation which fits with the assumption for the freestream boundary. Since the domain is not spherical higher risk for problems is even more likely. Figure 4.36a shows how the unphysical pressure fluctuations contaminates the acoustic results. It is unclear whether the unphysical pressure fluctuations have a large impact on the flow-field or not. A close-up of the effects on the duct roof is shown in Figure 4.37a where the symmetric shape is due to the unphysical resonance, though, it is not clear why it is shaped the way it is.

These problems did not occur for Tell [32] as much as in this thesis i.a. because of SOU mistakenly used for some of the transient simulations leading to severe diffusion of turbulent kinetic energy. However, in one of the LES-simulations in [32] where BCD was used a peak appeared slightly over 2,000 Hz which could be the same problematic peaks as in this thesis.

Altogether, this domain is too thin to be suitable for compressible simulations. Therefore, an incompressible approach had to be undertaken in order to avoid unphysical pressure fluctuations. As explained, for low Mach numbers hydrodynamic fluctuations are mostly the dominating source and according to Ask [2] incompressible aeroacoustics produce good results at least when it comes to the magnitude of SPL. This approach therefore has rather good empirical arguments.

By looking at Figures 4.23 to 4.27 it is clear that the broadbanded peak as well as the narrowbanded peak disappear for an incompressible fluid. This is due to the fact that sound cannot propagate in such a fluid and all resonance phenomenas, such as the standing wave, disappear.

The curves are aligned with each other until 1,000 Hz or higher for all figures except for Figure 4.27 and to some extent for Figure 4.26. In both these figures the curves are separated by 5 dB on average though over different frequency ranges. A reason for the behavior at the leading edge could be that the highest pressure in the domain is obtained here which leads to high velocity gradient slightly above the stagnation point. Figures A.55a and A.55b show the pressure coefficients for the both cases. The compressible case has much higher pressure-values than the incompressible which is explained by that the incompressible case only can regulate pressure and velocity which leads to low pressure where the velocities are high and vice versa. In accordance with what was concluded by Ask mentioned in Section 3.6.2.5 this may have lead to some disturbances regarding the incompressible approach. This may explain also why the results for the ”Front cavity”-probe deviates relatively much from the curve of the compressible DES since the air impinges on the edge in a similar manner as on the leading edge of the roofbar.

The cause of why the curves separate at 1,000 Hz or higher seems to be mesh-related. The areas correspondent to the monitors plotted in Figure 4.24, 4.25 and 4.26 have cell sizes in descending order where the probes are located and the curve for the compressible case separates from the incompressible curve for higher frequencies the smaller the cell

size is.

Regarding the surface FFT-plots in Figures 4.28, 4.30, 4.32 and 4.34 the existence of large noise sources for the compressible DES-case is simply due to that turbulence is created in the entire turbulent region. Since there is a lack of turbulence and, thus, vortices for the incompressible DES-case, especially over the downstream half of the hatch, the acoustic sources are absent. At the duct roof for 250 Hz and 500 Hz in Figure 4.31 and Figure 4.33 respectively the incompressible approach overpredicts the noise as it did in Figures 4.28-4.34 that display the entire hatch. A reason for this could be because of the distortion effects when changing to the incompressible flow as is mentioned as one of the conclusions in [2]. This might lead to higher pressure fluctuations and thus higher SPL-values.

It was noticed in Figures 4.32b and 4.34b that high SPL-values were created at the front cavity edge. This could be due to the separation from the leading edge of the cavity which releases separated flow that impinges on the trailing edge and for, possibly, geometrical reasons and/or because the thickness of the boundary layer prior to the cavity have length scales and time scales that together correspond to 500 Hz and 1,000 Hz.

For all cases a pattern is visible at the hatch when considering the acoustic surface sources. Since the stronger source terms seem to lie close to the left boundary on the hatch, this suggests that the flow is directed diagonally and the distribution is thereby asymmetric possibly caused by a swirl created by the duct and/or the roofbar. The diagonal flow comes from the attached additional mirror located in front of the windshield on the passenger side of the truck. This mirror can be seen in Figure 3.4.

It is questionable if the incompressible approach is correct since the domain is still too thin which could affect the turbulence in the y-direction and might have affected the turbulence in the x-direction.

5.3 On the comparison between incompressible LES and DES

Figures 4.38 and 4.39 shows ”Hatch 1” and ”Hatch 2” respectively. The result for ”Hatch 1” are rather good especially for SST-DES but looking at ”Hatch 2” there are significant deviations between the DES-models and LES where DES predicts the highest levels. It is difficult to reach any conclusion, however, one guess is that this is due to that the DES-models for some reason produces higher mass flow in the duct. This implies for the same cross-sectional area and same density a higher velocity for the DES-cases.

In Figure 4.42 and 4.43 for ”Front cavity edge” and ”Duct roof” respectively the results are satisfactorily good especially in the range 100 Hz to 1,000 Hz. SST-DES is superior to SA-DES in these two figures especially over the duct roof. This is probably due to that SST-DES might handle complex flow better in this situation where SA-DES could have problems with defining the true length scale because of an internal flow-situation. The reason why the results are good for the hitherto mentioned figures may be that they are all located beneath or a short distance after the duct. Here the flow is rather insensitive to the flow behavior on the top of the roofbar.

For the "Leading edge"-probe shown in Figure 4.40 the DES-models deviate for low frequencies. As mentioned in Section 3.5 the cell sizes on the surface of the roofbar for the DES-cases are 4 times larger for the top of the roofbar and 8 times larger for the leading edge of the roofbar compared to the mesh for LES. This could be a reason for the differences of the "Leading edge"-probe where the flow is still attached to the roofbar. Also, as it is attached onto the leading edge of the roofbar, RANS is most probably activated which cannot capture turbulent fluctuations in the boundary-layer. This thought to be adding to the early separation of the curves in Figure 4.40.

Consider the "Top"-probe in Figure 4.41. A reason for the deviation could be seen by observing the mean velocities in Figure 4.20. In this figure it is obvious that the flow for LES is attached onto the roofbar on average while for the DES-models the flow separates on average. The higher the separation angle, the greater the possibility for larger turbulent scales to be developed and thus the larger pressure fluctuations for smaller frequencies which is the case for the DES-models. That is possibly the reason to why much larger SPL-values occur for DES compared to LES for low frequencies. Consequently LES has higher SPL-values than DES because of that higher velocities and smaller scales are present for LES.

It is unknown why the separation angles differ when going from LES to DES. The higher velocity leads to higher gradients when the air flows around the small radius when going from the leading edge to the top of the roofbar. This induces a force from the attached flow on the freestream flow which creates an opposite force pushing the attached flow to still be attached on the top of the roofbar. Where this high velocity for LES emanates from is difficult to see. The spatial resolution requirements have been met but at first the CFL-requirement was not met. A test-run with half the time-step $\Delta t = 7.5 \cdot 10^{-6}$s proved not to solve the issues. The transition of the cell-sizes prior to the roofbar might be a cause of the high velocity, i.e. the velocity from coarser cells may not have time enough to develop until it reaches the roofbar. Another plausible and the most likely cause could be the turbulent viscosity-ratio which values are shown in Figure A.56 for all cases. Looking at LES the figure reveals that there are portions of high levels of turbulent viscosity-ratios found around the sunvisor possibly caused by large velocity gradient fluctuations, see Eq. (2.16). The fluctuations of the velocity gradient are then transported onto the roofbar where a higher ν_T gives a higher skin-friction coefficient and thus a lower tendency to separate from the geometry. Comparing this with the compressible and incompressible case of the SST-DES model suggests that the sunvisor is not properly resolved for LES which is reasonable since the mesh is quite coarse at this location. The scales might be quite anisotropic here since large cells which should be simulated using DNS and not an SGS-model. The path along which the flow is flowing from the sunvisor to the roofbar needs to be refined as well so that quantities do not grow on the way to the roofbar due to cell-size transition. The SA-DES model also has high levels of turbulent viscosity-ratio especially between the sunvisor and the wind-screen, however, the latter might be due to that the model can experience difficulties with defining the length scales when it comes to internal flows as mentioned in Section 2.2.1.1, i.e. if that could be regarded as an internal flow.

For all the Figures 4.44 - 4.51 LES is much more detailed due to that 0.5 mm cells was used on the surface at the roofbar and the hatch while 2 mm was used for DES. This has, of course, a large impact on when displaying the results. For larger cell sizes values may appear larger than they actually are and this might show an excessive relative difference between LES and DES. Since the LES-case because of the attached has a larger x-momentum this will affect the results by causing higher SPL-values on the hatch.

Consider the isolated relatively high SPL-values at the rear cavity mentioned among the results, for instance in Figure 4.46c. This is most probably due to the air flowing out of the spoiler volume in the opposite direction of travel. The flow hits the cavity edge just as on the other side of the hatch, at the front cavity edge. However, the SPL-values at the rear cavity are substantially lower due to lower velocities.

Figure 4.45 shows almost identical results for the methods when it comes to the magnitude of the SPL although the distribution of the sources are slightly different which might be due to different surface resolution. In Figures 4.47 and 4.49 the SST-DES predicts the closest results to LES. For a frequency of 1,000 Hz LES has suddenly a large source on the duct roof as can be seen in Figure 4.51a. This could be due to that portions of high $\nu_{T,SGS}$ in Figure A.56a mentioned previously which makes the flow to attach onto the roof under the roofbar. In this case the length scales for the SGS-scales are 0.5 mm or less in the duct which might correspond to approximately 1,000 Hz.

5.4 On the spoiler's impact on the results

The spoiler volume did not have any effect at all on the acoustics at least as far downstream as "Hatch 2" as the results were considered to be identical in the sense that there were only small unsignificant differences. Turbulent scales were not developed as for the other incompressible DES-cases when the spoiler volume was included in the simulations. This suggests that the cause of the undeveloped scales is a problem related to the features of the boundary conditions rather than the gap leading to the spoiler volume. The fact that incompressible LES developed scales over the hatch but not the incompressible DES suggests that DES is much more sensitive to the boundary conditions. In addition, LES might have had an advantage from a higher x-momentum since its flow is attached to the roofbar while the x-momentum for the incompressible DES-cases is lower due to earlier separation. Thus, LES might be more sensitive to stiff boundary conditions than was apparent in these results. Since no turbulent scales were developed for the incompressible DES-cases this might suggest that there could be smaller scales there that could not be resolved due to too large cell-sizes.

5.5 Averaging "Hatch 2"

Averaging "Hatch 2" with respect to the surrounding probes first led to an underestimation of the curves even though the pressure fluctuations were strictly positive by taking the square of the pressure fluctuation in each probe. The reason was that the averaging took place in the time domain and not the frequency domain. The transformed pressure data for each probe was therefore exported in SPL-values dependent on the frequency

and averaged in MATLAB instead and thereafter imported back to StarCCM+. The reason why they had to be exported to MATLAB was that the already transformed SPL-values could not be called using the user-code syntax in the CFD-software.

5.6 Tonal peaks

The Rossiter mode did not show up in the monitor plots which might have been caused by two things. Firstly, the leading edge of the cavity has a rather large radius which attenuates the created vortices which have a resulting smaller velocity than for an ideal rectangular cavity. Secondly, the self-sustained oscillation should be absent which does not create a periodic flow and therefore no peak exists. Some effect might be induced by including the entire real cavity which extends in the stream-wise direction in reality. If there would have been a Rossiter mode, which is most probably not the case, it would most likely not have been properly resolved. Setting a small area with 0.25 mm enclosing the front cavity edge would probably help to capture the rather small oscillations of the flow and thus capture the Rossiter mode.

The Helmholtz frequency calculated in [32] lies close to the unphysical peak at 2,400 Hz. However, this peak is most probably only unphysical since, once again, the leading edge of the cavity has a quite large radius which attenuates the separation effect. According to [13] the Helmholtz resonator is characterized by having "overhanging lips" that partly seals the inlet. This is not the case for this cavity since the trailing edge is partly sealed but the leading edge directs a fraction of the flow down to the cavity and thus attenuate the resonance if there is any.

5.7 Methodology

The domain that has been used for the transient simulations has proven to generate problems. Both incompressible and compressible flow have shown some weak sides. Since the incompressible flow led to undeveloped turbulence for incompressible DES and thereby missing to generate aeroacoustic data on the hatch an incompressible approach is not to be recommended for this special case, i.e. for a thin domain where the distance between boundary conditions is small. Although the compressible approach gave developed turbulence above the hatch turbulent structures at the boundary caused huge unphysical pressure fluctuations which makes the approach unsuitable. It was not found if these fluctuations had an impact on the flow-field.

To begin with, a better method for aeroacoustic problems would be to study the subject of aeroacoustics deeply. Benchmark problems with measure data helps to detect pitfalls and to build up confidence when making these simulations. When experience has been gained regarding the subject simulations on the truck can be made.

Until measure data are available the aeroacoustic results of these simulations are not of qualitative interest but serves the purpose of creating an approach for aeroacoustic studies based on relative simulation data.

6 Conclusions

The main conclusions of this Master's thesis are the following:

- The domain used was too thin to be used for aeroacoustics.
- Turbulent structures at the freestream boundary had severe effects on the acoustic field.
- Compressible and incompressible simulations using DES agreed well up to a certain frequency, however, the incompressible case somewhat overpredicted the results. The certain frequency might have been mesh-related.
- SA-DES predicted high levels of the turbulent viscosity compared to SST-DES which might be due to that SA-DES could have difficulties with internal flows.
- The difference between SST and SA as RANS-models for DES were minor, however since SST showed somewhat better results and as it is regarded as a more general model it is recommended to use for a problem with this complexity.
- LES had a distorted mean velocity-profile which most probably was caused due to that the predicted turbulent viscosity was much higher for LES due to poor meshing at the sunvisor which releases portions of relatively high turbulent viscosity onto the roofbar.
- Turbulent scales developed far downstream created strong noise sources on the hatch for LES and compressible DES.
- The incompressible-DES cases were unable to develop turbulent scales over the hatch and did agree well with LES up to about a third of the hatch. This might have been due the DES-models' sensitivity to strict boundary conditions and/or the difference in separation angle leading to different x-momentum.
- The volume beneath the spoiler had no effect on the flow field nor the acoustics for the chosen probes.
- Compared to LES the DES-cases showed stronger noise sources in the proximity of the roofbar.
- Measure data are crucial for aeroacoustic simulations.
- Calculating the root-mean-square value of SPL for a probe surrounded by other probes was successful when the averaging took place in the frequency domain.
- Except for the unphysical peak for the compressible DES-case only broadbanded noises were found.
- The time required for the simulations, except for the case without the volume beneath the spoiler, were incompressible LES, compressible SST-DES, incompressible SST-DES and incompressible SA-DES. Although SA-DES was quite much faster than SST-DES.

7 Future work

The subject of aeroacoustics is relatively unexplored at Volvo GTT. Therefore studies of benchmarks are essential in order to gain a fundamental understanding of the subject as well as experience so that a new approach can be established.

Beginning with simple problems is a good way to isolate behaviors in a domain. The present domain could be simplified to just contain the roofbar, cavity and hatch located at a flat wall. In this way the noise contribution of each of the three parts could be studied. The roofbar could for instance be tested with different angles and positions relative to the cavity in order to determine the interactions between them.

If the cavity is isolated it can be compared with cavity benchmark problems. Simulating the truck cavity with a benchmark cavity could reveal similarities and differences. Subsequently, the effect of the depth of the cavity could be investigated since this is simplified for the domain used in this thesis.

The domain should be widened in every direction and preferably be spherical so that acoustic waves can impinge onto the freestream boundaries normally and be absorbed. Setting the boundaries in the far-field avoids problems at the boundaries due to turbulent structures.

The focus region in the domain could be tested with different widths, for instance 60 cm, 30 cm and 15 cm. Outside the focus region the mesh can gradually be coarsened.

A 2D-domain would also be useful to get feel for the problem, however, LES and DES describes turbulence which is a three-dimensional phenomena. It is possible to write a code to enable 2D-LES in other softwares but so far this is not possible in StarCCM+.

References

[1] J. D. Anderson. *Modern Compressible Flow - With Historical Perspective*. New York: McGraw-Hill, 3 edition. ISBN 007-124136-1.

[2] J. Ask. *Predictions Of Aerodynamically Induced Wind Noise Around Ground Vehicles*. PhD thesis, Chalmers University of Technology, Gothenburg, 2008.

[3] J. Blazek. *Computational Fluid Dynamics: Principles and Applications*. Elsevier Science Ltd., Amsterdam, 2^{nd} edition, 2005. ISBN 0-08-044506-3.

[4] A. Brandt. *Ljud och vibrationsanalys I*. Saven EduTech AB, 2000.

[5] M. Brennberger. Experimentelle und numerische Grundsatzuntersuchung zum Schiebedachwummern. In *Conf. Aerodynamik*, Essen, 2004. Haus der Technik.

[6] *StarCCM+ User Guide*. CD-Adapco, 2013. v. 8.02.008.

[7] I. M. Cohen and P. K. Kundu. *Fluid Mechanics*. Elsevier, 4^{th} edition, 2008.

[8] D. C. Crighton. Basic principles of aerodynamic noise generation. *Prog. Aerospace Sci.*, pages 16:31 – 96, 1975.

[9] N. Curle. The influence of solid boundaries upon aerodynamic sound. In *Proceedings of the Royals Society London*, pages 505 – 514, 1955.

[10] D. J. Ewins. *Modal Testing: theory practice and application*. Research Studies Press Ltd., Baldock, 2^{nd} edition, 2000.

[11] J. Ffowcs-Williams and D. Hawkings. Sound Generation by Turbulence and Surfaces in Arbitrary Motion. *Philosophical Transactions of the Royal Society*, 264:321–342, 1969.

[12] G. B. Folland. *Fourier analysis and its applications*. Wadsworth & Cole, 2^{nd} edition, 2000. ISBN 0534170943.

[13] X. Gloerfelt. *Cavity Noise*. PhD thesis, Arts et Métiers ParisTech, Paris, France, 2008.

[14] A. Hedlund. Conversation, March 2013. Cab Features & Noise and Vibration Specialist, Volvo Group Trucks Technology.

[15] W. Jones and M. Wille. Large-eddy simulation of a jet in a cross-flow. pages 4:1 – 4:6, 1995.

[16] A. Kierkegaard. Conversation, June 2013. Senior Engineer, Technical Support, CD-Adapco London.

[17] A. Kierkegaard. Conversation, August 2013. Senior Engineer, Technical Support, CD-Adapco London.

[18] M. Lighthill. On sound generated aerodynamically. i. General Theory. In *Proceedings of the Royals Society London*, pages 564 – 587, 1952.

[19] F. Menter, M. Kuntz, and R. Langtry. Ten Years of Industrial Experience with the SST Turbulence Model. *Turbulence Heat and Mass Transfer 4*, 2003.

[20] P. Moin and J. Kim. Numerical investigation of turbulent channel flow. *Journal of Fluid Mechanics*, 118:341 – 377, 1982.

[21] U. Piomelli and J. Chasnov. *Large-eddy simulations: Theory and application.* Kluwer Academic Publishers, 1996.

[22] I. Proudman. The generation of noise by isotropic turbulence. In *Proceedings of the Royals Society London*, pages 119 –132, 1952.

[23] T. D. Rossing and N. H. Fletcher. *Principles of Vibration and Sound.* Springer Science + Business Media, 2004.

[24] J. Rossiter. Wind-tunnel experiments on the flow over rectangular cavities at subsonic and transonic speeds. (3438), October 1964.

[25] F. G. Schmitt. About Boussinesq's turbulent viscosity hypothesis: historical remarks and a direct evaluation of its validity. *Comptes Rendus Mécanique*, 335:617 – 627, September – October 2007.

[26] M. L. Shur, P. R. Spalart, M. K. Strelets, and A. K. Travin. A hybrid RANS-LES approach with delayed-DES and wall-modelled LES capabilities. *International Journal of Heat and Fluid Flow*, 2008. URL `http://www.elsevier.com/locate/ijhff`.

[27] P. Spalart and S. Allmara. A One-equation Turbulence Model for Aerodynamic Flows. *AIAA Paper 92-0439*, pages 5 – 21, 1992.

[28] P. Spalart, S. Deck, M. L. Shur, K. D. Squires, M. K. Strelets, and A. Travin. A new version of detached-eddy simulation, resistant to ambiguous grid densities. *Theoretical Computational Fluid Dynamics*, 20, 2006.

[29] P. R. Spalart. *Young-Person's Guide to Detached-Eddy Simulation Grids.* Boeing Commercial Airplanes, Seattle, Washington, 2001. v. 8.02.008.

[30] W. R. Stapleford and G. W. Carr. Aerodynamic noise in road vehicles, part 1: The relationship between aerodynamic noise and the nature of the airflow. *The Motor Industry research Association*, 1971/2, November 1970.

[31] M. Strelets. Detached Eddy Simulation of Massively Separated Flows. *AIAA Paper 2001-0879*, 2001.

[32] J. Tell. Aeroacoustic study on roof bow - CFD generation of input data for hybrid approach. MSc thesis, Chalmers University of Technology, Gothenburg, 2012.

[33] H. K. Versteeg and W. Malalasekera. *An introduction to Computational Fluid Dynamics - The Finite Volume Method*. Harlow: Pearson Education Ltd., 2 edition. ISBN 978-0-13-127498-3.

[34] M. Wang and P. Moin. Computation of trailing-edge flow and noise using large-eddy simulation. *AIAA Journal*, 38(12):2201 – 2209, November 2000.

[35] J. R. Welty, C. E. Wicks, R. E. Wilson, and G. L. Rorrer. *Fundmentals of Momentum, Heat and Mass Transfer*. John Wiley & Sons, 2^{th} edition, 2008. ISBN 978-0470128688.

A Appendix

In the appendix discussion-related results and custom codes are presented.

A.1 Various flow-field results

Here, results that are not presented among the main results are attached mainly to add to the discussion section.

A.1.1 Pressure coefficients for compressible and incompressible flow

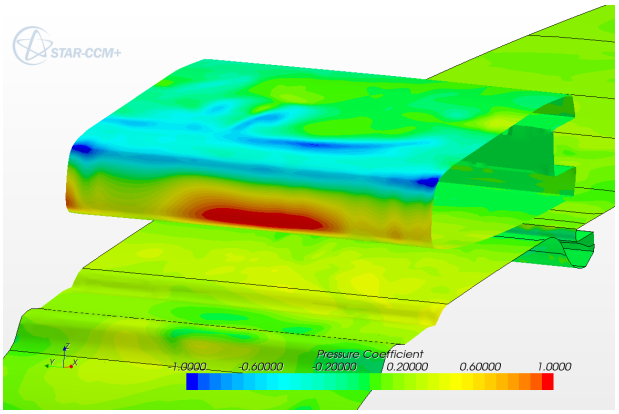

(a) Pressure-coefficient for compressible SST-DES.

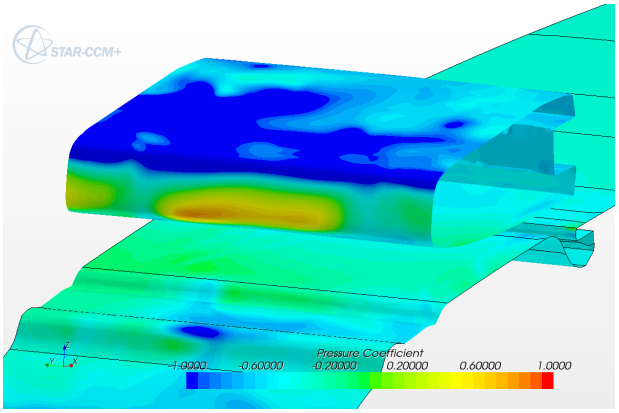

(b) Pressure-coefficient for incompressible SST-DES.

A.1.2 Turbulent viscosity-ratios

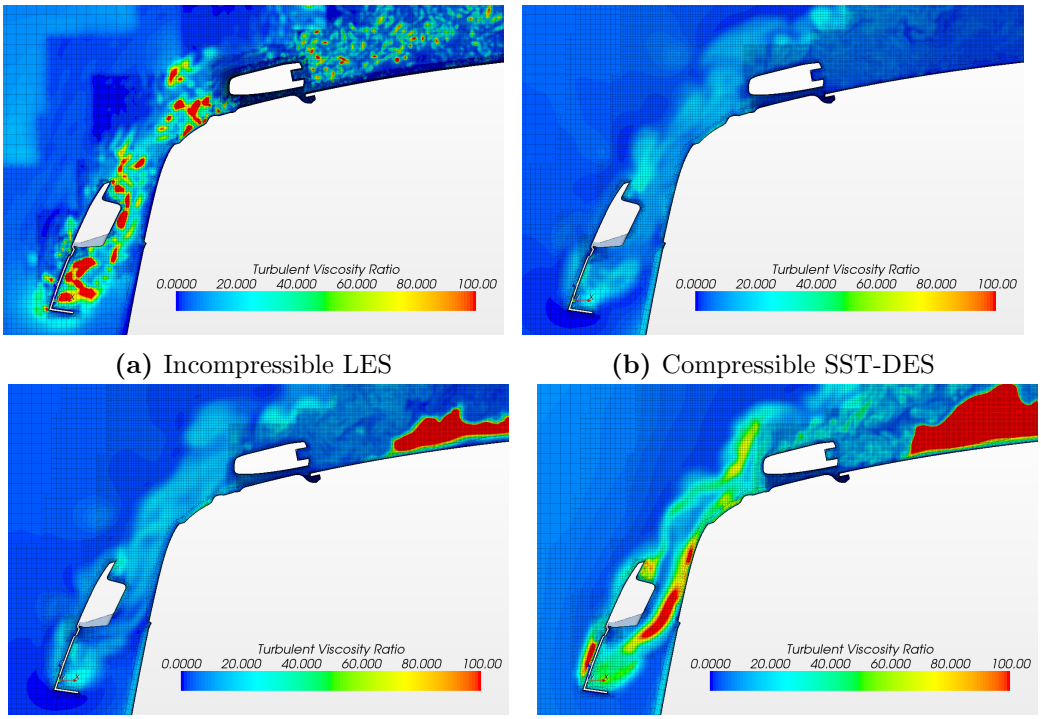

(a) Incompressible LES **(b)** Compressible SST-DES

(c) Incompressible SST-DES **(d)** Incompressible SA-DES

Figure A.56: Contour-plots showing the turbulent viscosity-ratio between the cases.

A.1.3 Velocity boundary conditions at the left boundary

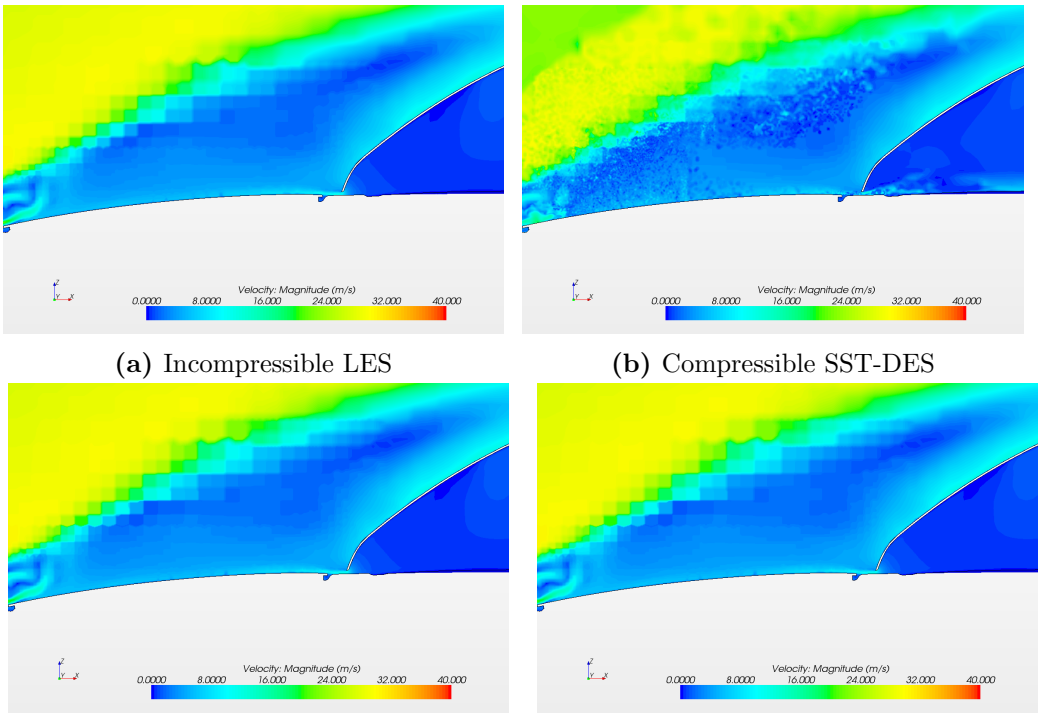

(a) Incompressible LES

(b) Compressible SST-DES

(c) Incompressible SST-DES

(d) Incompressible SA-DES

Figure A.57: Contour-plots showing the left boundary of the cases. Note that the incompressible cases have the same left boundary while the compressible case has a different one because of the freestream boundary condition.

A.1.4 Pressure fluctuations at the left boundary

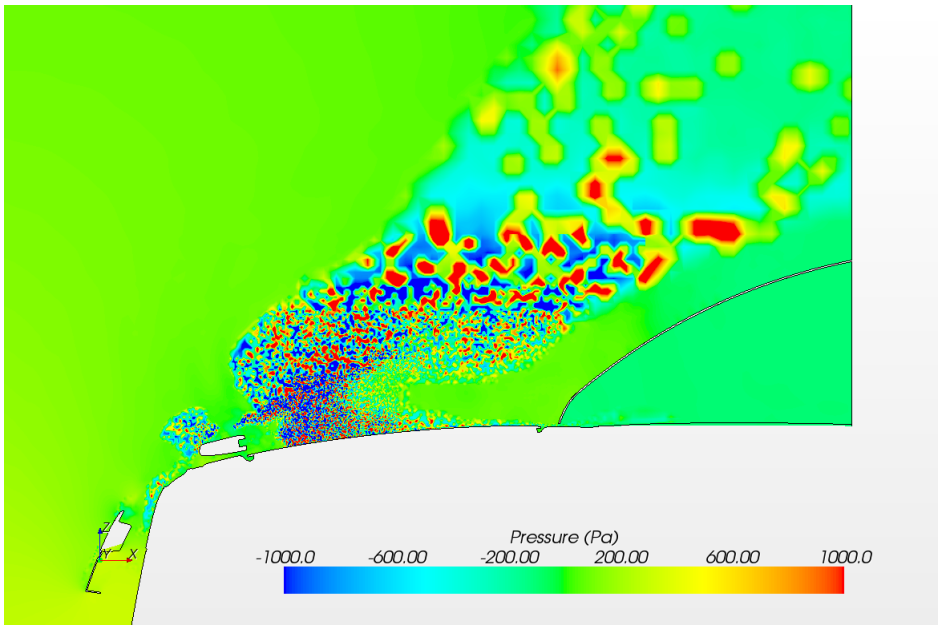

Figure A.58: Extreme pressure fluctuations at the left boundary for the compressible SST-DES simulation. The same tendencies were also found at the right boundary.

A.2 Custom codes for averaging the surrounding probes

Here the custom codes made in StarCCM+ as well as MATLAB are presented. The StarCCM+-code describes the incorrect way of averaging while the MATLAB-code describes the correct way.

A.2.1 Computing the average in StarCCM+

The following user function code was specified in StarCCM+ in order to produce an average of the probes surrounding "Hatch 2" according to Eq. 3.1:

```
pow((pow($Hatch2Report,2) + pow($Hatch2P1Report,2) + pow($Hatch2P2Report,2) +
 + pow($Hatch2P3Report,2) + pow($Hatch2P4Report,2))/5),1/2)
```

Here `$` is used to call a scalar variable. `$$` would have been used for a vector. The command `pow` is used to specify powers on the form `pow($Variable, exponent to variable)`. For instance x^2 is written `pow($x,2)` using this syntax.

A.2.2 Code in MATLAB

```
% Read .csv-file (csv = column separated value, the tabular
    format in StarCCM+)
csvread('W:\..\average.csv',1)
data=ans; % Column [Frequency P1 P2 P3 P4 P] where P(1-4) are
    the involved probes

% Loop to obtain the pressure as a function of frequency
for i=2:6;
p(:,i)=10.^(data(:,i)/20)*(2*10^-5);
end
% Creating a pure pressure vector
p_vector=p(:,2:6);

% Computing the root-mean-square value to obtain the averaged
    pressure
p_rms=rms(p_vector,2)

% Computing the SPL-value with the average pressure
SPL_av=20*log10(p_rms/(2*10^-5))

% Collecting new vectors
Hatch2_av = [data(:,1) SPL_av];

% Writing a new .csv-file
csvwrite(W:\..\'Hatch2_av',Hatch2_av)
```